UNIVERSIDAD DE CHILE
FACULTAD DE CIENCIAS FÍSICAS Y MATEMÁTICAS
DEPARTAMENTO DE GEOLOGÍA

SILICA SINTER FORMATION AT THE EL TATIO GEYSER FIELD, CHILEAN ALTIPLANO: INSIGHTS FROM RADIOCARBON DATING

TESIS PARA OPTAR AL GRADO DE MAGÍSTER EN CIENCIAS, MENCIÓN GEOLOGÍA

SILVINA SLAGTER

PROFESOR GUÍA:
MARTIN REICH MORALES

MIEMBROS DE LA COMISIÓN:
FERNANDO BARRA PANTOJA
DIEGO MORATA CÉSPEDES

SANTIAGO DE CHILE

2019

FORMACIÓN DE SÍNTER SILÍCEO EN EL CAMPO DE GÉISERES DE EL TATIO, ALTIPLANO CHILENO: UNA PERSPECTIVA DESDE LA DATACIÓN MEDIANTE CARBONO 14

La actividad geotermal es registrada en los depósitos de sínter silíceo, que se forman cuando aguas termales se descargan y enfrían rápidamente en superficie. La formación de sínter silíceo entrampa microbios que viven en aguas termales, así como también material vegetal. La preservación de ésta materia orgánica permite la datación mediante ^{14}C en sistemas geotermales activos como El Tatio en el norte chileno. A pesar de ser el tercer campo de géiseres más grande del mundo, después de Yellowstone en Estados Unidos, y El Valle de Géiseres en Kamchatka, la edad absoluta de este sistema geotermal permanece sin constreñir. El campo de géiseres El Tatio está localizado en el altiplano chileno, a una altitud de más de 4.200 metros sobre el nivel del mar, y sus condiciones climáticas extremas como la alta tasa de evaporación, gran amplitud térmica, y alta radiación UV, resultan en un ambiente único análogo a la Tierra primitiva y Marte.

En este estudio, la edad de los depósitos de sínter silíceo de El Tatio es determinada mediante ^{14}C en 21 muestras de superficie usando espectrometría de masas con acelerador. Con el objetivo reconstruir la evolución de la formación de sínter silíceo, la estrategia de muestreo incluyó la colección de muestras en perfiles estratigráficos de afloramientos de sínter fósiles. Las edades varían de $15{,}042 \pm 30$ a 230 ± 35 años B.P., indicando que El Tatio ha tenido una descarga activa de aguas termales por al menos 15.000 años. Estas edades son utilizadas para determinar la tasa de precipitación en El Tatio, que fue calculada entre 0,14 and 2,57 kg/años/m^2. Estos valores están entre las más altas tasas de precipitación medidas en sistemas geotermales y son consistentes con experimentos de precipitación *in situ* en El Tatio (0,84-2,92 kg/años/m^2). Los resultados indican que las condiciones ambientales extremas en el Altiplano Chileno, i.e., alta tasa de evaporación y enfriamiento de las aguas termales, junto con una gran amplitud térmica, han jugado un rol fundamental en la construcción y preservación de los depósitos de sínter silíceo.

La mineralogía de las muestras de sinter silíceo fue determinado utilizado difracción de rayos X y espectroscopia Raman, mostrando que las fases minerales presentes en los sinter fósiles son dominantemente ópalo-A y ópalo-A/CT, reflejando un general bajo grado de diagénesis. Estos resultados apuntan a una compleja evolución mineral en el Tatio, donde la maduración de sílice está asociada a procesos de disolución-reprecipitation.

Este estudio resalta la importancia de un mejor entendimiento de la evolución de la formación de sinter silíceo en sistemas geotermales y explora el uso del radiocarbono como una herramienta novedosa para constreñir las tasas de precipitación, Además, este estudio enfatiza el impacto de las condiciones ambientales en la precipitación de sílice en los sistemas geotermales andinos.

SILICA SINTER FORMATION AT THE EL TATIO GEYSER FIELD, CHILEAN ALTIPLANO: INSIGHTS FROM RADIOCARBON DATING

Geothermal activity is recorded in silica sinter deposits, which form when high silica, alkali chloride hot spring waters discharge and rapidly cool at the surface. Silica deposition entombs microbes that thrive in hot springs water, as well as plant material. The preservation of this organic matter allows radiocarbon dating of sinter in active geothermal systems, such as El Tatio geothermal field in northern Chile. Despite being the third largest geyser field in the world after Yellowstone National Park and the Valley of Geysers in Kamchatka, the absolute age of this geothermal system remains unconstrained. The El Tatio geyser field is located in the Chilean Altiplano at an altitude of 4200 meters above the sea level, and its extreme conditions including low atmospheric pressure, high evaporation rate, high diurnal temperature variation, and high UV radiation result in a unique environment analog to early Earth and Mars.

In this study, the age of silica sinter deposits at the El Tatio geyser field is determined by radiocarbon (C-14) dating of 21 surface samples using Accelerator Mass Spectrometer. In order to reconstruct the evolution of silica deposition, the sampling strategy included the collection of rocks from meter-thick stratigraphic profiles of fossil sinters outcrops. Radiocarbon ages range from $15,042 \pm 30$ to 230 ± 35 years B.P., indicating that El Tatio system has had an active discharge of silica-rich chloride springs over at least the past 15,000 years that resulted in the formation of extensive sinter deposits. These ages are used to determine the silica precipitation rate at El Tatio, which was calculated between 0.14 and 2.57 kg/years/m^2. These values are among the highest precipitation rates in geothermal systems where data are available and are consistent with *in situ* silica precipitation experiments at El Tatio (0.84-2.92 kg/years/m^2). Our results indicate that the extreme environmental conditions of the arid Chilean Altiplano, i.e., high evaporation and cooling rate of thermal waters, and significant daily temperature oscillations, have played a key role in the construction and preservation of silica sinter deposits.

The mineralogy of sinter samples was determined using X-ray diffraction and micro-Raman analysis, showing that the mineral phases present in paleogeyser mounds are dominantly opal-A and opal-A/CT, reflecting an overall low degree of diagenesis in the geyser mounds sampled. These results point to a complex mineralogical evolution of sinter mounds at El Tatio, where silica maturation is most likely associated with dissolution and reprecipitation processes.

Overall, this study highlights the importance of better understanding the long term evolution of sinter formation in geothermal systems and explores the use of radiocarbon techniques as a novel tool to constrain silica precipitation rates. Also, this study emphasizes the impact of environmental conditions on silica precipitating spring systems in the high Andes.

"La creatividad requiere tener el valor de desprenderse de las certezas"
Erich Fromm

ACKNOWLEDGMENTS

CONTENTS

TABLE INDEX

FIGURE INDEX

CHAPTER 1: INTRODUCTION

1.1 Motivation

Silica sinter deposits overlying geothermal fields are reliable records of environmental, geochemical and biological changes through time. Therefore, determining the absolute ages of formation of these deposits is fundamental to constrain the timing and evolution of processes that have shaped silica precipitation on the Earth's surface.

Silica sinter forms when near neutral thermal water cools at the surface. The silica carried out in solution aggregates, polymerizes, and precipitates as a result of evaporation processes in cooling thermal pools and discharge channels (Fournier, 1985; Williams and Crerar, 1985). Pre-existing substrates including microorganisms and other biological fragments (e.g., thermophilic microbes, plants, insects, and diatoms) become silicified forming mound buildups and terraced sinter over time. Hence, the preservation of organic matter allows dating the formation of sinter deposits using radiocarbon (^{14}C) methods.

Sinter deposits are widely distributed around the world and throughout geologic time, with examples related to ancient hydrothermal activity such as the Archean Dresser Formation in Australia (Djokic et al., 2017), the Paleozoic Rhynie chert in Scotland (Trewin and Rice, 2004), the Devonian to Carboniferous Drummond Basin sinters in Australia (Walter et al., 1996), and the Jurassic sinters of the Argentinian Patagonia (Guido and Campbell, 2011). Younger silica sinters include, for example, the famous Pleistocene Steamboat Springs deposits in Nevada, U.S.A. (11,493 ± 70 years; Lynne et al., 2008), and Yellowstone National Park (~ 8000 years B.P.; Lowenstern et al., 2016) and Opal Mound sinters from Utah, USA (1,920 ± 160 and 1,630 ± 90 years; Lynne et al., 2005).

The identification and geomorphic interpretation of these paleosurface products can be used as guides for the exploration of concealed geothermal resources and epithermal Au-Ag deposits (e.g., Guido et al., 2012; Rodgers et al., 2004; Lynne et al., 2007; Sillitoe, 2015). Additionally, silica sinter deposits have been the focus of astrobiological investigations (Konhauser et al., 2003, Handley et al., 2005; Gibson et al., 2014; Campbell et al., 2015), and recently the El Tatio geyser in the Altiplano of northern Chile has been proposed as an early Mars analog environment because of similar siliceous sinter textures observed on the Martian surface (Ruff and Farmer, 2016).

Many studies have focused on understanding the evolution of geothermal systems by studying silica sinter deposits. In the Te Kopia thermal area, Taupo Volcanic Zone, Bignall and Browne (1994) identified several stages of thermal activity based on silica sinter presence and surficial hydrothermal alteration minerals. Also, paleo hydrothermal systems such as Mangatete, in Taupo Volcanic Zone (Drake et al., 2014) were studied using ^{14}C dating in charcoal and tephra, integrated with faults rupture events to reconstruct a complex history of volcanological and geothermal activity. At Steamboat Springs, Nevada, U.S.A., drill cores with several stages of diagenetic transformations were identified and dated (Lynne et al., 2008). More recent studies based on facies mapping in a well-preserved outcrop from a sinter apron in Atastra Creek in California and Nevada, U.S.A, recognized three hydrothermal phases in the evolution of the study area during the Miocene (Campbell et al., 2018).

At the El Tatio geothermal system in the Altiplano of northern Chile, extensive silica sinter deposits occur distributed throughout the geyser field. Recent studies have proposed that the extreme environmental conditions at El Tatio, including high altitude (~4.200 m a.s.l.) and significant diurnal variations in temperature (~up to 40ºC), result in increased silica precipitation rates. This hypothesis remains untested due to the lack of absolute ages of the sinter deposits (Nicolau et al., 2014).

To gain knowledge about the timing of silica sinter precipitation and the evolution of the El Tatio sinter deposits, radiocarbon dating was performed in the organic matter enclosed in the silica matrix from four paleogeyser mounds. These data were complemented with extensive field mapping of the deposits, detailed petrographic observations and mineralogical characterization of the sinter samples. Furthermore, *in-situ* precipitation experiments were undertaken to constrain present-day silica precipitation rates. These data are combined to constrain how silica precipitation has changed over time, and how the unique environmental conditions at El Tatio impact the formation of sinter deposits.

1.2 Background

1.2.1 El Tatio Geyser Field

The El Tatio geothermal field is located at 4270 meters above sea level, 95 km east of the town of Calama, Antofagasta Region, northern Chile. El Tatio is one of the largest geyser fields in the world (Hurwitz and Manga, 2017) with more than 200 thermal features within an area of ~30 km^2 (e.g., Zeil, 1959; Trujillo, 1969; Glennon and Pfaff, 2003; Tassi et al., 2010). It presents numerous thermal features, including fumaroles, geysers, hot springs, hot pools, boiling pools, mud pools, and sinter deposits, mainly located along the Salado river valley and its affluent.

This unique high altitude geothermal system is characterized by extreme climatic conditions such as significant daily temperature variations, high evaporation rates, and high UV radiation. The climate in this area is characterized by low precipitation (<100 mm/year). Rainfall is particularly seasonal, particularly focused from December to March (Fernandez-Turiel et al., 2005). The mean annual temperature ranges from 8 to 11 °C. Daily temperature variation reaches 35 °C. In winter the temperature can reach -30 °C (Fernandez-Turiel et al., 2005).

The geologic sequence that outcrops in the El Tatio area include: Jurassic marine sediments, Jurassic-Cretaceous meta-andesites, and Cretaceous sediments; Tertiary to Miocene ignimbrites, andesites, and volcanic agglomerates; and Plio-Holocene dacitic and rhyolitic ignimbrites, lavas and domes. Glacial, alluvial and colluvial deposits overlay this geologic sequence and are locally covered by siliceous sinter deposits (Nicolau et al., 2014 and references therein).

The first investigations at El Tatio evaluated the energy potential and are focused almost exclusively on fluid geochemistry aspects (Lahsen and Trujillo, 1975). More recently, studies have characterized geothermal features present at the site (Glennon and Pfaff, 2003) and addressed the origin of thermal waters (Tassi et al., 2010; Cortecci et al., 2005; Munoz-Saez et al., 2018). Two exploration wells were drilled in El Tatio between 1969 and 1971, finding thermal fluids at 263 °C at 800 m depth (Lahsen and Trujillo, 1975). Based on these data, the energy potential for this particular system has been estimated between 100 and 400 MW (Lahsen, 1988). Currently, El Tatio

geyser field is a geothermal park administered by Toconce and Caspana communities, with a focus on conservation and tourism.
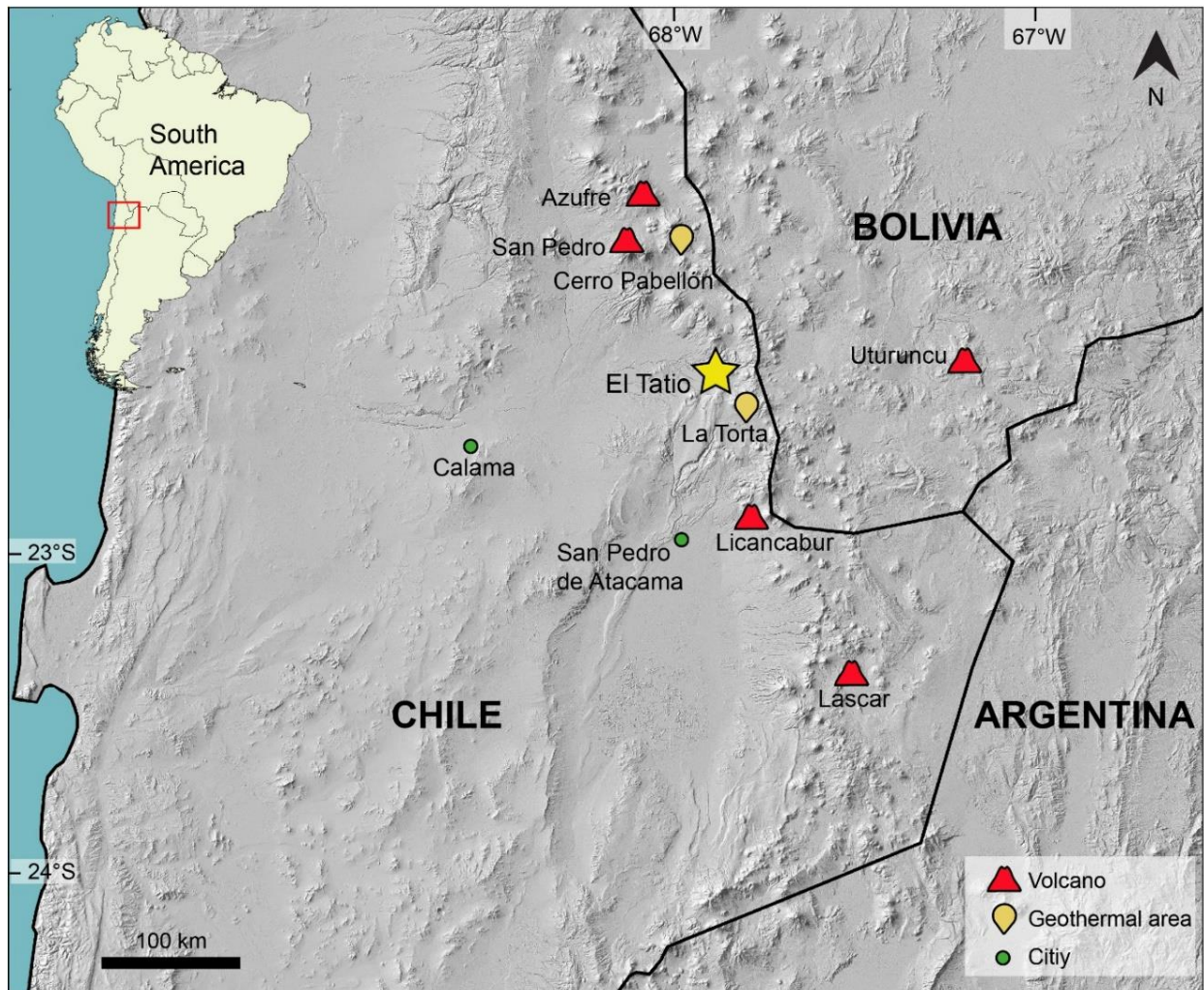
Figure 1. Location of El Tatio geyser field.

The geothermal field is located in a hemigraben with an orientation NE-SW. El Tatio thermal waters are near neutral pH, alkali-chloride and display high concentrations of silica (up to 102 mg/L; Tassi et al., 2010), sodium (4000 mg/L) arsenic (up to 30 mg/L), boron (up to 100 mg/L) and antimony (up to 1.5 mg/L) (Cusicanqui et al.,1976; Giggenbach, 1978; Cortecci et al., 2005; Landrum et al., 2009; Tassi et al., 2005, 2010). Hydrogeological models proposed by Cusicanqui et al. (1975) and Giggenbach (1978) includes a geothermal reservoir emplaced in volcanic and ignimbritic rocks and a second shallower aquifer hosted in a dacitic unit, sealed by silica deposits and clays. Meteoric waters are recharged through deep faults at higher altitude ~15 to 20 km to the east of El Tatio (Giggenbach, 1978; Munoz-Saez et al., 2018) and are then heated along the flow path. Recent studies have improved the conceptual model of the geothermal system proposed during the 1970s, confirming that thermal waters are meteoric in its origin, and have >60 years residence time that, whereas local groundwater has a time-averaged residence time of <60 years, according to tritium (^{3}H) data (Munoz-Saez et al., 2018). Geophysical surveys identified a zone of

low electrical resistivity that extends toward the south and southeast of the field (Lahsen and Trujillo, 1975), suggesting groundwater flow into the basin from that direction.

1.2.2 Silica sinter formation

The origin of dissolved silica in thermal waters is related to water-rock interaction processes that occur in geothermal systems. In most geothermal reservoir waters (with T < 350 °C, pH < 8), dissolved silica consists mainly of monomeric silica (monosilicic acid, H_4SiO_4) (Zotov and Keppler, 2002). At higher pHs (pH> 8), however, the monomeric silica dissociates according to the equations (Fig. 2):

$$H_4SiO_4 = H^+ + H_3SiO^{4-}$$
$$H_3SiO_4- = H^+ + H_2SiO_4^{2-}$$
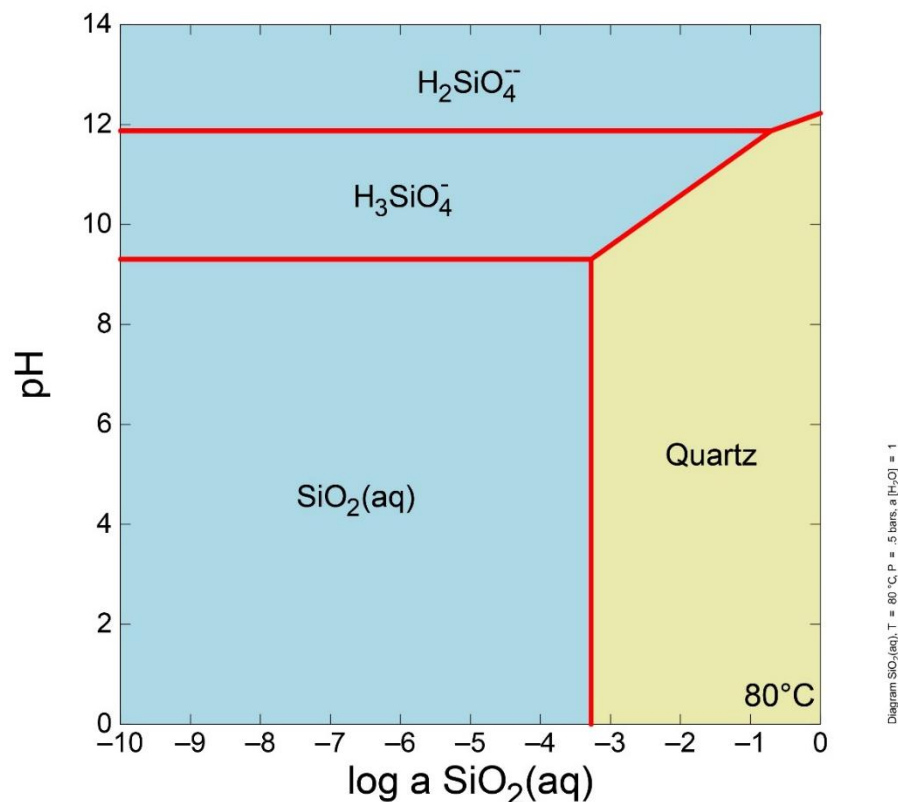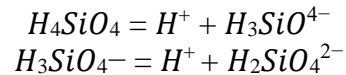
Figure 2. Log aSiO$_2$-pH diagram of silica species in thermal water. The light blue field represents aqueous species, and light brown field the solid (mineral) species. a[SiO$_2$] = 10-2; a[H$_2$O] = 1. The diagram was constructed using Geochemist's Workbench with a provided database at 80°C and 0.5 bar (approximate for El Tatio thermal water conditions).

As the alkali chloride hydrothermal water discharges at the surface and cools < 100 °C, silica precipitates and accumulates to form siliceous sinter deposits. Rapid cooling is the main mechanism by which silica sinter forms (Tobler et al., 2009; Boudreau and Lynne, 2012). The processes affecting sinter formation were studied by Tobler et al (2008). In their study, a set of parameters like temperature, silica concentration, pH, salinity, and biotic components were monitored in five diverse geothermal sites in Iceland, concluding that abiotic-biotic relationship governs the buildup of silica sinter. When water cools, silica is oversaturated and silicic acid

nucleates by polymerization to form colloids of noncrystalline opal-A (Fournier 1985; Williams et al., 1985). The silica particles grow by Ostwald ripening into compact aggregates that become denser than water and tend to settle out of solution (Campbell et al., 2001).

Precipitation occurs in available surfaces. Many studies have determined that microbes provide heterogeneous nucleation sites for the near-vent accumulation of silica (Jones et al 1999; Handley et al. 2005), having a passive role in silica sinter precipitation. Functional groups (OH) on the surface of microbial cells can act as nucleation sites for opal-A (Fox-Powell et al., 2018). However, the specific role of microorganisms in terms of their volumetric contribution to the build-up of the solid sinter deposits is still under discussion (Campbell et al., 2015). According to Konhauser (2001), microstromatolites growing at the Krisuvik hot spring in Iceland contribute a major component to the overall sinter deposit, with approximately half the sinter thickness attributed to silicified microorganisms. In places where cryosilicifation occurs (silicification at freezing temperatures), such as El Tatio, cryogenic and non-freezing silicification mineralize different portions of the microbial consortia. Recent studies determined that non-freezing conditions predominantly captures biofilms, streamer communities, and other benthic organisms. Conversely, cryogenic silicification is likely to more efficiently capture the planktic microorganisms present in the fluid-phase, where ice-formation primarily occurs (Fox-Powell et al., 2018). On the other hand, some authors acknowledge the dominant role of abiogenic processes -rapid cooling driving evaporation and silica oversaturation- in the precipitation of noncrystalline opaline silica (Braunstein and Lowe, 2001).

1.2.3 Mineralogy and textures of siliceous sinter

Previous studies found that El Tatio´s siliceous sinter is mainly composed of opal-A and opal-CT (Fernandez-Turiel et al., 2005, Garcia-Valles et al., 2008; Nicolau et al., 2014). Siliceous sinters elsewhere are composed by opal-A, opal-A/CT, paracrystalline opal-CT, opal-C, moganite and/or quartz. The initial phase that forms from thermal waters is always non-crystalline opal-A, and subsequent phases are formed by postpositional diagenesis, accompanied by with the loss of structural water, porosity, and increment of density (Herdianita et al., 2000; Lynne and Campbell, 2003; Jones and Renaut, 2004; Lynne et al., 2005, 2007, 2008). Accessory minerals such as halite, and sylvite, can also be present in minor quantities. Boron and arsenic minerals such as sassolite [H_3BO_3], nobleite [$CaB_6O_{10}4H_2O$], realgar [AsS] and teruggite [$Ca_4MgAs_2B_{12}O_{22}(OH)_{12}12(H_2O)$] are also reported in El Tatio silica sinters (Garcia-Valles et al., 2008). Silica sinters can also uptake pathfinder elements, as suggested by recent studies (Hamilton et al., 2017; Sanchez-Yanez et al., 2017). For instance, higher concentrations of Au, Ag, As, Ba, Hg, Mo, S, and Tl has been found in sinters from near-vent areas with respect to distal facies in Kohuamuri deposit in Comadere Volcanic Zone, New Zealand (Hamilton et al., 2017). This enrichment is associated with near-neutral alkali chloride waters in active geothermal systems (McKenzie et al. 2001; Pope et al. 2004) and also occurs in the fossilized sinter of the Rhynie cherts, Scotland (Trewin and Rice, 2004). Additionally, Smith et al. (2018) observed high concentrations of Ga (1260 ppm), Ca and As (10 ppm) in "geyser eggs" (smooth, oval, siliceous pebble found in alkali chloride hot pools) surrounding Old Faithful Geyser, Yellowstone National Park, U.S.A., attributing this increment to freezing conditions. On the other hand, Sanchez-Yanez et al. (2017) have addressed that metal enrichment is related to the maturity of siliceous sinter at Puchuldiza geothermal field, northern Chile. While As and B are enriched in the more amorphous silica phase (opal-A/CT), Au and Ag show higher concentrations in more crystalline phases (opal-C/quartz).

The development of sinter textures depends on the hydrodynamic properties of the hot spring, temperature, and biological component of spring water (e.g., Walter, 1976; Cady and Farmer, 1996; Hinman and Lindstrom, 1996; Jones and Renaut, 1997; Campbell et al., 2001; Konhauser et al., 2001; Lowe et al., 2001; Jones et al., 2003; Guidry and Chafetz, 2003; Lynne and Campbell, 2003; Handley et al., 2005; Nicolau et al., 2014). Also, different textures will form depending on the dominant process of silica sinter formation (i.e., evaporation vs. supersaturation), and the state of polymerization, (Tobler et al., 2008; Handley and Campbell, 2011). Sinter facies assemblages may be broadly grouped into three main categories: vent and proximal slope (>65°C), mid-apron (<65–45°C) and distal apron to marsh (<45°C) (Cady and Farmer 1996; Campbell et al., 2015). Furthermore, environmental conditions may influence textures formation. Nicolau et al (2014) showed that freezing-thawing conditions at El Tatio and high evaporation rates trigger the development of microtextures associated with freezing such as micro columns/ridges and silica platelets. These aspects are explored in detail in this thesis, which is described below.

1.3 Objective of the thesis

1.3.1 General goal

The general aim of this thesis is to constrain the absolute age of silica sinters at El Tatio using radiocarbon (^{14}C) dating methods in organic matter trapped within the deposits. These data are used to reconstruct the silica precipitation history in the geothermal field and evaluate the impact of environmental conditions on silica precipitation in high-altitude geothermal systems.

1.3.2 Specific objectives

1- Estimate silica precipitation rates using radiocarbon ages and compare these data with precipitation rates estimated using *in situ* silica precipitation experiments.
2- Study the textures, morphologies, and mineralogy of silica sinter deposits at El Tatio.
3- Study the crystallinity of silica phases and relate it to the age of each sinter sample.

1.4 Hypotheses

1- El Tatio is a long-lived geothermal system, with continued hydrothermal activity since at least the Holocene.

2- Environmental conditions at El Tatio, including extreme daily temperature oscillations, strong winds, and high evaporation rates, exert a strong control on silica precipitation. Silica precipitation is hypothesized to be more pronounced at El Tatio than in geothermal systems elsewhere since these effects are maximized under the high altitude conditions of the Altiplano.

3- Silica sinter crystallinity at El Tatio depends on the aging of these sediments due to fluid-rock interaction, and site-specific diagenesis.

1.5 Thesis structure

This work is centered on the study of silica sinter deposits at the El Tatio geyser field, in northern Chile. The main scope of the thesis is set on discussing the geological observations, the

textural and mineralogical characteristics, and the radiocarbon data of the siliceous sinter deposits. The structure is briefly detailed below.

In Chapter 2, the geological background, methods, results, and discussions are presented. This chapter consists of the manuscript entitled "*Environmental controls on silica sinter precipitation revealed by radiocarbon dating*" published in *Geology* in February 2019. In Chapter 3, the mineralogy and textures of silica sinter are further discussed. Chapter 4 presents the main conclusions of the study.

Additionally, supplementary data are included in the Appendix. Appendix A is the data repository of the manuscript presented in Chapter 2. Appendix B includes additional petrographic observations and XRD spectra of the sinter samples, while Appendix C includes water geochemistry data.

1.6 Publications and conference papers resulting from this work

1.6.1 Peer reviewed article

Silvina Slagter, Martin Reich, Carolina Munoz-Saez, John Southon, Diego Morata, Fernando Barra, Jian Gong, John R. Skok (2019) Environmental controls on silica sinter formation revealed by radiocarbon dating. *Geology* https://doi.org/10.1130/G45859.1 **(Chapter 2).**

1.6.2 Conference abstracts (main project)

Silvina Slagter**,** Martin Reich, Carolina Munoz-Saez, Diego Morata. Dating silica sinter precipitation in hot springs from El Tatio, Chile. XV Congreso Geológico Chileno. November 18-23, 2018. Concepción, Chile.

Silvina Slagter**,** Martin Reich, Carolina Munoz-Saez, Diego Morata, John Southon Carbon-14 dating of silica sinter deposits from El Tatio, Chile. Goldschmidt Conference. August 12-17, 2018. Boston, U.S.A.

Silvina Slagter**,** Martin Reich, Carolina Munoz-Saez. The evolution of silica precipitation at El Tatio Geyser Field. IGCP636 Annual Meeting. November 21, 2017. Santiago, Chile.

Silvina Slagter**,** Martin Reich, Carolina Munoz-Saez (2017) Biological influence on silica sinter precipitation at El Tatio Geyser Field. Astrobiology. November 26-December 1, 2017. Coyhaique, Chile.

1.6.3 Conference abstracts (side projects)

Carolina Munoz-Saez, Silvina Slagter, Michael Manga. Martin Reich, Shaul Hurwitz, Dakota Churchill. ^{14}C from El Tatio geothermal field. XV Congreso Geológico Chileno. November 18-23, 2018. Concepción, Chile.

Carolina Munoz-Saez, Silvina Slagter, Martin Reich, Michael Manga (2017) µXRT imaging of biosignatures in sinter deposits. Astrobiology. November 26-December 1, 2017. Coyhaique, Chile.

Carolina Munoz-Saez, Michael Manga, Dakota Churchill, <u>Silvina Slagter</u>, Shaul Hurwitz, Martin Reich Advection of heat from the El Tatio geothermal system since the late Pliocene. Chapman conference 2018. 07- 12 January 2018, Quinamavida, Maule Region, Chile.

CHAPTER 2: ENVIRONMENTAL CONTROLS ON SILICA SINTER FORMATION REVEALED BY RADIOCARBON DATING

Silvina Slagter[1,2]*, Martin Reich[1,2], Carolina Munoz-Saez[1,2], John Southon[3], Diego Morata[1,2], Fernando Barra[1,2], Jian Gong[4], Jhon Roma Skok[5]

[1]*Department of Geology and Andean Geothermal Center of Excellence (CEGA), FCFM, Universidad de Chile, Plaza Ercilla 803, Santiago, Chile.*

[2]*Millennium Nucleus for Metal Tracing Along Subduction, Universidad de Chile, FCFM, Santiago, Chile.*

[3]*Department of Earth System Science, University of California, Irvine, California 92697, USA.*

[4]*Intitut de Physique du Globe de Paris, CNRS-UMR7154, Paris, France.*

[5] *SETI Institute, Mountain View, California 94043, USA.*

*Corresponding author: Silvina Slagter (sslagter@ing.uchile.cl)
Keywords: geothermal systems, silica sinter, Carbon-14, El Tatio, Chile

2.1 ABSTRACT

Silica sinter deposits overlying geothermal fields are reliable records of environmental, geochemical and biological changes through time. Therefore, determining the absolute ages of formation of these deposits is fundamental to constraining the timing and evolution of processes that have shaped silica precipitation on the Earth's surface. We performed ^{14}C dating of organic matter trapped within silica sinter deposits from the high altitude El Tatio geyser field in the Chilean Altiplano. Radiocarbon ages of stratigraphically controlled samples retrieved from four well-preserved paleosinter mounds range from $10,840 \pm 30$ to 230 ± 35 years B.P., indicating that El Tatio system has had an active discharge of silica-rich chloride springs over at least the past 10,000 years that resulted in the formation of extensive sinter deposits. These ages are used to determine the silica precipitation rate at El Tatio, which was calculated between 0.14 and 2.57 kg/years/m^2. These values are among the highest precipitation rates in geothermal systems where data are available and are consistent with *in situ* silica precipitation experiments at El Tatio (0.84-2.92 kg/years/m^2). Our results indicate that the extreme environmental conditions of the arid Chilean Altiplano, i.e., high evaporation and cooling rate of thermal waters, and significant daily temperature oscillations, play a key role in the construction and preservation of silica sinter deposits.

2.2 INTRODUCTION

Silica sinter deposits are the surface expressions of underlying geothermal systems and form when near neutral thermal waters discharge and cool at the surface, precipitating silica (Lynne et al., 2007, and references therein). They are found near hot springs forming mounds and are targets for exploration of concealed geothermal energy resources and epithermal Au-Ag deposits (Sillitoe, 2015). Sinter deposits have also been the focus of astrobiological investigations (Konhauser et al., 2003, and references therein), and recently the El Tatio geyser field in the Central Andes has been proposed as an early Mars analog environment because of similar siliceous sinter textures observed on the Martian surface (Ruff and Farmer, 2016). El Tatio is one of the world's largest geyser fields and is located in the Chilean Altiplano at an altitude of 4,200 m a.s.l., associated with extreme

environmental conditions including high evaporation rates and daily temperature oscillations that can reach up to 40 °C (Fig. 3). Silica sinter deposits at El Tatio cover an area of 30 km² with more than 200 thermal springs that host active sinters and fossil sinter deposits, i.e., ''paleosinter'', which are mostly concentrated in the upper basin (Fig. 3). This unique setting has motivated studies on the geochemistry and dynamics of thermal fluids, the mineralogy of sinter deposits, and the description of extremophile bacterial communities (Jones et al., 1997; Fernandez-Turiel et al., 2005; Phoenix et al., 2006; Garcia-Valles et al., 2008; Nicolau et al., 2014; Munoz-Saez et al., 2016). Despite these advances, the absolute age of the El Tatio sinter deposits remains unconstrained, limiting our knowledge about the evolution of the geothermal system at depth, the formation of sinter deposits on the surface and the impacts of extreme environmental conditions on the rates of silica precipitation.

Determining the absolute age of silica sinter deposits is challenging. Previous studies have approached to answer this question indirectly, either by relating hydrothermal deposits to glacial ages (White et al., 1988) or through estimations of the time that would be necessary to form the sinter deposits, based on silica precipitation rates determined *in situ* (Nicolau et al., 2014). More recent geochronological studies, in contrast, have used radiocarbon dating techniques (^{14}C) to obtain ages of organic carbon trapped within silica, opening new avenues for dating sinter deposits (Foley et al., 2006; Lynne et al, 2008, 2012; Lowenstern et al., 2016).

In this study, we present thirteen radiocarbon ages of stratigraphically controlled samples retrieved from four well-preserved paleosinter mounds at El Tatio. Our results point to a protracted history of silica precipitation with some of the oldest ^{14}C ages reported so far for active geothermal fields. Our new radiocarbon ages are integrated with field observations and *in situ* experiments to determine the rates of silica precipitation at El Tatio, which point to a strong effect of environmental conditions on the construction of silica sinter deposits in high altitude geothermal systems.

2.3 GEOLOGICAL BACKGROUND

El Tatio geyser field is bounded by a NE half-graben, which control the orientation of most thermal manifestations (Fig. 3). The geyser field comprises extensive paleosinter deposits that precipitated over glacial sediments, and actively forming siliceous sinters with surface manifestations including thermal springs, fumaroles, geysers and mud pools. Most of the hot springs discharge at temperatures close to the boiling point at 4,200 m a.s.l. (~86 °C), and are characterized by near-neutral pH and high alkali chloride and silica concentrations (Cl >8,000 mg/L, Na >3,500 mg/L, and SiO_2 >150 mg/L) (Cusicanqui et al.,1976; Cortecci et al., 2005; Munoz-Saez et al., 2016).

The climate in this area is characterized by a low precipitation rate (<100 mm/year). The mean annual temperature ranges from 8 to 11 °C during the day and day-night temperature variation often reaches 35 °C. In winter the temperature can drop below −30 °C at night (Fernandez-Turiel et al., 2005). Wind direction is predominantly from the west with speeds between 3.7 and 7.5 m/s. The mean annual evaporation rate at El Tatio is 131.9 mm/month, reaching its maximum during December (183.2 mm/month) and a minimum during June (72.8 mm/month) (Nicolau et al., 2014; Data Repository).

These extreme environmental conditions have conditioned microbial life at El Tatio. Microbial communities that usually live in water temperatures close to 40 °C thrive under higher

temperature conditions (>60 °C) due to the high thermal gradient resulting from the strong Altiplano winds (Phoenix et al., 2006).

2.4 SAMPLES AND METHODS

We selected four well-preserved paleosinter mounds that represent former outflow zones in the upper basin (mounds 404, 502, 429, and 408; Fig. 4). We divided each mound from bottom to top in regular intervals (Fig. 5), and retrieved a 5 cm-thick sample at the base of each interval. The number of intervals in each mound depended on the height of the mound and the observed textures. The depositional environments and approximate temperature conditions can be inferred for each textural type by comparing the distinct textures preserved in the sampled paleosinter mounds with examples from modern geothermal settings (Lynne, 2012). The sampled mounds show textures that are characteristic of high-temperature conditions (60 °C) such as geyserite, as well as palisade and laminated textures that are similar to sinter textures described previously at El Tatio, and which represent deposition at middle to low temperature conditions (40-20 °C) (Fig. 15; Nicolau et al., 2014). Detailed examination using polarized light microscopy and scanning electron microscopy (SEM) revealed that all the sinter samples contain remnants of filamentous bacteria and plant fragments (Fig. 16; Fig 17). Bacteria are preserved within the siliceous matrix, which is predominantly opal-A (Fig. 18). Details of the methods can be found in the Data Repository.

Two active geysers in the upper basin (sites 411 and 412) were selected for *in situ* silica precipitation experiments (Data Repository). At 411 site, water is in equilibrium with amorphous silica, while at site 412 sites, the geothermal water is undersaturated with respect to silica according to the equilibrium equation of Gunnarsson and Arnórsson (2000) (Table 6; Fig. 20; Data Repository).

2.5 RADIOCARBON AGES

Radiocarbon and calibrated ages are reported in Table 3. The ages of four paleosinter mounds comprise a time interval between $10,840 \pm 30$ years B.P. and 230 ± 35 years B.P. The oldest mound (mound 404) formed between $10,840 \pm 30$ and $5,860 \pm 25$ years B.P. and corresponds to a 1.5-m-tall structure with a smooth surface. Six intervals were sampled from this mound, with geyserite on top (sample 404a) and laminated and palisade textures at the bottom (samples 404f, e, d, c, and b) (Fig. 4A; Fig. 15). Mound 408 has a height of 0.8 m, with a geyserite texture at the bottom (sample 408b; $7,220 \pm 45$ years B.P.), and a palisade texture at the top (sample 408t; 555 ± 20 years B.P.). Mound 429 is 0.5 m high and has a gentle slope. Two layers are identified in this mound, with ages from $3,720 \pm 70$ years B.P. to $2,625 \pm 20$ years B.P. Lastly, mound 502 has a height of 2.4 m and was divided into three intervals. Radiocarbon dating yielded an age range of $2,220 \pm 15$ to 230 ± 35 years B.P. Laminated textures were found at the base (sample 502b), and geyserite and palisade textures were found in the middle (sample 502m) and top (sample 502t) layers, respectively (Fig. 18). Most of the samples consist of opal-A, which is present in samples younger than 8,000 years B.P. (Fig. 17; Data Repository).

2.6 SILICA PRECIPITATIONS RATES

The silica precipitation rate for each layer within each mound was determined considering the thickness and extent of the layer (Table 4). The thickness of each layer was measured directly

from the mound, and the area was determined using aerial drone imaging (Fig. 4B; Data Repository). The precipitation rate R, in kg/years/m^2, was calculated using $R = \frac{A*\rho}{\Delta t}$, where A is the layer thickness (m), ρ is density, assumed as 1.8 g/cm^3 based on previous density measurements in sinters (Herdianita et al., 2000; Munoz-Saez et al., 2016), and Δt is the difference between the radiocarbon age of two consecutive layers. Silica precipitation rates were calculated considering a continuous precipitation process. In addition, the reported rates are considered minimum values because erosion was not taken into account. Calculated silica precipitation rates for the four paleosinter mounds are between 0.14 and 2.57 kg/years/m^2 (Fig 5; 6). It is worth noting that precipitation rates have varied at a given site through time. Mound 404 has varied from 0.1 to 0.9 kg/years/m^2, and in mound 502 precipitation varies from 1.4 to 2.5 kg/years/m^2 (Fig. 4). Foley (2006) suggested that pulses and pauses in silica sinter formation are due to variations in discharge rates and feature geometry changes. The higher precipitation rates observed in mound 502 may be due to either environmental changes or intrinsic variations in the hydrothermal system at depth.

The *in situ* experimental precipitation rate varies between 0.84 and 2.92 kg/years/m^2 (average 1.86 kg/years/m^2; Table 5), in agreement with previously reported *in situ* rates of 1.3 to 3.4 kg/years/m^2 measured on glass slides (average 2.5 kg/years/m^2; Nicolau et al., 2014). Silica precipitation rates determined for El Tatio are compared with published data for other geothermal systems (Fig. 5; Data Repository). In El Tatio, precipitation rates are among the highest measured in geothermal systems where data are available, reaching a maximum value of 3.4 kg/years/m^2 (average of 2.5 kg/years/m^2; Nicolau et al., 2014), corresponding to *in situ* measurements.

2.7 IMPACT OF EXTREME ENVIRONMENTAL CONDITIONS

The high silica precipitation rates measured at El Tatio raise some fundamental questions concerning the behavior of dissolved silica in thermal waters that discharge on the surface. It is well documented that silica precipitation in geothermal fields is strongly controlled by cooling, pH changes, silica concentration and ionic strength (Hinman and Lindstorm et al., 1996; Guidry and Chafez 2003, and references therein; Tobler et al., 2013). However, when comparing El Tatio to other systems in New Zealand and Iceland, it is noted that factors such as pH, temperature, and silica saturation, do not explain the observed differences in precipitation rates. For example, the pH of discharged waters in all localities is close to 7, except for Geysir, Iceland where more alkaline values have been reported (pH~8.5) (Tobler et al., 2008). Furthermore, the temperature of the thermal fluids is also similar, ranging from 70 to 96 °C. Despite these similarities, the silica content of thermal waters is the lowest at El Tatio, with an average of ~216 ppm SiO$_2$ (Nicolau et al., 2016; this study; Table 6) compared with Champagne Pool (~430 ppm; Handley et al., 2005), Geysir (~360 ppm; Tobler et al., 2008), and Yellowstone National Park, western United States (~750 ppm; Channing and Butler., 2007).

Environmental conditions have been reported to exert a critical influence on silica precipitation and texture development (Lynne, 2012; Nicolau et al., 2014; Campbell et al., 2015b; Sanchez-Yanez et al., 2017; Lynne et al., 2019). Particularly, high evaporation and high cooling rates of thermal waters enhance silica precipitation (Hinman and Lindstorm, 1996). Complete evaporation has been shown to be 7-8 orders of magnitude more efficient than precipitation from a supersaturated solution (Boudreau and Lynne, 2012; Orange et al., 2013). At El Tatio, evaporation is intensified by the high altitude, high wind speed and low atmospheric humidity (Nicolau et al., 2014; Data Repository, Fig. 21). In addition, the cooling rate of thermal waters

caused by the low air temperature is extreme, and drastic variability in temperature gradients along channels can reach ~30 °C within a square decimeter (Dunkel et al., 2009). Furthermore, daily freezing and thawing cycles may also influence silica precipitation by causing the formation of cryogenic opal-A (Fox-Powell et al., 2018). Previous studies at El Tatio have described microtextures (e.g., platelets, microcolumns, and ridges) resulting from freezing-thawing processes (Nicolau et al., 2014). Channing and Butler (2007) reported that during freezing, particles become compressed by ice, physically forcing aggregate formation. The partial freezing of thermal waters also leads to an increase in the concentration of dissolved chemical components (such as Si, Na, and Cl) in the water, enhancing the silica precipitation rate (Fox-Powell et al., 2018).

2.8 CONCLUSIONS AND FURTHER IMPLICATIONS

Our new ages contribute to a better understanding of the geologic history of the El Tatio area, pointing out to a long-lived geothermal system that has been active since at least 10,840 years B.P. Hydrothermal activity at the El Tatio may have begun after the last deglaciation (ca. 20-10 kyr B.P. in the Chilean Altiplano; Blard et al., 2014), and continued uninterruptedly throughout the Holocene.

Our results show that silica precipitation rates at El Tatio, estimated from *in situ* experiments are consistent with silica precipitation rates calculated based on radiocarbon data, and were most likely enhanced by environmental factors such as high evaporation rates and extreme temperature oscillations. Interestingly, our data show some significant secular variations in the silica precipitation rate at El Tatio. In particular, an increase of ~2 kg/year/m^2 is observed within a 2.4-m tall geyser mound in the last 2,000 years (Fig. 6). These variations might have been caused by fluctuations in the concentration of silica in the fluids due to changes in the geothermal system and/or environmental conditions.

Overall, the results presented here indicate that siliceous sinter deposits contain not only mineralogical and biogeochemical information that records the evolution of a geothermal system but are crucial for reconstructing the effects of climate change on silica precipitation, and potentially on the development of extremophiles on Earth, and possibly Mars.

2.9 ACKNOWLEDGMENTS

2.10 REFERENCES CITED

Blard, P.-H., Lavé, J., Farley, K.A., Ramirez, V., Jiménez, N., Martin, M., Charreau, J., Tibari B., Fornari L.C.P, 2014, Progressive glacial retreat in the Southern Altiplano (Uturuncu volcano , 22 ° S) between 65 and 14 ka constrained by cosmogenic ^{3}He dating: Quaternary Research, v. 82, p. 209-221.

Boudreau, A.E., Lynne, B.Y., 2012, The growth of siliceous sinter deposits around high-temperature eruptive hot springs: Journal of Volcanology and Geothermal Research, v. 247–248, p. 1–8.

Braunstein, D.G., Lowe, D.R., 2001, Relationship between spring and geyser activity and the deposition and morphology of high temperature (&73 °C) siliceous sinter, Yellowstone National Park, Wyoming, U.S.A.: Journal of Sedimentary Research, v. 71, p. 747–763.

Campbell K.A., Guido, D.M., Gautret, P., Foucher F., Ramboz C., Westall F., 2015, Geyserite in hot-spring siliceous sinter: Window on Earth's hottest terrestrial (paleo) environment and its extreme life: Earth-Science Reviews, v. 148, p. 44- 64.

Channing, A., Butler, I.B., 2007, Cryogenic opal-A deposition from Yellowstone hot springs: Earth and Planetary Science Letters, v. 257, p. 121–131.

Cortecci, G., Boschetti, T., Mussi, M., Herrera Lameli, C., Mucchino, C., Barbieri, M., 2005, New chemical and original isotopic data on waters from El Tatio geothermal field, northern Chile: Geochemical Journal, v. 39, p. 547–571.

Cusicanqui, H., Mahon, W.A.J., Ellis, A.J., 1975, The geochemistry of the El Tatio Geothermal Field, northern Chile: Proceedings, Second United Nations Symposium on the Development and Use of Geothermal Resources, San Francisco, p. 703–711.

Dunckel AE, Cardenas MB, Sawyer AH, Bennett PC, 2009, High resolution in-situ thermal imaging of microbial mats at El Tatio Geyser, Chile shows coupling between community color and temperature: Geophysics Research Letters, v. 36, p. 23403.

Fernandez-Turiel, J.L., Garcia-Valles, M., Gimeno-Torrente, D., Saavedra-Alonso, J., Martinez Manent, S., 2005, The hot spring and geyser sinters of El Tatio, northern Chile: Sedimentary Geology, v. 180, p. 125–147.

Foley, D., 2006, Dating castle geyser: preliminary results and broad speculations on the geologic development of geysers and hydrothermal systems in Yellowstone national park, Wyoming: USA. Transaction of Geothermal Resources Council, v. 30 (I), p. 413–417.

Fox-Powell M.G., Channing A., Applin D., Cloutis E., Preston L.J., Cousins C.R., 2018, Cryogenic silicification of microorganisms in hydrothermal fluids: Earth and Planetary Science Letters, v. 498, p. 1-8.

Garcia-Valles, M., Fernandez-Turiel, J.L., Gimeno-Torrente, D., Saavedra-Alonso, J., Martinez-Manet, S., 2008, Mineralogical characterization of silica sinters from the el Tatio geothermal field, Chile: American Mineralogist, v. 93, p. 1373–1383.

Guidry, S.A., Chafetz, H.S., 2003, Depositional facies and diagenetic alteration in a relict siliceous hot spring accumulation: examples from Yellowstone National Park, U.S.A.: Journal of Sedimentary Research, v. 73, p. 806–823.

Gunnarsson, I. and Arnórsson, S., 2000, Amorphous silica solubility and the thermodynamics properties of H4SiO4° in the range of 0° to 350°C at P_{sat}: Geochimica et Cosmochimica Acta, v. 64, p. 2295– 2307.

Handley, K.M., Campbell, K.A., Mountain, B.W., Browne, P.R.L., 2005, Abiotic–biotic controls on the origin and development of spicular sinter: in situ growth experiments, Champagne Pool, Waiotapu, New Zealand: Geobiology, v. 3, p. 93–114.

Herdianita, N.R., Browne, P.R.L., Rodgers, K.A., and Campbell, K.A., 2000, Mineralogical and textural changes accompanying ageing of silica sinter: Mineralium Deposita, v. 35, p. 48–62.

Hinman, N.W., and Lindstorm, R.F., 1996, Seasonal changes in silica deposition in hot spring systems: Chemical Geology, v. 132, p. 237–246.

Jones, B., Renaut, R.W., 1997, Formation of silica oncoids around geysers and hot springs at el Tatio, northern Chile: Sedimentology, v. 44, p. 287–304.

Konhauser, K.O., Phoenix, V.R., Bottrell, S.H., Adams, D.G., Head, I.M., 2001. Microbial–silica interactions in Icelandic hot spring sinter: possible analogues for some Precambrian siliceous stromatolites: Sedimentology, v., 48, p. 415–433.

Konhauser, K.O., Jones, B., Reysenbach, A., Renaut, R.W., 2003, Hot spring sinters: keys to understanding Earth's earliest life forms: Canadian Journal of Earth Sciences, v. 40, p. 1713–1724.

Lowenstern, J. B., Hurwitz, S., McGeehin J.P., 2016, Radiocarbon dating of silica sinter deposits in shallow drill cores from the Upper Geyser Basin, Yellowstone National Park: Journal of Volcanology and Geothermal Research, v. 310, p. 132-136.

Lynne, B.Y., Campbell, K.A., James, B., Browne, P.R.L., Moore, J.N., 2007, Tracking Crystallinity in Siliceous Hot-Spring Deposits: American Journal Sciences, v. 307, p. 612–641.

Lynne, B.Y., Campbell, K.A., Moore, J.N., Browne, P.R.L., 2008, Origin and evolution of the Steamboat Springs siliceous sinter deposit, Nevada, U.S.A: Sedimentary Geology, v. 210, p. 111–131.

Lynne, B. Y., 2012, Mapping vent to distal- apron hot spring paleo-flow pathways using siliceous sinter architecture: Geothermics, v. 43, p. 3-24.

Lynne, B. Y., Boudreau, A., Smith, I. J., Smith G. J., 2019, Silica accumulation rates for siliceous sinter at Orakei Korako geothermal field, Taupo Volcanic Zone, New Zealand: Geothermics, v. 78, p. 50-61.

Mountain, B.W., Benning, L.G., Boerema, J., 2003, Experimental studies on New Zealand hot spring sinters: Rates of growth and textural development: Canadian Journal of Earth Sciences, v. 40, p. 1643–1667.

Munoz-Saez, C., Saltiel, S., Manga, M., Nguyen, C., Gonnermann, H., 2016, Physical and hydraulic properties of modern sinter deposits: El Tatio, Atacama: Journal of Volcanology and Geothermal Research, v. 325, p. 156-168.

Munoz-Saez, C., Manga, M., Hurwitz, S., 2018, Hydrothermal discharge from the El Tatio basin, Atacama, Chile: Journal of Volcanology and Geothermal Research, v. 325, p. 25-35.

Nicolau, C., Reich, M., Lynne, B., 2014, Physico-chemical and environmental controls on siliceous sinter formation at the high-altitude El Tatio geothermal field, Chile: Journal of Volcanology and Geothermal Resources, v. 282, p. 60–76.

Orange, F., Lalonde, S.V., Konhauser K.O., 2013, Experimental Simulation of Evaporation-Driven Silica Sinter Formation and Microbial Silicification in Hot Spring Systems: Astrobiology, v. 13, p. 163-176.

Phoenix, V.R., Bennett, P.C., Engel, A.S., Tyler, S.W., Ferris, F.G., 2006, Chilean high-altitude hot spring sinters: a model system for UV screening mechanisms by early Precambrian cyanobacteria: Geobiology, v. 4, p. 15–28.

Ruff and Farmer, 2016, Silica deposits on Mars with features resembling hot spring biosignatures at El Tatio in Chile: Nature Communications, v. 7, 13554.

Sanchez-Yañez, C., Reich, M., Leisen, M., Morata, D., Barra, F., 2017, Geochemistry of metals and metalloids in siliceous sinter deposits: Implications for elemental partitioning into silica phases: Applied Geochemistry, v. 80, p. 112-123.

Sillitoe, R.H., 2015, Epithermal paleosurfaces: Mineralium Deposita, v. 50, I. 7, p.767-793.

Tobler, D.J., Stefansson, A., Benning, L.G., 2008, In situ grown silica sinters in Icelandic geothermal areas: Geobiology, v. 6, p. 481–502.

Tobler, D.J., Benning, L.G., 2013. In situ and time-resolved nucleation and growth of silica nanoparticles forming under simulated geothermal conditions: Geochimica et Cosmochimica Acta, v. 114, p. 156-168.

White, D.E., Hutchinson, R.A., and Keith, T.E.C., 1988, The geology and remarkable thermal activity of Norris Geyser Basin, Yellowstone National Park, Wyoming: U.S. Geological Survey, Professional Paper 1456, 84 p.

2.11 FIGURES
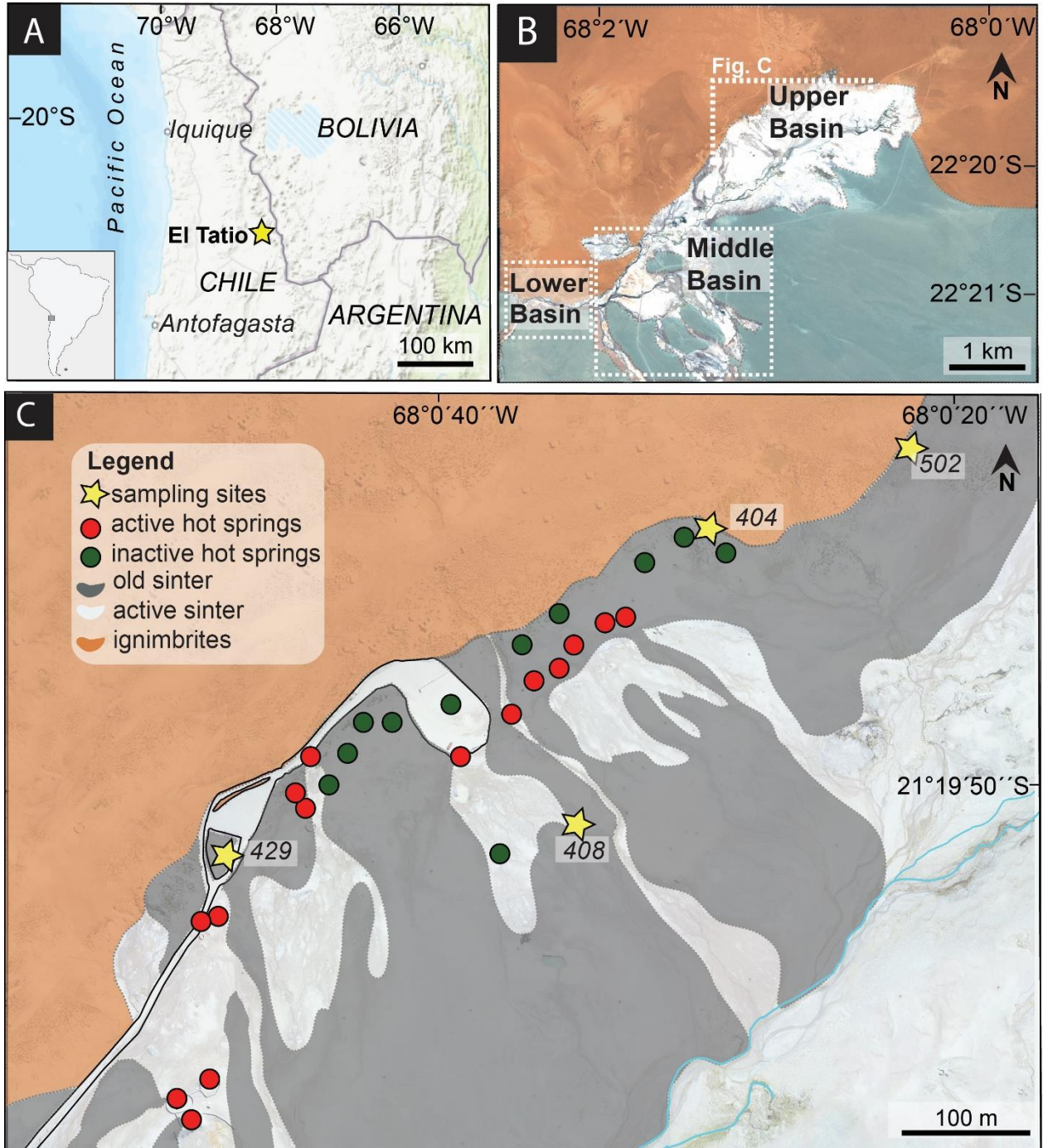
Figure 3. A. Location of the El Tatio geyser field in the Chilean Altiplano. B. Map of El Tatio showing the lower, middle and upper basins in a satellite image. White: silica sinter deposits; Light green: glacial deposits. Orange: ignimbrites. Modified from Munoz-Saez et al. (2018). C. Map of the upper basin (white rectangle in B). Black lines are roads. Light blue lines are natural water courses. Mapping of surface thermal manifestations is overlain on a Drone image obtained in April 2017.
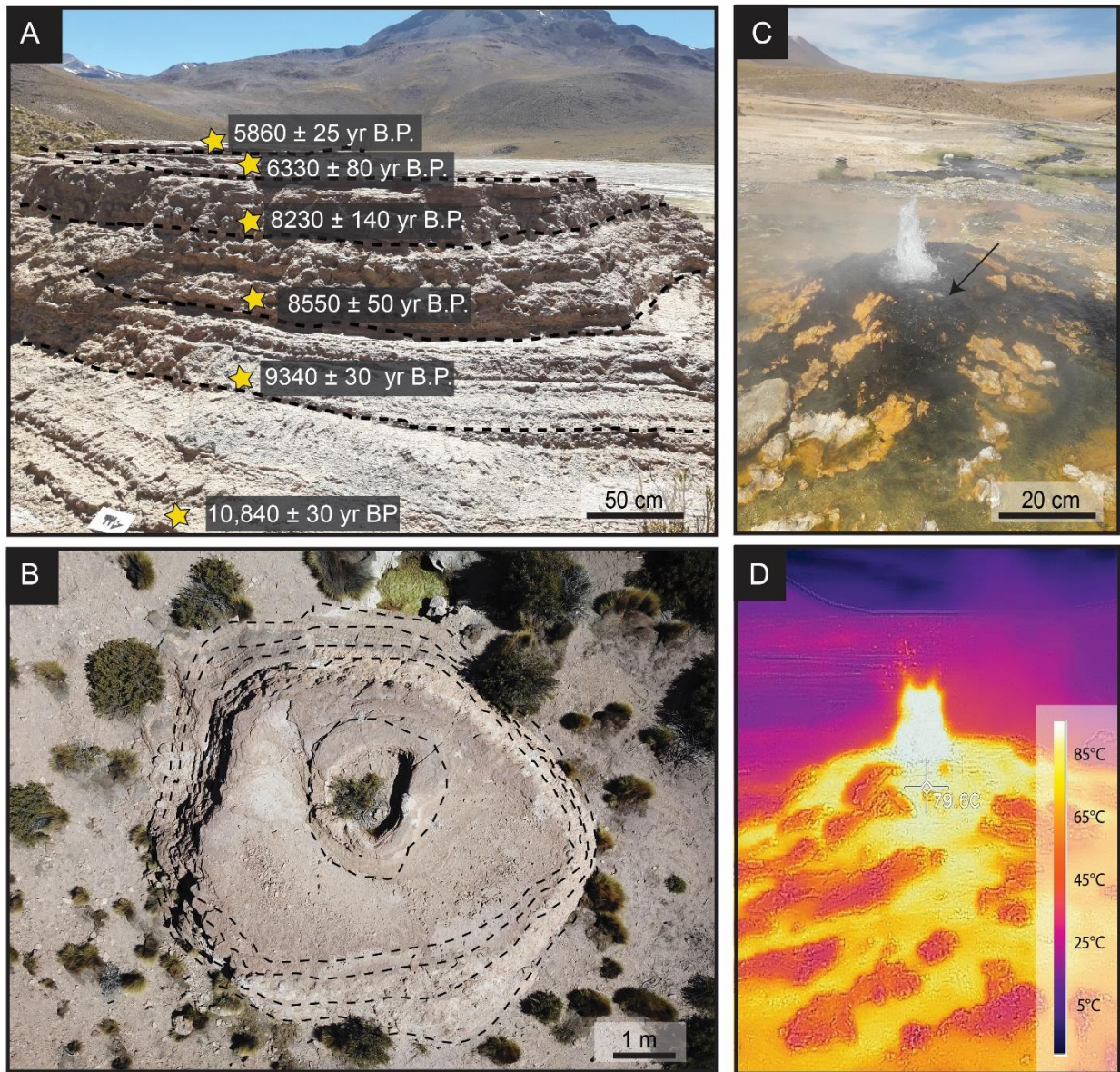
Figure 4. A. Paleosinter mound 404 with radiocarbon ages (in the El Tatio geyser field, Chilean Altiplano). Dashed lines represent the limits of each interval dated. Yellow stars are sampling sites. B. Aerial drone image of mound 404 with dashed lines representing the limits of each interval. For drone image details see Supplementary Text. C. *In situ* precipitation experiment at the active geyser site 411. The black arrow points to the place where the sandpaper sheets were placed (see the Data Repository experimental methods). D. Thermal image of the same geyser mound in C, obtained with forward-looking infrared (FLIR) camera. The temperature of thermal water at the experimental site was 78.8 °C.
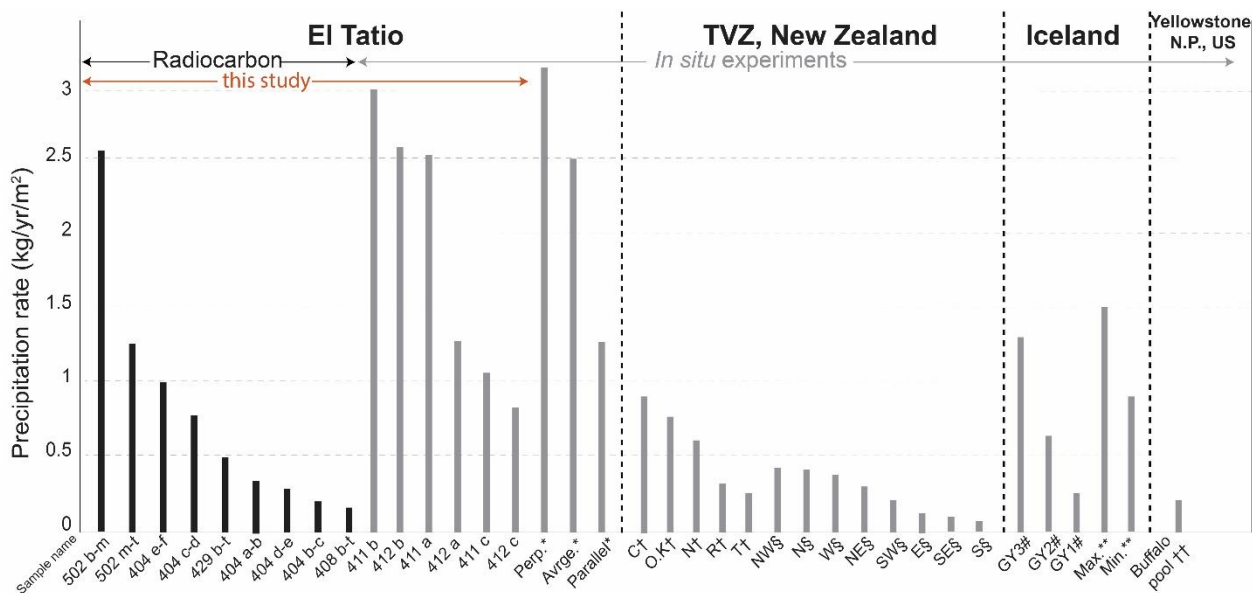
Figure 5. Comparison between silica precipitation rates at El Tatio (Chilean Altiplano) and those at other geothermal systems, estimated using radiocarbon data (black) and *in situ* precipitation experiments (grey). Suffixes correspond to intervals between two samples. [*]Nicolau et al. (2014); [†]Mountain et al. (2003); [§]Handley et al. (2005); [#]Tobler et al. (2008); [**]Konhauser et al (2001); [††] Braunstein and Lowe (2001). Compass directions correspond to names of samples in Handley et al. (2005). Perp: perpendicular to water flow, Avrge.: average, Parallel: parallel to water flow, TVZ: Taupo Volcanic Zone, C: Champagne pool, O.K: Orakei Korako, N: Ngatamariki, R: Rotokawa, T.: Tokaanu, N: north, NW: north-west. NP: National Park; Max.—maximum; Min.—minimum.
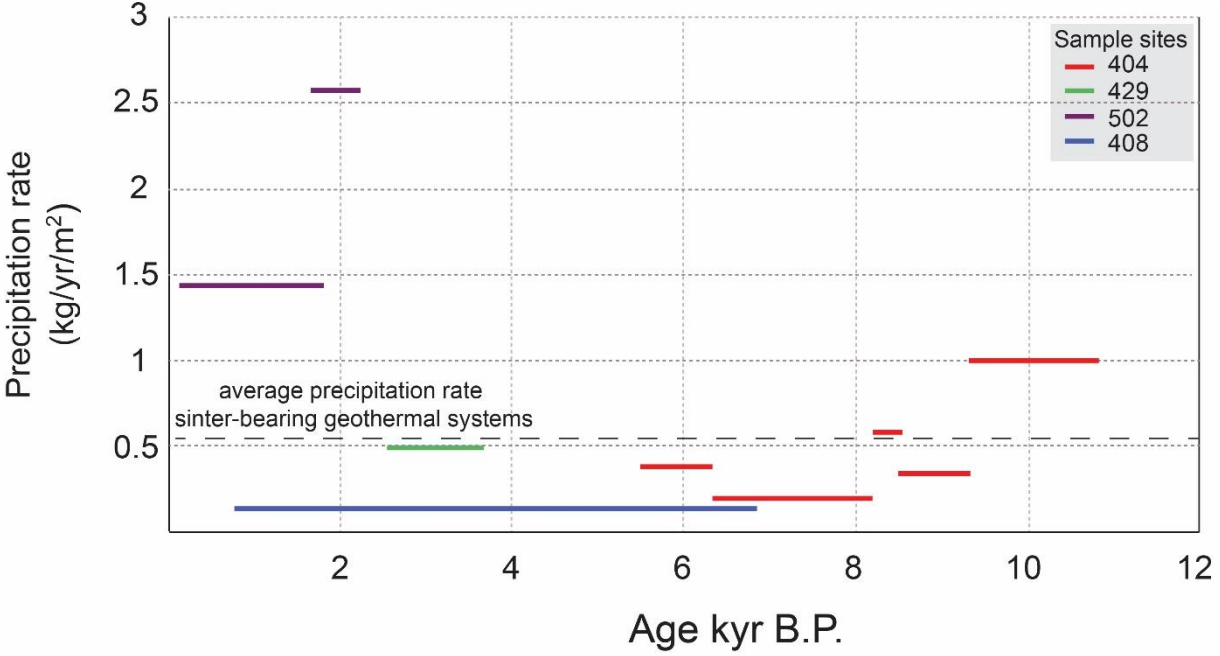
Figure 6. Silica precipitation rates at El Tatio (Chilean Altiplano) estimated using radiocarbon ages and plotted as a function of time. Average rate corresponds to a global average, including data in Figure 5.

19

CHAPTER 3: GEYSER MOUND FORMATION AND SILICA SINTER MATURATION AT THE EL TATIO: INSIGHTS FROM TEXTURAL, MINERALOGICAL, AND RADIOCARBON DATA

3.1 ABSTRACT

Silica sinter deposits at El Tatio in northern Chile preserve textures that reflect the dynamics of the geothermal system in the geological past. The well-exposed stratigraphy and well-preserved sedimentary facies of the sinters, along with radiocarbon (^{14}C) ages, provide a unique scenario to better understand the hydrodynamic changes recorded in the sinter and the diagenetic processes influencing silica maturation. ^{14}C ages obtained in both, paleogeyser mounds and sinter samples obtained throughout the whole geothermal field are combined with field mapping, macro-textural observations, scanning electron microscopy (SEM), X-ray diffraction (XRD) and micro-Raman analyses. The geochronological data show a dynamic record of hydrothermal activity for the last 15,042 years B.P. Sinter textures such as geyserite and palisade, similar to those found in actively forming sinter and ancient hot-spring deposits elsewhere, were identified in paleosinter, revealing ancient geyser activity. A link between the ^{14}C age and XRD and micro-Raman data of the sinter mounds indicate that opal-A phases are dominant across the whole age spectra, confirming the previously reported low degree of crystallinity of El Tatio sinters. However, a subtle diagenetic trend from opal-A to opal-A/CT is observed as a function of increasing age. The results presented here point to a complex mineralogical evolution of sinter mounds at El Tatio, where silica maturation is most likely associated with dissolution and reprecipitation processes.

3.2 INTRODUCTION

Silica sinters are common surface deposits in geothermal fields throughout the world. Mostly, they are produced by near-neutral alkali-chloride hot springs derived from deep reservoirs with temperatures in excess of 175°C (Fournier and Rowe, 1966). Sinters persist long after surficial thermal activity has ceased, and therefore they are used as exploration vectors towards concealed high-enthalpy geothermal systems and epithermal Au-Ag deposits (White et al., 1989; Hamilton et al., 2017; Taksavasu et al., 2018). Silica sinter deposits can also record the hydrodynamic and geochemical conditions at the time of deposition, with a myriad of textures useful for paleoenvironmental interpretations. Mapping the spatial distribution of sinters can reveal, for instance, where alkali chloride-rich fluids discharged at the surface, with the spatial extent and thickness of the sinter also indicating the relative amount of fluid discharged. Additionally, the spatial distribution of textures reveals the location of high-temperature vents and lower temperature flow pathways.

Silica deposition can be mediated by mineral-microbe interactions, as recognized by Weed (1989), where microbes provide a substrate upon which silica can nucleate and aggregates. Consequently, the resulting sinter deposits may contain valuable information about mineral–microbe associations in geothermal systems (e.g. Cady and Farmer, 1996; Farmer, 2000). Also, organic carbon trapped within silica sinter allows dating these materials using radiocarbon (^{14}C) methods. The first studies that obtained absolute ages in silica sinter deposits focused on separate plant and pollen fragments from the silica matrix (Steamboat Spring, U.S.A, Lynne et al., 2008;

Opal Mound, U.S.A, Lynne et al., 2005; Te Kopia, New Zealand, Martin et al., 2000). However, more recent studies have applied a technique that involves dissolving the silica matrix with HF for separating the organic matter fraction. This technique allows collecting a larger fraction of preserved organic matter, including bacteria filaments (e.g., Yellowstone N.P., U.S.A, Lowenstern et al., 2016; and Mangatete, Taupo Volcanic Zone; Drake et al., 2014).

When siliceous sinter forms, the phase that initially precipitates is opal-A. As a result of dissolution, reprecipitation and recrystallization processes, opal-A can mature to form opal-A/CT, paracrystalline opal-CT, opal-C, and quartz (Cady and Farmer, 1996; Campbell et al., 2001; Guidry and Chafetz, 2003; Lynne and Campbell, 2003; Lynne and Campbell, 2004, and Lynne et al., 2005). These changes are accompanied by morphological changes and constitute a maturation or diagenetic process (Lynne et al., 2005). Maturation of sinter is important because it commonly obliterates the original depositional fabrics in hot-spring systems (Guidry & Chafetz, 2003; Lynne and Campbell, 2003, 2004), thereby destroying valuable palaeoecological evidence as silicified microbes and other biotic remains (Rodgers and Cressey, 2001; Lynne and Campbell, 2003, 2004; Jones and Renaut, 2004; Lynne et al., 2005).

Mineralogical maturation of siliceous sinters can be tracked using powder X-ray diffraction (XRD), electron backscatter diffraction (EBSD), Fourier-transform infrared spectroscopy (FTIR) and Raman spectroscopy (Rodgers et al., 2003; Lynne et al., 2007; Garcia-Valles et al., 2008). XRD analysis is commonly used as a tool to quantify the degree of structural order/disorder, by measuring the width of the diffraction peaks. Non-crystalline opal-A and opal-A/CT produce XRD spectra with characteristic wide peaks, or broadbands, while para-crystalline opal-CT and opal-C and microcrystalline quartz produce traces with increasingly sharper, narrower peaks (Lynne et al., 2007). The Full Width at Half Maximum (FWHM) parameter corresponds to the measured wideness of the broadband at half of the maximum intensity and is used to compare the degree of structural disorder between different non-crystalline phases. Typical FWHM values for opal-A, opal-A/CT, opal-CT, opal-C and quartz in sinters are 7.5 °2Θ, 4.5 °2Θ, 1.8 °2Θ, 0.6 °2Θ and 0.3 °2Θ, respectively (Lynne et al., 2007).

The transition from opal-A to micro-crystalline quartz in sinter has been proposed to be time-dependent. Herdianita (2000) studied sinter samples from New Zealand and proposed a model for ageing of siliceous sinter in relation to their mineralogy. Lynne (2005) studied the Opal Mound sinter in Roosevelt Hot Springs, U.S.A., finding that the transition from one phase to the next is gradual and that sometimes two consecutive silica phases co-exist. However, more recent studies have provided evidence that sinter diagenesis is not time-controlled, which is illustrated by the presence of quartz (the diagenetically most mature silica phase) in two siliceous sinter deposits of very different ages. The relatively old Steamboat Springs sinter ($11,493 \pm 70$ years; Lynne et al., 2008) and the much younger Opal Mound sinter ($1,920 \pm 160$ and $1,630 \pm 90$ years; Lynne et al., 2005) are both composed by opal-A, opal-A/CT, opal-CT, opal-C, moganite, and quartz.

Burial heat, pressure, temperature, pore fluid flow, water chemistry, and other environmental factors represent important variables controlling the maturation time of silica sinters (Lynne et al., 2007). The transformation from opal-A to opal-CT is typically accompanied by textural changes although the mineralogical changes may outpace textural maturation (Lynne et al., 2007; Liesgang 2018). Morphological changes were well described by Lynne (2005). In their study, the preserved diagenetic process began with individual ~8µm diameter smooth opal-A micro-spheres that formed botryoidal aggregates when the micro-spheres merge together. Then, in the transition to opal-CT, aligned nano-spheres join to form jagged plates. Opal-CT commonly forms lepispheres that are

similar in size to the opal-A microspheres (Herdianita et al., 2000; Campbell et al., 2001). Reorganization of blades into opal-C elongate, randomly oriented clusters of nano-rods, ending with quartz micro-crystals (Rodgers et al., 2004). In addition to opal-C and quartz, moganite can occur in mature sinters (Rodgers and Cressey, 2001). Moganite (SiO_2) is a distinctive monoclinic polymorph of microcrystalline silica present in the majority of samples of microcrystalline quartz (Heaney and Post, 1992; Herdianita et al., 2000). Rodgers and Cressey (2001) found that moganite forms < 13 vol. % of the SiO_2 phases in New Zealand sinters >20,000 and < 200,000 years old. In general, they found it to be patchily distributed through the quartz-dominated Pliocene sinters in New Zealand (Rodgers et al., 2003). Moganite is indistinguishable from quartz in powder XRD diffractogram without special analytical procedures (Heaney and Post, 1992); hence, the two are best differentiated by their Raman spectra (Rodgers and Cressey, 2001).

Nicolau et al. (2014) and Sanchez-Yanez et al. (2017) provide evidence that sinter deposits from high-altitude geothermal fields in the Andes have some of the world's highest degrees of structural disorder. Amorphous silica phases from the high-altitude Puchuldiza field (~4200 m a.s.l) are characterized by some of the highest FWHM values reported in the literature (7-9.52°2Θ), in agreement with previous values reported by Nicolau et al. (2014) at El Tatio (~4270 m a.s.l.). Compared with XRD data of sinters samples from Steamboat Spring and Opal Mound, both in the US, occurring at ~1400 m a.s.l and ~1840 m a.s.l, respectively, and from the Taupo Volcanic Zone, New Zealand (Te Kopia ~410 m a.s.l, Waiotapu ~380 m a.s.l, Orakei Korako ~350 m a.s.l, and Sinter Island ~320 m a.s.l), the representative median values of FWHM for high-altitude active sinters are above 9, while for active sinter deposits at lower altitudes FWHM values are commonly below 9. Coincidently, the highest FWHM value (12.5°2Θ) corresponds to El Tatio sinter, which is located at the highest altitude, while the lowest FWHM value (6°2Θ).

Mineral transitions from opal-A to quartz have also been observed in the Martian surface indicating different paleoenvironments (Ruff and Farmer, 2016; Sun et al., 2018). The apparent persistence of opal-A on Mars over long timescales has been taken to indicate limited water availability on that planet over the past several billion years (Tosca and Knoll, 2009), although more geochemically mature silica phases such as opal-CT and even trydimite have recently been identified at Gale crater (Morris et al., 2016). Distinguishing opal types is important for understanding relative differences in biosignature preservation potential for various siliceous deposits on Mars (Cady and Farmer, 1996; Konhauser et al., 2003). Biosignatures in rocks containing more crystalline hydrated silica (e.g., opal-CT and quartz) may be more susceptible to textural overprinting or dissolution by fluids during opal maturation compared with less-altered deposits that retain opal-A (Campbell et al., 2015a; Jones and Renaut, 2003a).

El Tatio geothermal system in the Altiplano of northern Chile comprises extensive paleosinter deposits that precipitated over glacial sediments, and actively forming siliceous sinters with more than 200 surface manifestations including thermal springs, fumaroles, geysers, and mud pools. The mineralogical variability of El Tatio active sinters has been previously studied in three different environments: geyser mounds, hot springs and distal aprons (Fernandez-Turiel et al., 2005; Garcia-Valles et al., 2008). According to these studies, siliceous sinter deposits at El Tatio are mainly composed of non-crystalline silica phase, opal-A, with a minor occurrence of para-crystalline phases (opal-A/CT and opal-CT; Fernandez-Turiel et al., 2005; Garcia-Valles et al., 2008). Their chemical composition shows variable concentrations of Cl, Na, Ca, S, As, Sb and B (5–20 wt%; Fernandez-Turiel et al., 2005; Landrum et al., 2009). Mineralogical studies reveal the common occurrence of accessory minerals such as halite [NaCl], sylvite [KCl], realgar [AsS], cahnite [$Ca_4B_2As_2O_{12} \cdot 4(H_2O)$] (Nicolau et al., 2014), and the rare occurrence of nobleite

[CaB$_6$O$_{10}$·4H$_2$O], teruggite [Ca$_4$MgAs$_2$B$_{12}$O$_{22}$(OH)$_{12}$.12(H$_2$O)] and sassolite [H$_3$BO$_3$] (Rodgers et al., 2002; Garcia-Valles et al., 2008).

The relationship between the silica mineralogy and age of the sinter deposits at El Tatio has never been investigated due to the lack of absolute dating in these deposits. In the light of the new radiocarbon (^{14}C) data presented by Slagter et al. (2019), which document at least 10,800 years of sinter formation at El Tatio, the aim of this study is to evaluate the distribution and character of the varied paleosinter facies associations, together with their mineralogy and age. The timing of texture formation and silica maturation in former outflow zones is investigated by combining stratigraphically controlled ^{14}C ages with field mapping, macro-textural observations, SEM observations, and XRD and micro-Raman analyses.

3.3 GEOLOGIC BACKGROUND

El Tatio is located in the Altiplano of northern Chile, at more than 4200 m a.s.l. Hydrothermal deposits or sinter occur on top of Miocene to Holocene sequences of lavas and ignimbrites and glacial deposits (Lahsen and Trujillo, 1975). The area is surrounded by volcanoes, with no historical eruptions. The geothermal field is located in a hemigraben with an orientation NE-SW. Hydrogeological models proposed that meteoric waters are recharged through deep faults at higher altitude ~15 to 20 km to the east of El Tatio (Giggenbach, 1978; Munoz-Saez et al., 2018) and are then heated along the flow path (Lahsen, 1976). Thermal water discharges at El Tatio have near neutral pH, are alkali-chloride in composition and display high concentrations of dissolved silica (SiO$_2$: 150 mg/L), arsenic (As: 30 mg/L), boron (B: 50 mg/L) and antimony (Sb: 1.5 mg/L; Landrum et al., 2009).

Glennon and Pfaff (2003) characterized El Tatio thermal features and divided the 30 km^2 area of silica sinter deposits into three main zones: upper, middle and lower basin. Diverse thermal features have been reported, including geysers, springs, perpetual spouters, mud pools, mud volcanoes, and fumaroles, concluding that the greatest number of eruptive springs and inactive geyser cones occur at the upper basin (Fig. 7C). A variety of biological communities of green bacteria, cyanobacteria, and diatoms thrive in the hot springs that form sinter deposits, largely dependent on the physicochemical features of the thermal waters (Fernandez-Turiel et al., 2005). Recent studies at El Tatio suggest that the distribution of microbial matter control the pore structure, and thus hydraulic and physical properties of silica sinter (Munoz-Saez et al., 2016).

Sinter deposits form an array of mounds, geyser cones, pool-rim dams, and complex sinter aprons characterized by shallow terraced pools (Jones and Renaut, 1997). The extreme climatic conditions at El Tatio such as high altitude, high evaporation rates, and large daily temperature oscillations have been reported to exert a strong influence on silica precipitation (Garcia-Valles et al., 2008; Nicolau et al., 2014; Sanchez-Yanez et al., 2017).

3.4 METHODS

A field mapping and sampling campaign were conducted in November 2016. Mapping of the surface manifestation was undertaken using a differential GPS, and high-resolution aerial images of the field were taken using a drone (DJI Mavic Pro). Four paleogeyser mounds (13 samples) along with 8 surface samples were studied.

Powder X-ray diffraction (XRD) was used to determine the mineralogy of the siliceous sinter. The analyses were carried out in a Siemens Diffractometer model D-5000, in the Physics Department of the Universidad de Chile. The untreated powder samples (<200 mm) were scanned at a rate of 0.6°2/min, with a step size of 0.01°, from 0 to 40°2, and operating conditions of 40 kV and 30 mA. Accessory minerals were identified using the XPowder12 software. For each sample, the Full Width at Half Maximum (FWHM) was measured by fitting the curve and base line manually (Lynne et al., 2007). The FWHM value of the XRD diffraction band is a measure of the degree of lattice ordering within each silica phase. A narrowing of the diffraction band decreases the FWHM value and represents increased structural ordering. For example, unaltered opal-A broadband has a FWHM value of ~8°2θ while a quartz sinter has a FWHM value of~0.2°2θ (Lynne et al., 2005). XRD diffraction bands for opal-A are centered at 22.2°2θ, for opal-CT and opal-C at 21.75°2θ, and for quartz at 20.9°2θ.

In order to obtain morphological and textural data, sinter samples were examined using a FEI Quanta 250 SEM (Thermo Fisher Scientific) at the Andean Geothermal Center of Excellence (CEGA), Universidad de Chile, Santiago, Chile. The SEM is equipped with secondary electron (SE) and backscattered electron (BSE) detectors, and an energy–dispersive X-ray spectrometer (EDS). The analyses were performed using a spot size of 1 to 3 m, an accelerating voltage of 5 to 20 keV, a beam intensity of 80 mA, and a working distance of 10 mm. High–resolution imaging of micro- to nano-sized inclusions was achieved using field-emission scanning electron microscopy (FE-SEM). Observations were performed using a FEI Quanta 250 FEG at the Center for Research in Nanotechnology and Advanced Materials (CIEN) at the Pontificia Universidad Católica de Chile, Santiago, Chile. The FESEM is equipped with in–column detector (ICD) for SE and BSE, and an EDS detector. Operating conditions included an accelerating voltage of 20 kV, spot size was ~4 μm in diameter, takeoff angle ~35°–37°, and the live time was 45 s and a working distance of ~10 mm.

Micro Raman spectroscopy measurements were performed using a Renishaw micro-Raman (RM 1000) system, at the Department of Chemistry, Universidad de Chile, Santiago. The micro Raman system is equipped with a laser (lines 514, 633 and 785 nm), a Leica optical microscope (model DM LM) and an electrically cooled CCD camera. The Raman signal was calibrated to the 520 cm^{-1} line of Si wafer and a 50X objective. Laser power was less than 2 mW. The resolution was set to 4 cm^{-1} and 1-10 scans between 10 and 20s per accumulation. Spectral data were obtained using the 785 nm laser line and were recorded between 100 and 1000 cm^{-1}. Analytical data processing was performed with CrystalSleuth software (Laesch and Downs, 2006).

The samples were analyzed for ^{14}C at the UC Irvine Keck-CCAMS facility. The age is reported as before present (BP), where present is AD 1950 (Stuiver and Polach, 1977). Calibrated ages obtained on CALIB (http://calib.qub.ac.uk) using the SHCal13 dataset (Hogg et al., 2013) are also reported. Calibrated ages are presented as mean ages with a 2σ confidence level. All results were corrected for isotopic fractionation using δ^{13}C values measured with the AMS spectrometer, but these may differ from the isotope ratios of the original material due to fractionation during AMS sample preparation and/or the measurement itself and are not reported. However, seven samples had a sufficient quantity of carbon collected from the combustion to prepare a separate aliquot of CO_2 for δ^{13}C analysis, by stable isotope ratio mass spectrometer (IRMS). δ^{13}C values for those samples were measured to a precision of <0.1‰ relative to PDB, using a Thermo Finnigan Delta Plus IRMS with Gas Bench input at UC Irvine (Table 1). For further details, see Appendix A.

3.5 RESULTS
3.5.1 Sinter textures

Paleogeyser mounds and discharge aprons are distributed within the same area where active discharge zones are found (Fig. 7C). Three distinct sedimentary facies are distinguished according to its formation temperature: low temperature, middle temperature and high-temperature facies (cf. Cady and Farmer, 1996; Lynne, 2012; Campbell et al., 2015b). Different textures were identified for each facies, which are described below.

Low-temperature facies (25-45°C)

Low-temperature facies correspond to sinter aprons (Fig. 8A) and include palisade and plant-rich textures (Fig. 9 and 10, respectively). Most of the samples (12 out of 21) in this study correspond to low-temperature facies (Table 2). Palisade texture is composed by silicified filamentous microbes that range from 10 to 200 µm in length and are 2-5 µm in diameter. Dense vitreous silica layers are also composed of opal-A spheres. SEM textural analysis reveals the hollow nature of many tubules (Fig. 9D). Plant-rich texture originates by silicification of plant material (Lynne, 2012). Stems up to 10 mm in diameter and several centimeters long impart high porosity to the sample. The organic matter is cemented by fine-grained silica. These fragments may have formed *in situ,* or may have been transported by the wind, and later silicified.

Middle-temperature facies (45-65°C)

The mid- to low-temperature sinter facies constitutes an extensive outcrop area of the El Tatio geyser field (Fig. 8A). Discontinuous horizons of apron sinter textures interbedded with high-temperature facies are observed. Also, beading plane features occur all over the field, indicating deposition of terrace fronts from thermal springs. Mid-temperature discharge channels also include bubble mat sinter, which is originated by the silicification of microbial mats such as *Leptolyngbya* that liberate gas through photosynthesis (Hinman and Lindstrom, 1996). At El Tatio, pisolites can be several centimeters in diameter, located around high-temperature facies (Jones and Renaut, 1997).

High-temperature facies (65-86°C)

Paleosinter mounds were found at several locations, with subcircular shapes and recognizable vent throats (Fig. 8A; Fig. 11). The upper portion of the vents commonly consists of geyserite texture. The lower portions of the mounds contain variably compacted silica laminae, in agreement with previous descriptions of textures in geyser mounds (Campbell et al., 2018). In mounds 429 and 404 geyserite texture was preserved at the upper portions of the geyser (Fig. 18, Appendix A), consisting of spicular geyserite. However, in mounds 408 and 502 geyserite texture was found in the middle and lower portions of the vent mostly conformed of columnar geyserite.

3.5.2 Sinter microtextures, mineralogy, and radiocarbon ages

The optical inspection of thin sections shows that sinter samples are composed of white, and light brown laminations (<0.1 mm to ~0.25 mm) and variable porosity (see appendix B). The presence of detrital crystals of quartz, plagioclase, is common in the analyzed samples. Examination of sinter samples by scanning electron microscopy (SEM) reveals that the morphology of opal-A spheres includes well-rounded nano- and microspheres (Fig. 12). Nano-

spheres and most of the micro-spheres show a smooth surface and their individual diameter can reach 3 μm but commonly have 7 μm. Micro-spheres occur mostly coalesced forming in botryoidal clusters of 20 μm. SEM examination also reveals silicified biotic components in all samples, probably representing cyanobacteria such as *Phormiduim sp.* and *Leptolyngbya* sp. Diatom frustules (e.g., *Synedra* sp.) are also recognized in samples 420 and 502t (Fernandez-Turiel 2005; Garcia-Valles et al., 2008; Phoenix et al., 2006).

Radiocarbon and calibrated ages are reported in Table 1. They range from 21,490 years B.P. to modern (<200 years B.P.). The oldest sample (412), with 21,490 years B.P., does not have a duplicate, and sample 441 age is 20,930 years B.P., but its duplicate 10,330 years B.P. Thus, we assume that the oldest meaningful age is 15,042 (sample 432). The main mineralogical characteristics of the 21 sinter samples from El Tatio are listed in Table 2. Samples were classified as opal-A and opal-A/CT, according to their FWHM values and micro-morphologies (Lynne et al., 2007; Sanchez-Yanez et al., 2017). Representative XRD traces for selected samples are shown in Fig. 13 and Fig. 43, appendix B. Samples consist mainly of opal-A, in agreement with previous studies (Fernandez-Turiel et al., 2005; Garcia-Valles et al., 2008; Nicolau et al., 2014). Opal-A/CT was recognized in samples 404e, and f, 502b, 435, and 453. Opal-C was not recognized nor previously reported. The XRD patterns show halite (NaCl) as a common accessory mineral (Fig. 43, appendix B). In addition, samples in 429 mound show presence of cristobalite and tridymite. FWHM values range from 6.75°2Θ to 9.2°2Θ (Fig. 13; Table 2), in agreement with Garcia-Valles (2008) (5.7 and 10.6 Δ°2Θ), independent of fabric type, being similar among all samples.

3.6 DISCUSSIONS

3.6.1 Mechanisms of geyser mound formation

The spatial patterns of silica precipitation and the facies that develop in sinter-forming settings are complex and are controlled by interactions among many physical, chemical, and biological factors (e.g., Braunstein and Lowe 2001; Lowe et al. 2001; Jones and Renaut 2003a). These patterns can also span several orders of magnitude, ranging from a few microns to tens of meters. Therefore, preserved stratigraphic and facies relationships can help to reconstruct how sinter mounds are formed. Textural variations have been previously reported in geyser mounds at the active Tokaanu geyser (North Island, New Zealand) by Jones and Renaut (2003b), and at the paleogeyser mound Atastra Creek (Campbell et al., 2018). In Tokaanu, several textures associated with microbes were recognized, while in Atastra Creek, intercalated geyserite with middle to low-temperature facies was described. Also, a high-temperature sinter fabric termed silica infiltrate was interpreted to represent very shallow subterranean, super-heated fluid injection processes occurring directly beneath geyser mounds and hot vent pools.

Paleosinter deposits at El Tatio presents a variety of textures similar to modern fabrics observed in active sinters. However, it is important to note that some textures may have formed at lower temperatures than estimated from comparison with geothermal fields elsewhere. Recent studies by Wostbrock et al. (2018) documenting triple oxygen isotope data of paleosinter in Puchuldiza, near El Tatio, suggest that given the strong thermal gradient at the water-air boundary, precipitation occurs at least at 10°C less than the temperature of the spring water. In mounds 404 and 429, where geyserite occurs at the top of mound and palisade at the bottom (Fig. 19, appendix A), the formation of the cone may have started by a non-surging to gently surging flux of thermal water over the pool rim. The thermal water cooled rapidly under the influence of ambient air

temperatures. In this setting, palisade texture forms under the influence of microbes, most likely over timescales of thousands of years in both mounds. In contrast, in mounds 408 and 502, geyserite texture is found at the base and the middle of the mounds, respectively. Mound 408 present 0.7 meters of geyserite, reflecting a high-temperature splash eruption between 7220 years B.P. and 555 years B.P. In mound 502 a quiescent period of activity is recorded between 2220 and 1770 years B.P. by its palisade texture. Then, a shift to a different eruptive style is evidenced by a net contact between palisade and geyserite texture (Fig. 15, appendix A). Possibly, there were pulses and pauses in the thermal water discharge, leading to an intermittent flux, as previously suggested by Foley et al. (2006) for the Castle Geyser sinter in Yellowstone National Park.

The triggering of geyser activity during the lifetime of a sinter-forming system is a highly complex process. For example, Hurwitz and Manga (2017) attribute it to external factors, including earthquakes (Jones and Renaut, 2007), faulting (Drake et al., 2014), volcanic eruptions, and seasonal climate variations. Furthermore, continuous data from >4,000 eruptions over a shorter time interval of ~1 week from a geyser the El Tatio geyser field in Chile show no sensitivity to air temperature, wind, barometric pressure, and solid Earth tides (Munoz-Saez et al. 2015a). Although springs and geysers experience cycles through periods of activity and dormancy, little is known about the factors that control those changes (Jones and Renaut, 2012). Therefore, these factors that controlled the inception of geyser activity at El Tatio remain poorly understood and should be investigated in future studies.

3.6.2 Controls on silica sinter maturation

In general, the degree of crystallinity of sinters increases with increasing age. This trend is commonly monitored using the FWHM parameter, whose values decrease from 7 to 2.5°2Θ during the transition of opal-A to opal-A/CT. Some of the world's highest FWHM values have been reported for both El Tatio and Puchuldiza sinters in Chile, suggesting a higher degree of structural disorder compared to silica sinters elsewhere (Nicolau et al., 2014; Sanchez-Yanez et al., 2017). High FWHM values for amorphous opal-A in sinter have been attributed to the incorporation of cations attached to silanol bonds (Si-OH) in the silica network that may distort the crystalline setting (Iler, 1979), or incorporation of nano-minerals or mineral nano-particles within the silica matrix during the maturation (Nicolau et al., 2014). Also, Garcia-Valles (2008) observed that when the opal-A or opal-A/-CT phases occur with other minerals (halite, sylvite, realgar, sassolite, teruggite, and quartz), their FWHM values are generally higher than in the case of the single-phase opal samples. In addition, recent studies observed experimentally that the concentration of cations such as Na and Li can be adsorbed on the silica surface, affecting the aggregation rate of silica particles (Bałdyga et al., 2012). In high altitude environments, this characteristic has also been attributed to enhanced silica precipitation due to high evaporation rates and extreme temperature oscillations that are typical of the Chilean Altiplano (Nicolau et al., 2014; Sanchez-Yanez et al., 2017; Slagter et al., 2019).

Silica sinter diagenetic transformations are kinetically driven and follow a continuous pathway from opal-A through opal-CT and/or opal-C and ultimately to quartz. These changes follow the Ostwald Step rule and are accompanied by increasing particle density (2.18 to 2.36 g/cm^3), reduction of porosity (25 to 7%) and loss of water (1.84 to 0.96 wt. %) (Herdianita et al., 2000; Campbell et al., 2001; Lynne et al., 2005), as well as morphological changes. Opal-CT is a paracrystalline structure according to Wilson (2014), containing a small volume of crystalline stacking of trydimitc nature. In addition, opal-CT sometimes also forms lepispheres and complex three-dimensional spindle frameworks (Jones and Renaut, 2007). At the microscale, opal-CT has

been reported to forms <1μm lepispheres that are composed of arrays of loosely packed intersecting thin plates of hexagonal shapes or clusters of tightly packed plates. The transition from opal-CT to opal-C involves a reorganization from blades into elongate, randomly oriented nanorods or blocky aggregates (Lynne et al., 2005).

In this study, only opal-A and opal-A/-CT were observed, without evidence of lepispheres as micromorphologies. The transition from opal-A to opal-CT most likely occurs through a dissolution–reprecipitation process (Lynne et al., 2005; Jones and Renaut, 2007). Hence, and considering that most of the samples were taken from the external walls of sinter cones (Fig. 8B), where less water was available for dissolution and reprecipitation processes, these sites are representative of an immature stage of diagenesis. Our observations in active manifestations indicate that, when formed, the sinter mounds are typically soaked with hot water following each geyser eruption. Between eruptions, the geyserite domes are exposed to the atmosphere and their surfaces undergo progressive drying unless they are continuously exposed to steam emanating from the vent. The sheltered crevices, however, may remain moist because they can retain the thermal water that drains into them following each eruption (Braunstein and Lowe 2001; Jones and Renaut, 2004). However, considering the high evaporation rates at El Tatio, and that most of the samples of this study correspond to the outermost area of geyser cones, more exposed to drying, it is likely that dissolution and reprecipitation process did not proceed efficiently to form more mature silica phases. In agreement with Munoz-Saez (2016), mound 408 (sample TAT005 in their study) has no extensive evidence of dissolution, burial, compaction or diagenesis.

One aspect that needs to be taken into account is that different portions of a sinter may undergo diagenetic transformations at different rates and at different times, according to models proposed for Te Kopia, Umukuri, Tahunaatara, Otamakokore, and Whenuaroa, and Geyser Valley (Campbell et al., 2001; Lynne et al., 2005; Drake et al., 2014; Watts-Henwood et al., 2017). This reflects changes, for example, in local water flow and environmental temperature conditions. As Jones and Renaut (2007) pointed out, the transition between opal-A to opal-CT is mediated by thermal water infiltration. Previous studies have reported that the opal-A to quartz transition in sinters ranges from ~1,900 to ~40,000 years (Herdianita et al., 2000; Lynne et al., 2005), and that opal-A can persist up to 10,000 years (Rodgers et al., 2004). At Taupo Volcanic Zone in New Zealand, microcrystalline quartz becomes a common phase in silica sinters older than ~20,000 years (Herdianita et al., 2000). For example, Martin et al. (1999) noted that 3,500 years old sinter from Te Kopia, which is predominantly opal-A, converted to opal-CT in places where it has been heated by adjacent fumaroles.

Post-depositional conditions affect diagenetic rates by either accelerating (Lynne et al., 2006) or inhibiting maturation progress (Lynne et al., 2007). Incorporation of other elements, excess organic matter, and/or postdepositional alteration by heating from nearby fumaroles or weathering can accelerate the maturation process (Herdianita et al. 2000; Lynne and Campbell, 2003). At Sinter Island, for instance, sinter achieved mineralogic maturity (quartz) within only 450 years. As dissolution features are common in Sinter Island samples (Campbell and Lynne, 2006), it is likely that overprinting by acidic steam condensate accelerated diagenesis. Formation of quartzose sinter at Opal Mound (1900 years old) was hastened by local injection of thermal fluids into the sinter (Lynne et al., 2005). According to Rodgers et al., (2004) the presence of organic carbon inhibits the successful transformation to opal-CT, explaining the persistence of opal-A at the Pleistocene Omapere silica sinter, in New Zealand. Smith et al. (2003) studied the aging in silica deposits of at the discharge drain of the Wairakei power plant, showing that after two years, samples still consist of opal-A.

In high-altitude settings such as Puchuldiza, on the other hand, the opal-A to opal-C transition has been recognized, although the age of the samples is unknown (Sanchez-Yanez et al., 2017). Figure 14 shows the FWHM parameter plotted against the radiocarbon age of the sinter samples. Also, silica sinter data with radiocarbon ages from New Zealand and the US are plotted as a reference. In this figure, it is evident that opal-A is the dominant silica phase at El Tatio, and that samples have a high degree of structural disorder with FWHM values are among the highest reported (6.2-$9.5°2\Theta$). Samples from mounds 404 and 502 show apparent trends for FHWM in reaching a difference of $2°2\Theta$ between the bottom and the top (Table 2), varying from opal-A to opal-A/CT. Our results show that opal-A is present in most of the samples younger than 8550 years B.P. Certainly, the FWHM changes observed in the present study are consistent with the pattern of behavior found by Herdianita et al. (2000), Smith et al., (2003) and Lynne et al., (2007), who reported an overall decrease in FWHM with time. However, we report in this study a different time lapse to for its changes. Micro Raman analysis showed the absence of moganite and quartz (scattering band ant 499-505 cm^{-1}) in all samples studied, corresponding to opal-A or opal-A/CT (Fig 13E), in agreement with an overall low maturity in El Tatio samples. The colored dots indicate that Steamboat Spring, Opal Mound, and Sinter Island has values between $1.5°2\Theta$ and $5.5°2\Theta$. The minor diagenetic maturation of silica sinter has also been observed in other geothermal fields such as Geyser Valley, Wairakei, New Zealand, where only opal-A a minor amount of opal-A/CT has been found (Watts-Henwood et al., 2017). The proposed explanation points to a somewhat restricted action of steam upon sinter maturation; these effects are believed to diffuse and local, only affecting some samples. No apparent correlations could be drawn between steam conditions at Geyser Valley sample locations and the state of sinter diagenesis. Similar to the sinter at Geyser Valley, Drake et al. (2014) investigated the Mangatete fossil sinter in New Zealand (up to 36 ky B.P.), and demonstrated that it preserves dominant amorphous opal-A despite evidence for local exposure to acidic steam conditions (dissolution features, localized fossil fumaroles). Thus, in agreement with these studies, it is likely that sinter diagenesis at El Tatio is not exclusively time-dependent, and silica hence phase maturation does not adhere strictly to temporal trends (e.g. as suggested by Herdianita et al., 2000). In contrast, the data presented suggest that sinter maturation at El Tatio is more likely influenced by the characteristics of the deposits (density, porosity, etc.), and the local environmental and hydrodynamic conditions.

3.7 CONCLUSIONS

The well-preserved textures at El Tatio record the geomorphic expression of ancient vent mounds and hot spring terraces formed in the last 15,042 years B.P. Sedimentary facies represent former conditions of thermal water outflow that originated the formation of textures such as palisade, laminated, plant-rich, and geyserite, reflecting fluctuations in hot spring discharge. Detailed stratigraphic and facies mapping at silica sinters from El Tatio, coupled with radiocarbon dating, revealed that different eruptive styles in paleogeyser mounds shaped these dynamic structures in a timescale of thousands of years.

Mineralogical maturation constrained with ages contributes to the understanding of diagenetic effects in silica sinter trough time. Combined SEM, XRD and radiocarbon data show that at El Tatio, diagenetic maturation through time is very subtle on geyser mounds, and is clearly site-specific. The oldest ages reported display a low stage of maturation, represented by opal-A and opal-A/-CT. This low stage of maturation is probably the result of a combination of factors

including a high concentration of cations in the sinter structure, and high evaporation, with limited dissolution-reprecipitation processes.

Overall, the excellent preservation of a suite of microbial and microfossils at El Tatio sinters may present the opportunity to further study the silicification and preservation of biosignatures. This study provides antecedents for understanding the factors controlling mineralogical changes on silica surfaces on Earth and may have astrobiological implications in the search for potential fossil life on Mars.

3.8 ACKNOWLEDGMENTS

3.9 REFERENCES CITED

Bałdyga J., Jasinska M., Jodko K., Petelski P., 2012. Precipitation of amorphous colloidal silica from aqueous solutions—Aggregation problem. Chemical Engineering Science, v. p. 77, 207-216.

Braunstein D.G., and Lowe, D.R., 2001. Relationship between spring and geyser activity and the deposition and morphology of high temperature (>73°C) siliceous sinter, Yellowstone National Park, Wyoming, U.S.A. J. of Sediment. Res. v. 71, p. 747–763.

Cady, S.L., Farmer, J.D., 1996. Fossilization Processes in Siliceous Thermal Springs: Trends in Preservation along Thermal Gradients. In: Bock, G.R., Goode, G.A. (Eds.), p. 150–173.

Campbell, K.A., Sannazzaro, K., Rodgers, K.A., Herdianita, N.R., Browne, P.R.L., 2001. Sedimentary facies and mineralogy of the late Pleistocene Umukuri silica sinter, Taupo volcanic zone, New Zealand. J. Sediment. Res. v.71, p. 727–746.

Campbell, K.A., Lynne, B.Y., 2006. Diagenesis and dissolution at Sinter Island (453 years B.P.), Taupo Volcanic Zone: Silica stars and the birth ofquartz. Proceedings of the 28th New Zealand Geothermal Workshop, Auckland, New Zealand.

Campbell, K.A., Guido, D.M., Gautret, P., Foucher, F., Ramboz, C., Westall, F., 2015a. Geyserite in hot-spring siliceous sinter: window on earth's hottest terrestrial (paleo) environment and its extreme life. Earth-Sci. Rev. v. 148, p. 44–64.

Campbell, K.A., Lynne, B.Y., Handley, K.M., Jordan, S., Farmer, J.D., Guido, D.M., Foucher, F., Turner, S., Perry, R.S., 2015b. Tracing biosignature preservation of geothermally silicified microbial textures into the geological record. Astrobiology, v.15 (10), p. 858–882.

Campbell, K.A., Guido, D.M., John, D.A., Vikre, P.G., Rhys, D., Hamilton, A., 2018. The Miocene Atastra Creek sinter (Bodie Hills volcanic field, California and Nevada): 4D evolution of a geomorphically intact siliceous hot spring deposit. J. Volc. Geoth Research, v. 370, p. 65-81.

Day, R., Jones, B., 2008. Variations in water content in opal-A and opal-CT from geyser discharge aprons. Journal of Sedimentary Research. v. 78, p. 301-315.

Dixit, C., Bernard, M.L., Sanjuan, B., André, L., Gaspard, S., 2016. Experimental study on the kinetics of silica polymerization during cooling of the Bouillante geothermal fluid (Guadeloupe, French West Indies), Chemical Geology, v. 442, p. 97-112.

Djokic, T. Van Kranendonk, M. J., Campbell, K.A., Walter, M. R., Ward, C. R., 2017. Earliest signs of life on land preserved in ca. 3.5 Ga hot spring deposits. Nature comms., v. 8, p. 1-8.

Drake, B.D., Campbell, K.A., Rowland, J.V., Guido, D.M., Browne, P.R.L., Rae, A., 2014. Evolution of a dynamic paleo-hydrothermal system at Mangatete, Taupo Volcanic Zone, New Zealand. J. Volcanol. Geotherm. Res., v. 282, p. 19–35.

Farmer, J.D., 2000. Hydrothermal systems: doorways to early biosphere evolution. GSA Today 10, p. 1–9.

Fernandez-Turiel, J.L., Garcia-Valles, M., Gimeno-Torrente, D., Saavedra-Alonso, J., Martinez-Manent, S., 2005. The hot spring and geyser sinters of el Tatio, northern Chile. Sediment. Geol., v. 180, p. 125–147.

Foley, D., 2006, Dating castle geyser: preliminary results and broad speculations on the geologic development of geysers and hydrothermal systems in Yellowstone national park, Wyoming: USA. Transaction of Geothermal Resources Council, v. 30 (I), p. 413–417.

Fournier, R., Rowe, J., 1966. Estimation of underground temperatures from the silica content of water from hot springs and steam wells. Am. J. Sci., v. 264, p. 685-697.

Fox-Powell, M. G., Channing, A., Applin, D., Mann, P. Cloutis, E. Preston, L. J. Cousins, C. R., 2018. Cryogenic silicification of microorganism in hydrothermal fluids. Earth and Planetary Science Letters, v. 498, p. 1–8.

Garcia-Valles, M., Fernandez-Turiel, J.L., Gimeno-Torrente, D., Saavedra-Alonso, J., Martinez-Manet, S., 2008. Mineralogical characterization of silica sinters from the el Tatio geothermal field, Chile. Am. Mineral., v. 93, p. 1373–1383.

Giggenbach, W.F., 1978. The isotopic composition of waters from the el Tatio geothermal field, northern Chile. Geochim. Cosmochim. Acta 42, p. 979–988.

Glennon, J.A., Pfaff, R.M., 2003. The extraordinary thermal activity of el Tatio geyser field, Antofagasta region, Chile. GOSA Trans., v. 8, p. 31–78.

Guidry, S.A., Chafetz, H.S., 2003. Anatomy of siliceous hot springs: examples from Yellowstone national park, Wyoming, USA. Sediment. Geol. v. 157, p. 71-106.

Hamilton, A., Campbell, K., Rowland, J., Browne, P., 2017. The Kohuamuri siliceous sinter as a vector for epithermal mineralisation, Coromandel Volcanic Zone, New Zealand. Miner. Deposita, v., 52, p. 181-196.

Handley, K.M., Campbell, K.A., Mountain, B.W., Browne, P.R.L., 2005. Abiotic–biotic controls on the origin and development of spicular sinter: in situ growth experiments, champagne pool, Waiotapu, New Zealand. Geobiology 3, 93–114.

Heaney, P.J., Post, J.E., 1992. The widespread distribution of a novel silica polymorph in microcrystalline quartz varieties. Science 255, 441–443.

Herdianita, N.R., Browne, P.R.L., Rodgers, K.A., Campbell, K.A., 2000. Mineralogical and textural changes accompanying ageing of silica sinter. Mineral. Deposita 35, 48–62.

Hinman, N.W., Lindstrom, R.F., 1996. Seasonal changes in silica deposition in hot spring systems. Chem. Geol. 132, 237–246.

Hogg, A., Hua, Q., Blackwell, P.G., Niu, M., Buck, C.E., Guilderson, T.P., Heaton, T.J., Palmer, J.G., Reimer, P.J., Reimer, R.W., Turney, C.S.M., Zimmerman, S.R.H., 2013, SHCal13 Southern Hemisphere calibration, 0–50,000 years cal BP: Radiocarbon, v. 55, p. 1889–1903.

Hurwitz, S., Manga, M., 2017. The fascinating and complex dynamics of geyser eruptions. Annu. Rev. Earth Planet. Sci., v. 45, p. 31–59.

Iler, R.K., 1979. The chemistry of silica: solubility, polymerization, colloid and surface properties and biochemistry. Wiley, New York (866 pp.).

Jones, B., Renaut, R.W., 1997. Formation of silica oncoids around geysers and hot springs at El Tatio, northern Chile. Sedimentology, v. 44, p. 287–304.

Jones, B., Renaut, R.W., 2003a. Hot spring and geyser sinters: the integrated product of precipitation, replacement and deposition. Can. J. Earth Sci., v. 40, p. 1549–1569.

Jones, B., Renaut, R.W., Rosen, M.R., 2003b. Silicified Microbes in a Geyser Mound: The Enigma of Low-Temperature Cyanobacteria in a High-Temperature Setting. Palaios. 18: 87–109.

Jones, B., Renaut, R. W., 2004. Water content of opal-A: implications for the origin of laminae in Geyserite and sinter. J. Sediment. Res. 74, 117–128.

Jones, B., Renaut, R.W., 2007. Microstructural changes accompanying the opal-A to opal-CT transition: new evidence from the siliceous sinters of Geysir, Haukadalur, Iceland. Sedimentology, v. 54, p. 921–948.

Jones, B., Renaut, R.W., 2012 Facies architecture in depositional systems resulting from the interaction of acidic springs, alkaline springs, and acidic lakes: case study of Lake Roto-a-Tamaheke, Rotorua, New Zealand. Can. J. Earth Sci., v. 49, p. 1217–1250.

Konhauser, K.O., Phoenix, V.R., Bottrell, S.H., Adams, D.G., Head, I.M., 2001. Microbial–silica interactions in Icelandic hot spring sinter: possible analogues for some Precambrian siliceous stromatolites: Sedimentology, v., 48, p. 415–433.

Konhauser, K. O., Jones, B., Reysenbach, A.-L., & Renaut, R. W., 2003. Hot spring sinters: Keys to understanding Earth's earliest life forms. Canadian Journal of Earth Sciences, 40(11), p. 1713–1724.

Laetsch, T. and Downs, T., 2006. Software for identification and refinement of cell parameters from powder diffraction data of minerals using the RRUFF project and American Mineralogist Crystal Structure databases. 19th General Meeting of the International Mineralogical Association, Kobe, Japan, 23, p.28.

Lahsen, A., Trujillo, P., 1975. El Tatio geothermal field. Proc. of the Second United Nations Symposium on the Development and Use of Geothermal Resources, San Francisco, California, pp. 157–178.

Lahsen, A., 1976. Geothermal exploration in Northern Chile-Summary. Circum Pacific Energy and Mineral Resour. Conf., Honolulu, pp. 169–175.

Landrum, J.T., Bennett, P.C., Engel, A.S., Alsina, M.A., Pasten, P.A., Milliken, K., 2009. Partitioning geochemistry of arsenic and antimony, El Tatio geyser field, Chile. Appl. Geochem., v. 24, p. 664-676.

Liesegang, M.; Milke, R.; Berthold, C., 2018. Amorphous silica maturation in chemically weathered clastic sediments. Sediment. Geol. 365, 54–61.

Lowe, D.R., Braunstein, D., 2003. Microstructure of high-temperature (>73 °C) siliceous sinter deposited around hot springs and geysers, Yellowstone National Park: the role of biological and abiological processes in sedimentation. Canadian Journal of Earth Sciences v. 40, p. 1611–1642.

Lowenstern, J. B., Hurwitz, S., McGeehin J.P., 2016, Radiocarbon dating of silica sinter deposits in shallow drill cores from the Upper Geyser Basin, Yellowstone National Park: Journal of Volcanology and Geothermal Research, v. 310, p. 132-136.

Lynne, B.Y., Campbell, K.A., 2003. Diagenetic transformations (opal-A to quartz) of low and mid-temperature microbial textures in siliceous hot-spring deposits, Taupo Volcanic Zone, New Zealand. Can. J. Earth Sci. v. 40, p. 1679–1696.

Lynne, B.Y., Campbell, K.A., 2004. Morphologic and mineralogic transitions from opal-A to opal-CT in low-temperature siliceous sinter diagenesis, Taupo Volcanic Zone, New Zealand. J. Sediment. Res. v. 74, p. 561–579.

Lynne, B.Y., Campbell, K.A., Moore, J.N., Browne, P.R.L., 2005. Diagenesis of 1900-year-old siliceous sinter (opal-A to quartz) at Opal Mound, Roosevelt Hot Springs, Utah, U.S.A.Sediment. Geol. v. 179, p. 249–278.

Lynne, B.Y., Campbell, K.A., Perry, R.S., Browne, P.R.L., Moore, J.N., 2006. Acceleration of sinter diagenesis in an active fumarole Taupo Volcanic Zone, New Zealand. Geology, v. 34, p. 749–752.

Lynne, B.Y., Campbell, K.A., James, B., Browne, P.R.L., Moore, J.N., 2007. Tracking Crystallinity in Siliceous Hot-Spring Deposits. Am. J. Sci., v. 307, p. 612–641.

Lynne, B.Y., Campbell, K.A., Moore, J.N., Browne, P.R.L., 2008. Origin and evolution of the Steamboat Springs siliceous sinter deposit, Nevada, U.S.A. Sediment. Geol., v. 210, p. 111–131.

Lynne, B.Y., 2012. Mapping vent to distal-apron hot spring paleo-flow pathways using siliceous sinter architecture. Geothermics v. 43, p. 3–24.

Martin, R., Mildenhall, D., Browne, P.R.L., Rodgers, K.A., 2000. The age and significance of in-situ sinter at Te Kopia thermal area. Geothermics v. 29, p. 367–375.

Morris, R. V., Vaniman, D. T., Blake, D. F., Gellert, R., Chipera, S. J., Rampe, E. B., 2016. Silicic volcanism on Mars evidenced by tridymite in high-SiO_2 sedimentary rock at Gale crater. PNAS, 113(26), 7071–7076.

Mountain B. W., Benning L. G. and Boerema J. A., 2003. Experimental studies on New Zealand hot spring sinters: rates of growth and textural development. Can. J. Earth Sci. v. 40, p. 1643–1667.

Munoz-Saez, C., Manga, M., Hurwitz, S., Rudolph, M., Namiki, A., Wang, C.-Y., 2015a. Dynamics within geyser conduits, and sensitivity to environmental perturbations: insights from a periodic geyser in the El Tatio geyser field, Atacama Desert, Chile. J. Volcanol. Geotherm. Res., v. 292, p. 41–55.

Munoz-Saez, C., Saltiel, S., Manga, M., Nguyen, C., Gonnermann, H., 2016, Physical and hydraulic properties of modern sinter deposits: El Tatio, Atacama: Journal of Volcanology and Geothermal Research, v. 325, p. 156-168.

Munoz-Saez, C., Manga, M., Hurwitz, S., 2018, Hydrothermal discharge from the El Tatio basin, Atacama, Chile: Journal of Volcanology and Geothermal Research, v. 325, p. 25-35.

Nicolau, C., Reich, M., Lynne, B., 2014, Physico-chemical and environmental controls on siliceous sinter formation at the high-altitude El Tatio geothermal field, Chile: Journal of Volcanology and Geothermal Resources, v. 282, p. 60–76.

Phoenix, V.R., Bennett, P.C., Engel, A.S., Tyler, S.W., Ferris, F.G., 2006. Chilean high-altitude hot- spring sinters: a model system for UV screening mechanisms by early Precambrian cyanobacteria. Geobiology, v. 4, p. 15–28.

Rodgers, K.A.; Cressey, G., 2001. The occurrence, detection, and significance of moganite (SiO_2) among some silica sinters. Mineral. Mag. v. 65, p. 157–167.

Rodgers, K.A., Greatrex, R., Hyland, M., Simmons, S.F., Browne, P.R.L., 2002. A modern, evaporitic occurrence of teruggite, $Ca_4MgB_{12}As_2O_{28} \cdot 18H_2O$, and nobleite, $CaB_6O_{10} \cdot 4H_2O$, from the El Tatio geothermal field, Antofagasta Province, Chile. Mineral. Mag. v. 66, p.253–259.

Rodgers, K.A.; Hampton, W.A., 2003. Laser Raman identification of silica phases comprising microtextural components of sinters. Mineral. Mag. v. 67, p. 1–13.

Rodgers, K.A.; Browne, P.R.L.; Buddle, T.F.; Cook, K.L.; Greatrex, R.A.; Hampton, W.A.; Herdianita, N.R.; Holland, G.R.; Lynne, B.Y.; Martin, R., 2004. Silica phases in sinters and residues from geothermal fields of New Zealand. Earth Sci. Rev. v. 66, p. 1–61.

Ruff, S.W., Farmer J. D., 2016. Silica deposits on Mars with features resembling hot spring biosignatures at El Tatio in Chile. Nature communications 7, 13554.

Sanchez-Yañez, C., Reich, M., Leisen, M., Morata, D., Barra, F., 2017, Geochemistry of metals and metalloids in siliceous sinter deposits: Implications for elemental partitioning into silica phases: Applied Geochemistry, v. 80, p. 112-123.

Sillitoe, R.H., 2015, Epithermal paleosurfaces: Mineralium Deposita, v. 50, I. 7, p.767-793.

Slagter, S., Reich, M., Munoz-Saez, C., Southon, J., Morata, D., Barra, F., Gong, J., Skok, J.R., 2019, Environmental controls on silica sinter formation revealed by radiocarbon dating. Geology https://doi.org/10.1130/G45859.1.

Smith, B.Y., Turner, S.J., Rodgers, K.A., 2003. Opal-A and associated microbes from Wairakei, New Zealand: the first 300 days. Mineral. Mag. v. 67, p. 563–579.

Stuiver, M., Polach, H.A., 1977, Discussion: reporting of 14C data: Radiocarbon, v. 19, p. 355–363.

Sun, V. Z., & Milliken, R. E., 2018. Distinct geologic settings of opal-A and more crystalline hydrated silica on Mars. Geophysical Research Letters, v. 45, (10) p. 221–228.

Taksavasu, T., Monecke, T., Reynolds, T. 2018. Textural characteristics of noncrystalline silica in sinters and quartz veins: implications for the formation of bonanza veins in low-sulfidation epithermal deposits. Minerals v. 8, p. 331.

Tosca, N. J., & Knoll, A. H. 2009. Juvenile chemical sediments and the long term persistence of water at the surface of Mars. Earth and Planetary Science Letters, v. 286(3–4), p. 379–386.

Walter, M.R. 1976. Hot-spring sediments in Yellowstone National Park. In Stromatolites. Edited by M.R. Walter. Developments in Sedimentology, Vol. 20, Elsevier, Amsterdam, The Netherlands, pp.489–498.

Watts-Henwood, N., Campbell, K. A., Lynne, B. Y., Guido, D. M., Rowland, J. V., Browne, P. R.L., 2017. Snapshot of hot-spring sinter at Geyser Valley, Wairakei, New Zealand, following anthropogenic drawdown of the geothermal reservoir. Geothermics, v. 68, p. 94-114.

Weed, W.H., 1889. On the formation of siliceous sinter by vegetation of thermal springs. American Journal of Science, v. 37 (217–222), p. 351–359.

White, D.E., Brannock, W.W., Murata, K.J., 1956. Silica in hot- spring waters. Geochimica et Cosmochimica Acta v. 10, p. 27–59.

White, N.C., Wood, D.G., Lee, M.C., 1989. Epithermal sinters of Paleozoic age in north Queensland, Australia. Geology. v. 17, p. 718–722.

Wilson, M.J., 2014. The structure of opal-CT revisited. Journal of Non-Crystalline Solids. v.405, p. 68–75.

Wostbrock J. A. G., Sharp, Z. D., Sanchez-Yanez, C., Reich, M., van den Heuvel, D. B., Benning, L. G., 2018. Calibration and application of silica-water triple oxygen isotope thermometry to geothermal systems in Iceland and Chile. Geochim. Cosmochim. Acta. v. 234, p. 84-97.

3.10 FIGURES
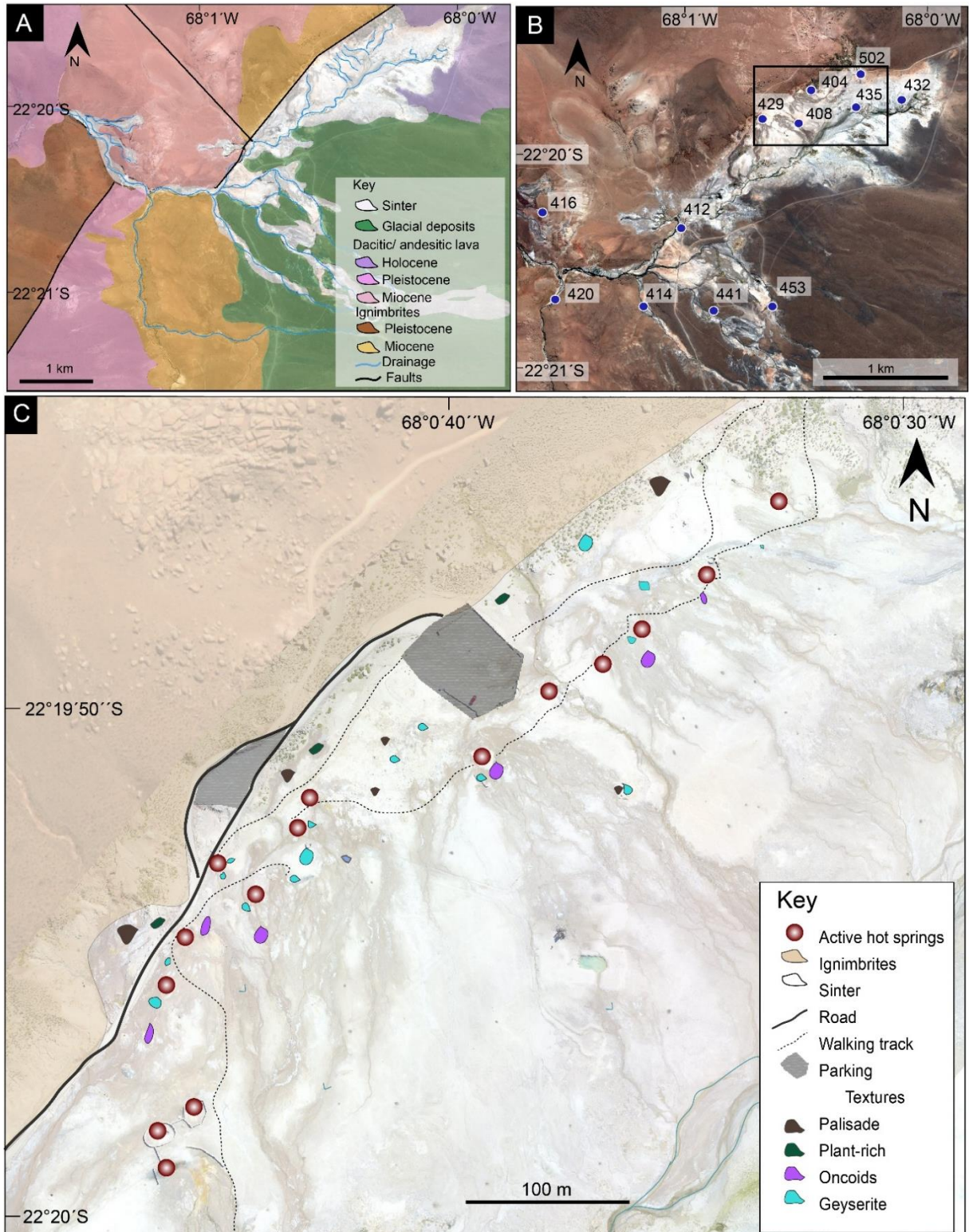
Figure 7. A. Geology of El Tatio geothermal field (modified from Muñoz-Saez et al., 2018). B. Aerial photograph showing sinter samples (blue dots labeled). C. Map of the upper basin (black rectangle in B) showing main thermal manifestations and textures. Mapping of surface thermal manifestations is overlain on a Drone image obtained in April 2017.
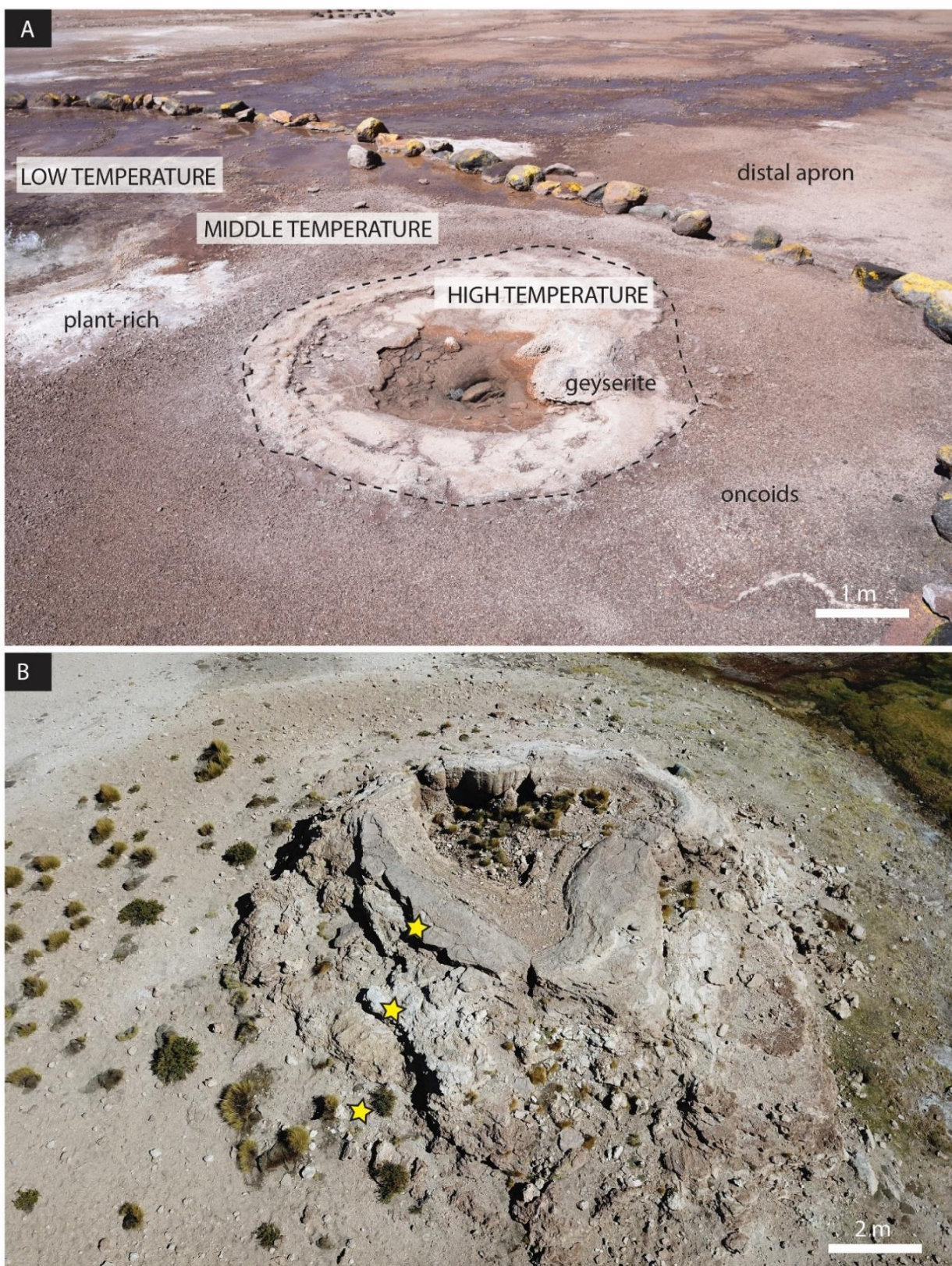
Figure 8. A. Sedimentary facies showing three environments: high, middle, and low temperature. In the high temperature setting the geyserite texture can be recognized, in the middle temperature the formation oncoids can be recognized, and in the low-temperature plant-rich fabrics are present. B. Aerial drone image of geyser mound 502 showing sampled sites in yellow stars.
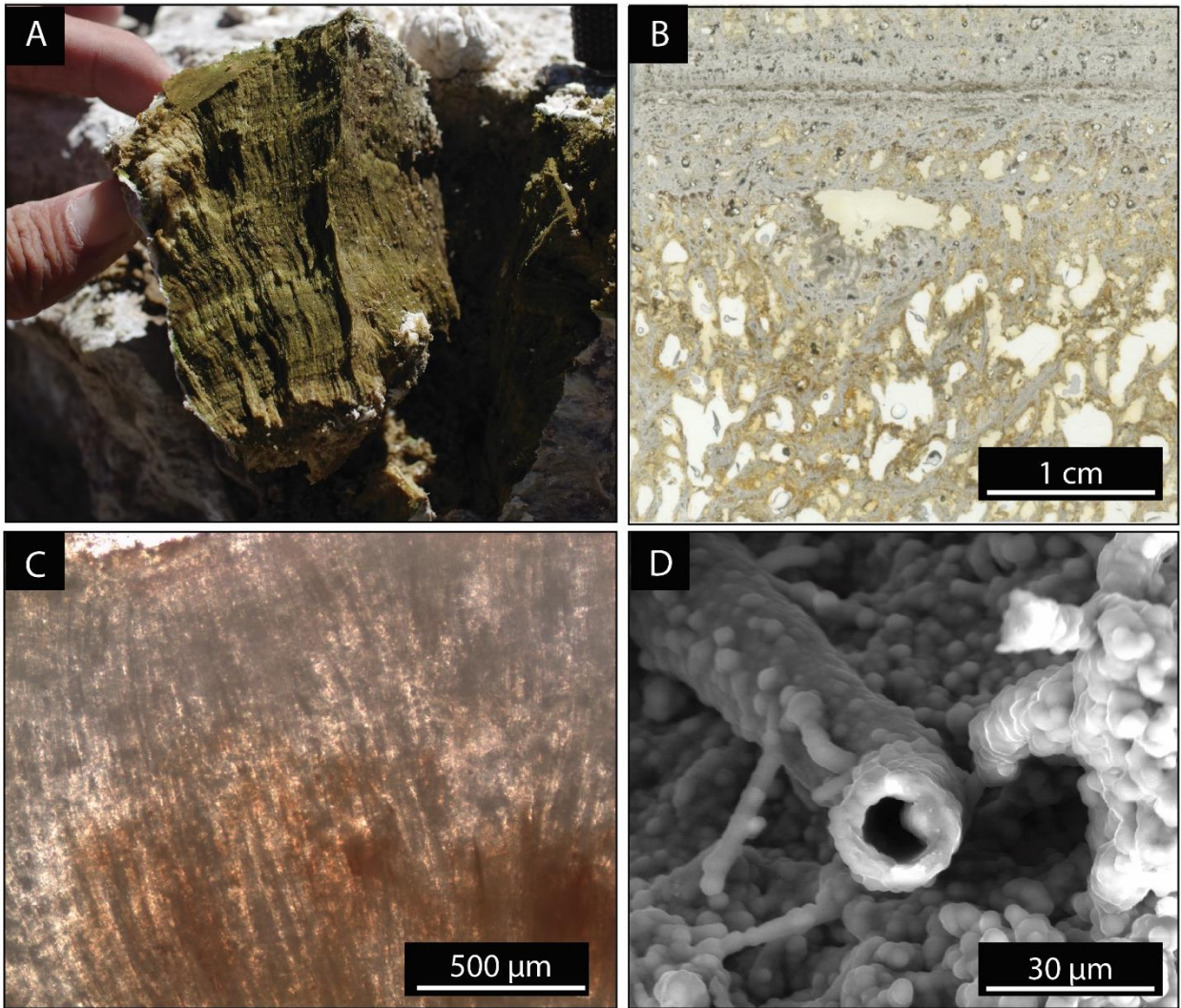
Figure 9. Photographs and photomicrographs of palisade texture. A. Hand sample with layers of five centimeters formed by bacteria filaments. B. sample 404c scanned thin section, showing two layers with porous texture in the bottom and layered texture at the top. Around porous, there are bacteria filaments. C. Photomicrograph of sample 404c thin section under transmitted light showing vertical bacteria filaments. D. Secondary electron SEM images of filament molds partially filled with porous silica present in sample 404c.
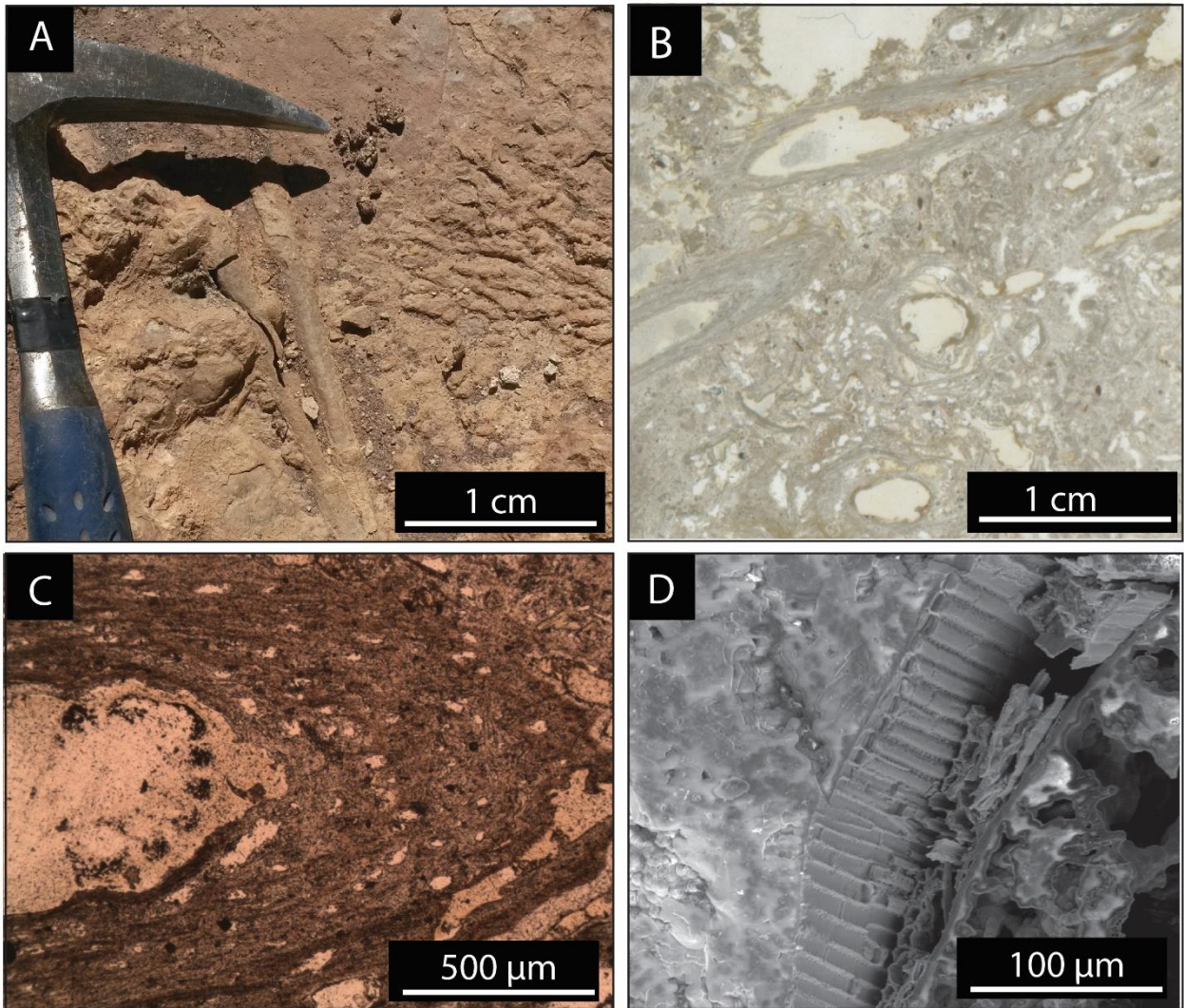
Figure 10. Photographs and photomicrographs of plant-rich texture. A. Hand sample with *in situ* fragments of plants. B. Scanned thin section of sample 429b, showing fragments of plants. C. Photomicrograph under polarized light with a cross-section of plant fragment. D. Secondary electron SEM image of a lateral view of the plant fragments.

Figure 11. Photographs and photomicrographs of geyserite texture. A. Hand sample of geyserite with columns of 10 cm high of a paleogeyser mound. B. Secondary electron SEM image of a cross view of columnar geyserite. There are gypsum crystals and detrital grains in between columns. C. Scanned thin section of sample 408b, showing convex stacking of silica pointing upward and the typical fine, dense laminae and cornices on either side of the column. Between columns, there are detrital grains.
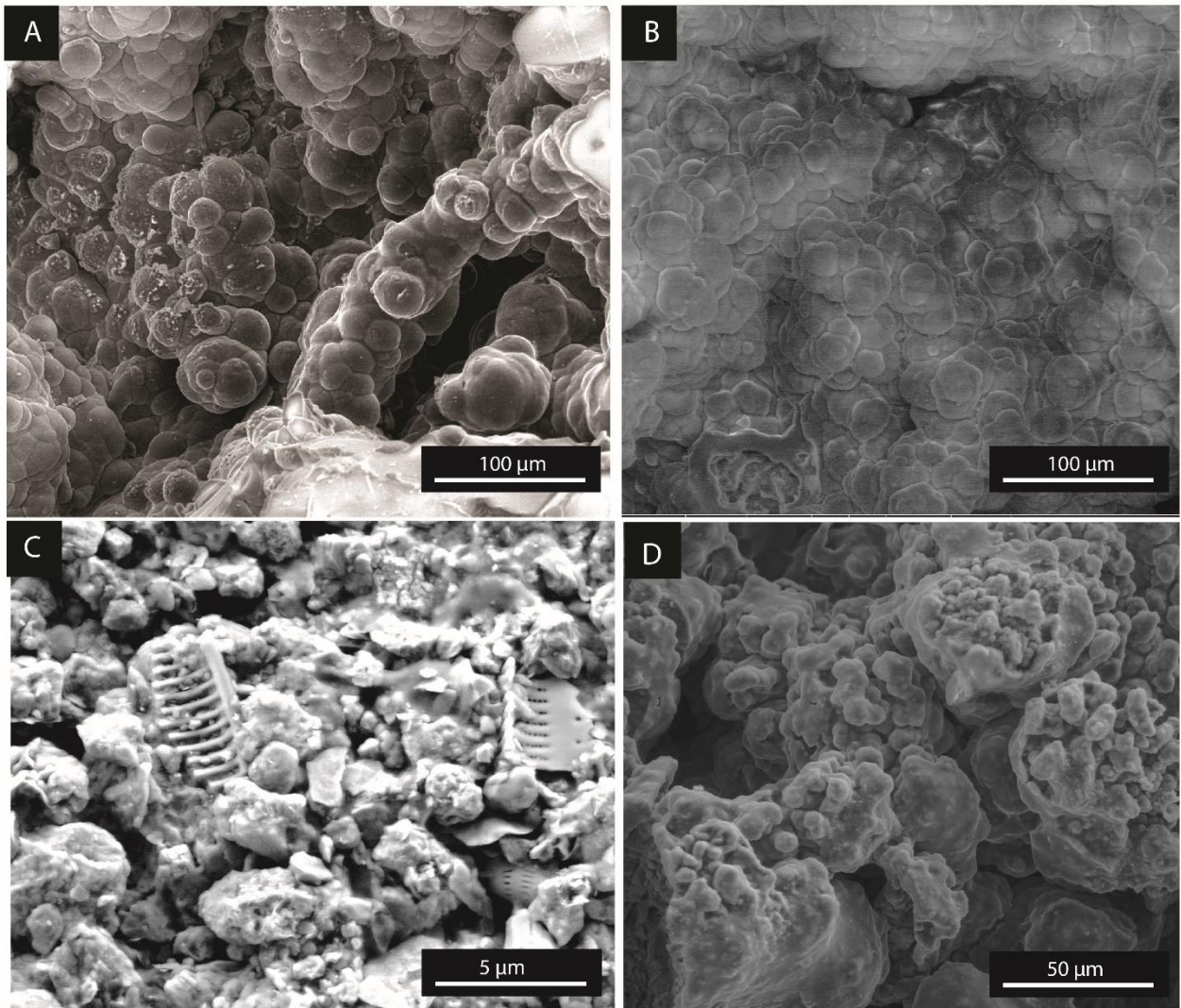
Figure 12. SEM images of silica sinter micromorphology, mainly consisting of opal-A spheres. A 404 sample showing opal-A clusters of botryoidal spheres of 20µm. B.408t sample showing spheres of opal-A up to 30µm diameter. C. FE-SEM image of sample 502 showing rests of diatoms. D. Botroyds clusters present in sample 432.
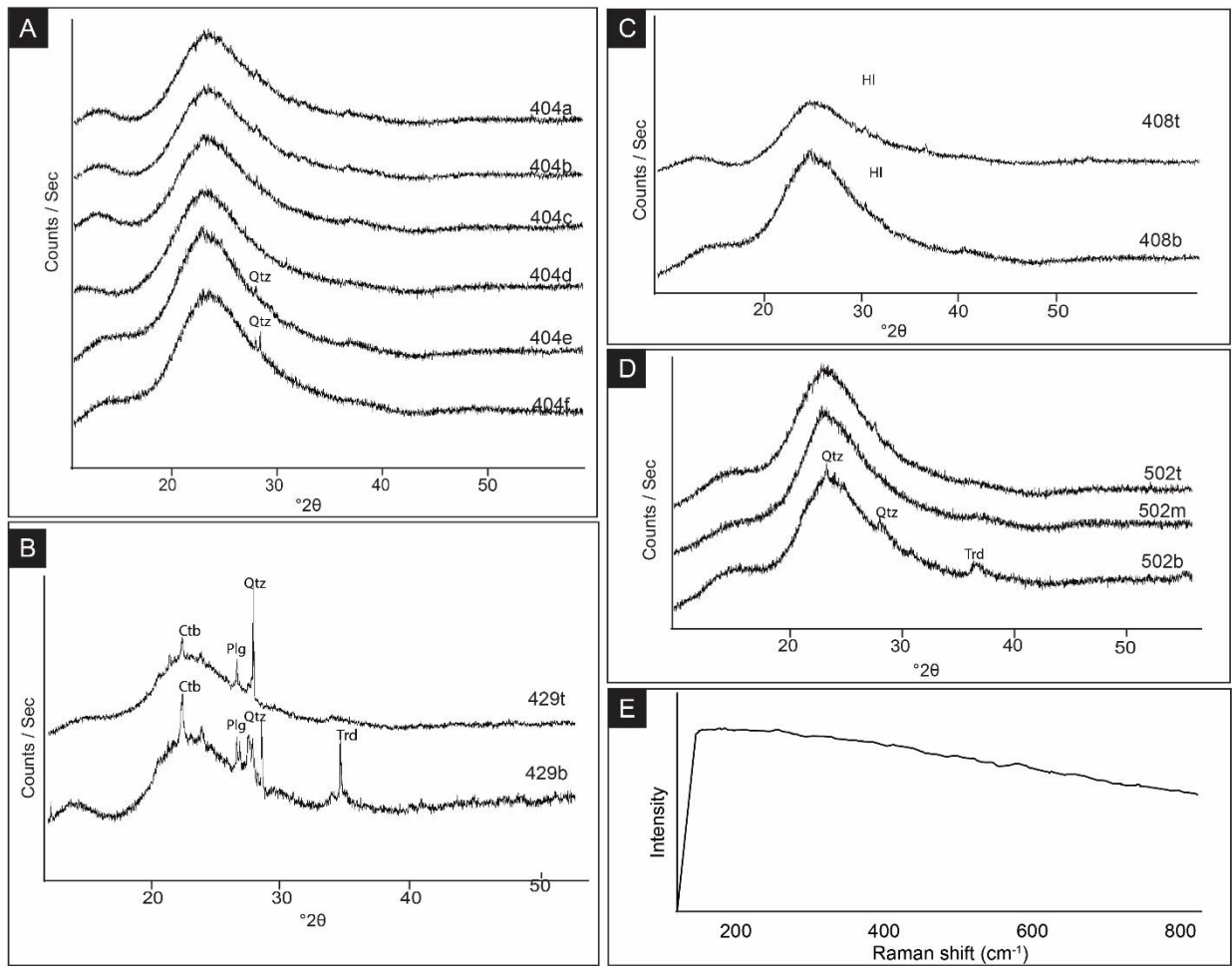
Figure 13. XRD spectra of selected sinter samples. A. 404 B. 408 C. 429 D. 502. Samples 404a,b,c,d 408b,t, 429b,t and 502b and m correspond to opal-A. The broadband is centered at 22.2°2Θ, with FWHM values between 6.9°2Θ and 9.3°2Θ. Samples 404e,f, and 502b correspond to opal-CT, and FWHM values vary between 5.7 and 6.1°2Θ. Main accessory minerals phases are labeled and correspond to plagioclase (Plg), halite (Hl), detrital quartz (Qz), tridymite (Trd) and cristobalite (Ctb). E. Raman shift of sample 502b, showing the typical opal-A spectra (Lynne et al., 2007).
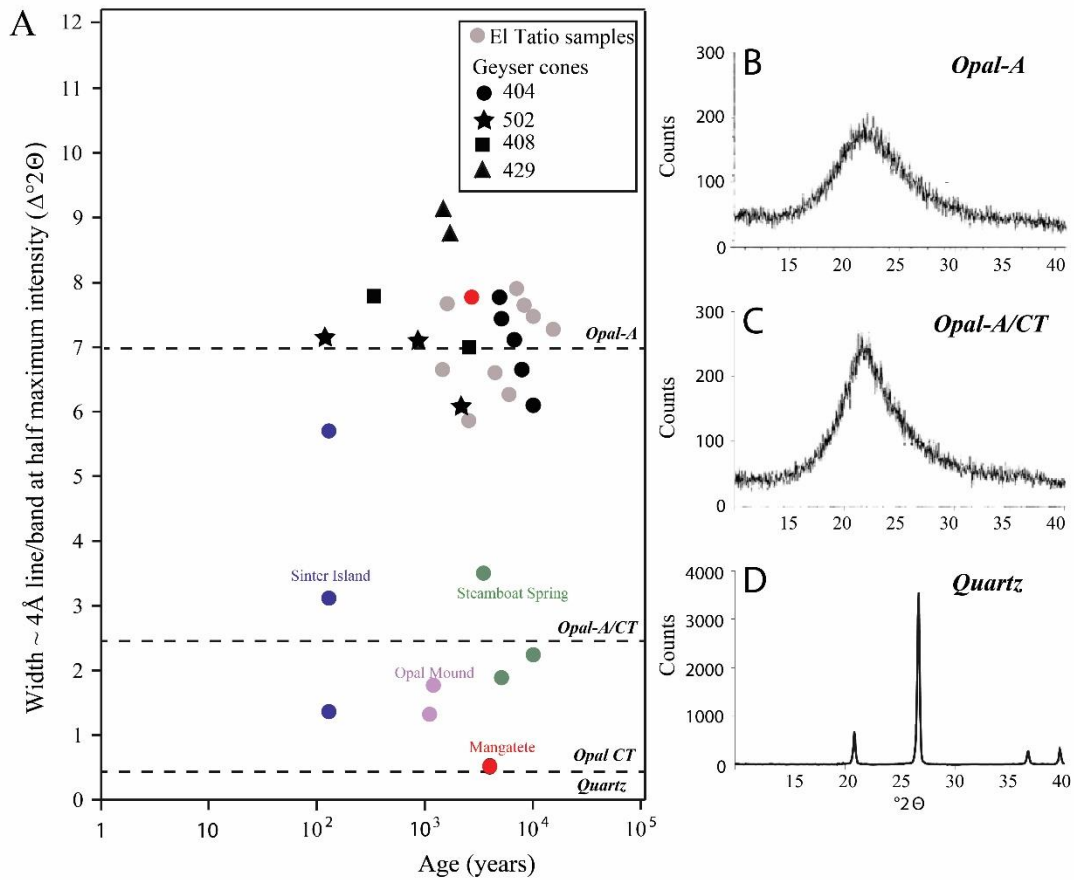
Figure 14. A. Full width at half maximum intensity of the ~4 Å line as a proxy for crystallinity versus ages of sinters from El Tatio and elsewhere (modified from Herdianita et al., 2000). El Tatio samples are indicated by grey circles, and black circles, stars, triangles, and squares. Colored circles represent geothermal fields elsewhere that have been dated with radiocarbon. B. Typical opal-A trace. C. Typical opal-A/CT trace. D. Typical quartz trace.

Table 1. Radiocarbon ages

	Sample code	Lab code	Fraction modern	±	d^{13}C (‰)	±	^{14}C age years B.P.	±	cal age * cal years B.P.		Median proability
Paleogeyser mounds	404a	198595	0.482	0.0012	-24.03	0.1	5860	25	6527	6696	6626
	404b	198596	0.454	0.0040			6330	80	6999	7340	7207
	404c	198594	0.358	0.0062			8230	140	8718	9480	9147
	404d	198611	0.344	0.0020			8550	50	9437	9548	9506
	404e	198613	0.312	0.0010			9340	30	10375	10588	10501
	404e†	198593	0.304	0.0014	-25.12	0.1	9565	40	10666	10892	10856
	404f	198612	0.259	0.0009			10840	30	12683	12744	12711
	502t	198602	0.971	0.0037			230	35	139	230	197
	502m	198601	0.806	0.0014	-20.42	0.1	1730	15	1540	1613	1585
	502m†	198618	0.799	0.0014			1805	15	1611	1673	1648
	502b	198600	0.758	0.0014	-20.51	0.1	2220	15	2221	2307	2241
	408t	198614	0.933	0.0018	-25.02	0.1	555	20	511	548	531
	408b	191794	0.407	0.0022			7220	45	7930	8065	7993
	429t	198617	0.721	0.0014	-22.41	0.1	2625	20	2700	2764	2737
	429b	191803	0.629	0.0052	-21.07	0.1	3720	70	3832	4236	4015
Surface samples	412	191779	0.069	0.0010			21490	120	25522	25986	25764
	414	191772	0.288	0.0048			10000	140	11144	11995	11489
	414†	191799	0.3092	0.0008			9430	25	10520	10699	
	416	191789	0.5819	0.0010	-21.19	0.1	4350	15	4834	4892	4862
	416†	191773	0.572	0.0016			4485	25	4954	5081	5050
	416†	191783	0.587	0.0011			4280	15	4811	4857	4831
	416†	191800	0.578	0.0011			4400	15	4854	4975	4919
	420	191784	1.0661	0.0038			Modern	-	-	-	-
	432	191801	0.163	0.0007	-19.40	0.10	14575	40	17541	17904	17713
	432†	191774	0.156	0.0006			14910	35	17907	18245	18070
	432†	191785	0.146	0.0113			15450	630	17127	20155	18661
	432†	191790	0.142	0.0007			15680	40	18764	18993	18876
	435	191775	0.212	0.0008			12470	30	14210	14850	14527
	441	191778	0.276	0.0014			10330	40	11824	12154	12033
	441†	191793	0.074	0.0007			20930	80	24946	25507	25223
	453	191802	0.744	0.0014	-23.41	0.10	2370	20	2309	2382	2346
	453†	191776	0.747	0.0021			2340	25	2303	2357	2330
	453†	191791	0.757	0.0013			2240	15	2217	2308	2233

*Using the SHCal13 dataset (Hogg et al., 2013). Calibrated ages are presented as mean ages with 2 sigma (95%) confidence limits

†Duplicate (gray)

Table 2. Mineralogy and XRD parameters for the El Tatio sinter samples

	Sample	Texture	Lab code	^{14}C age years B.P.	±	FWHM	Mineral Phase
Paleogeyser mounds	404a	Geyserite	198595	5860	25	7.7	opal-A
	404b	Palisade	198596	6330	80	7.5	opal-A
	404c	Palisade	198594	8230	140	7.5	opal-A
	404d	Palisade	198611	8550	50	7.4	opal-A
	404e	Laminated	198613	9340	30	6.0	opal-A/CT
	404f	Laminated	198612	10840	30	5.7	opal-A/CT
	502t	Palisade	198602	230	35	7.2	opal-A
	502m	Geyserite	198601	1730	15	7.0	opal-A
	502b	Laminated	198600	2220	15	6.1	opal-A/CT
	408t	Palisade	198614	555	20	7.5	opal-A
	408b	Geyserite	191794	7220	45	7.0	opal-A
	429t	Geyserite	198617	2625	20	9.3	opal-A
	429b	Palisade	191803	3720	70	9.0	opal-A
Surface samples	412	Palisade	191779	21490	120	7.2	opal-A
	414	Palisade	191799	9430	25	9.0	opal-A
	416	Plant-rich	191789	4350	15	7.2	opal-A
	420	Plant-rich	191784	Modern		7.8	opal-A
	432	Palisade	191790	15680	40	8.8	opal-A
	435	Laminated	191775	12470	30	6.2	opal-A/CT
	441	Palisade	191778	10330	40	8.2	opal-A
	453	Laminated	191776	2340	25	5.4	opal-A/CT

46

CHAPTER 4: CONCLUSIONS

In this study, stratigraphically controlled radiocarbon (^{14}C) ages of silica sinter deposits from the El Tatio geyser field in northern Chile are presented. The ^{14}C ages were obtained in the organic matter trapped within silica sinter, and indicate that the El Tatio geothermal system has been active for at least 15,000 years B.P.

The radiocarbon ages were integrated with a morphological and textural characterization of the stratigraphic profiles to determine silica precipitation rates. The radiocarbon-based estimations are consistent with *in situ* silica precipitation experiments undertaken at El Tatio, and vary from 0.1 to 3.5 kg/year/m^2. These rates are higher than the silica formation rates reported in previous studies at Geysir, Iceland, Champagne Pool, in New Zealand and Buffalo Pool in Yellowstone National Park, U.S.A (0.1 to 1.5 kg/year/m^2). These differences are attributed here to environmental effects on silica precipitation, which for the case of El Tatio are intrinsically linked to its geographic location at more than 4200 meters above sea level in the Chilean Altiplano. The high-altitude climatic conditions induce increased silica precipitation at the surface, as a result of high evaporation rates and extreme thermal variations during the day-night cycle.

Radiocarbon data allowed contrasting silica precipitation rates as a function of sinter age. Results show secular variations in the silica precipitation rate, with an increment from 0.5 to 2.57 kg/year/m^2 in the last 2000 years. Although the cause of such variations needs to be further investigated, it is likely that changes in the silica precipitation rate may be a response to intrinsic variations of the geothermal system or changes in the climatic conditions.

The detailed inspection of active geyser and paleosinter mounds at El Tatio show distinctive textures revealing changes in both temperature and hydrodynamic conditions over time. The ~two-meter high structures present geyserite, palisade and laminated textures that are detected in both active and extinct mounds. The variations of silica crystallinity of the sinter samples are also evaluated as a function of sinter age. Opal-A is the dominant mineral phase in sinter mounds, regardless of their radiocarbon age. Therefore, our results contrast with the maturation model proposed by Herdianita (2000), where amorphous silica phases (opal-A) change progressively to opal-CT, opal-C and finally quartz over a scale of ten to fifty thousand years. For El Tatio, we suggest that this sinter diagenesis is mainly controlled by the position of the water table, in agreement with Jones and Renaut (2004). These are aspects that need to be investigated in further studies.

Overall, the results presented in this thesis suggest that siliceous sinter deposits may contain not only a rich mineralogical and biogeochemical archive, but also bear information crucial for reconstructing the heat advected from geothermal systems and exploring the effects of climate on silica precipitation in Earth, and potentially Mars.

BIBLIOGRAPHY

Bignall, G., Browne, P., 1994. Surface hydrothermal alteration and evolution of the Te Kopia Thermal Area, New Zealand. Geothermics, v. 23, No. 5/6, pp. 645-658.

Boudreau, A.E., Lynne, B.Y., 2012, The growth of siliceous sinter deposits around high-temperature eruptive hot springs: Journal of Volcanology and Geothermal Research, v. 247–248, p. 1–8.

Braunstein D.G., and Lowe, D.R., 2001. Relationship between spring and geyser activity and the deposition and morphology of high temperature (>73°C) siliceous sinter, Yellowstone National Park, Wyoming, U.S.A. J. of Sediment. Res. v. 71, p. 747–763.

Cady, S.L., Farmer, J.D., 1996. Fossilization Processes in Siliceous Thermal Springs: Trends in Preservation along Thermal Gradients. In: Bock, G.R., Goode, G.A. (Eds.), pp. 150–173.

Campbell, K.A., Sannazzaro, K., Rodgers, K.A., Herdianita, N.R., Browne, P.R.L., 2001. Sedimentary facies and mineralogy of the late Pleistocene Umukuri silica sinter, Taupo volcanic zone, New Zealand. J. Sediment. Res. v.71, p. 727–746.

Campbell K.A., Guido, D.M., Gautret, P., Foucher F., Ramboz C., Westall F., 2015. Geyserite in hot-spring siliceous sinter: Window on Earth's hottest terrestrial (paleo) environment and its extreme life: Earth-Science Reviews, v. 148, p. 44- 64.

Campbell, K.A., Guido, D.M., John, D.A., Vikre, P.G., Rhys, D., Hamilton, A., 2018. The Miocene Atastra Creek sinter (Bodie Hills volcanic field, California and Nevada): 4D evolution of a geomorphically intact siliceous hot spring deposit. J. Volc. Geoth Research.v. 370, p. 65-81.

Cortecci, G., Boschetti, T., Mussi, M., Lameli, C.H., Mucchino, C., Barbieri, M., 2005. New chemical and original isotopic data on waters from el Tatio geothermal field, northern Chile. Geochem. J. 39 (6), 547–571.

Cusicanqui, H., Mahon, W.A.J., Ellis, A.J., 1975. The geochemistry of the El Tatio geothermal field, Northern Chile. Second United Nations Symposium on the Development and Utilization of Geothermal Resources, San Francisco, pp. 703–711.

Dixit, C., Bernard, M.L., Sanjuan, B., André, L., Gaspard, S., 2016. Experimental study on the kinetics of silica polymerization during cooling of the Bouillante geothermal fluid (Guadeloupe, French West Indies). Chemical Geology. v. 442, p. 97-112

Drake, B.D., Campbell, K.A., Rowland, J.V., Guido, D.M., Browne, P.R.L., Rae, A., 2014. Evolution of a dynamic paleo-hydrothermal system at Mangatete, Taupo Volcanic Zone, New Zealand. J. Volcanol. Geotherm. Res. v. 282, p. 19–35.

Fernandez-Turiel, J.L., Garcia-Valles, M., Gimeno-Torrente, D., Saavedra-Alonso, J., Martinez-Manent, S., 2005. The hot spring and geyser sinters of el Tatio, northern Chile. Sediment. Geol. 180, 125–147.

Fournier, R.O., 1985. The behaviour of silica in hydrothermal solutions. Reviews in Economic Geology 2:45–62.

Fox-Powell, M. G., Channing, A., Applin, D., Mann, P. Cloutis, E. Preston, L. J. Cousins, C. R., 2018. Cryogenic silicification of microorganism in hydrothermal fluids. Earth and Planetary Science Letters v. 498, p. 1–8.

Geilert S., Vroon P. Z. and Bergen M. J. Van, 2016. Effect of diagenetic phase transformation on the silicon isotope composition of opaline sinter deposits of Geysir, Iceland. Chem. Geol. 433, 57–67.

Gibson, R.A., Sherry, A., Kaur, G., Pancost, R.D., Talbot, H.M., 2014. Bacteriohopanepolyols preserved in silica sinters from Champagne Pool (New Zealand) indicate a declining temperature gradient over the lifetime of the vent. Org. Geochem. 69, 61-69.

Giggenbach, W.F., 1978. The isotopic composition of waters from the El Tatio geothermal field, Northern Chile. Geochim. Cosmochim. Acta 42, 979–988.

Glennon, J.A., Pfaff, R.M., 2003. The extraordinary thermal activity of el Tatio geyser field, Antofagasta region, Chile. GOSA Trans. 8, 31–78.

Guidry, S.A., Chafetz, H.S., 2003. Anatomy of siliceous hot springs: examples from yellowstone national park, Wyoming, USA. Sediment. Geol. 157, 71-106.

Guido, D.M., Campbell, K.A., 2011. Jurassic hot spring deposits of the Deseado Massif (Patagonia, Argentina): characteristics and controls on regional distribution. J. Volcanol. Geotherm. Res. 203, 35–47.

Guido, D.M., Campbell, K.A., 2012. Diverse subaerial and sublacustrine hot spring settings of the Cerro Negro epithermal system (Jurassic, Deseado Massif), Patagonia, Argentina. J. Volcanol. Geotherm. Res. 229–230, 1–12.

Hamilton, A., Campbell, K., Rowland, J., Browne, P., 2017. The Kohuamuri siliceous sinter as a vector for epithermal mineralisation, Coromandel Volcanic Zone, New Zealand. Miner. Deposita, 52, 181-196.

Handley, K.M., Campbell, K.A., Mountain, B.W., Browne, P.R.L., 2005. Abiotic–biotic controls on the origin and development of spicular sinter: in situ growth experiments, champagne pool, Waiotapu, New Zealand. Geobiology 3, 93–114.

Herdianita, N.R., Browne, P.R.L., Rodgers, K.A., Campbell, K.A., 2000. Mineralogical and textural changes accompanying ageing of silica sinter. Mineral. Deposita 35, 48–62.

Hinman, N.W., and Lindstorm, R.F., 1996, Seasonal changes in silica deposition in hot spring systems: Chemical Geology, v. 132, p. 237–246.

Hurwitz, S., Manga, M., 2017. The fascinating and complex dynamics of geyser eruptions. Annu. Rev. Earth Planet. Sci. 45, 31–59.

Jones, B., Renaut, R.W., Rosen, M.R., 1999. Actively growing siliceous oncoids in the Waiotapu geothermal area, North Island, New Zealand: Geological Society of London, Journal, v. 156, p. 89–103.

Jones, B., Renaut, R.W., 1997. Formation of silica oncoids around geysers and hot springs at El Tatio, northern Chile. Sedimentology 44, 287–304.

Jones, B., Renaut, R.W., 2003a. Hot spring and geyser sinters: the integrated product of precipitation, replacement and deposition. Can. J. Earth Sci. 40, 1549–1569.

Konhauser, K.O., Phoenix, V.R., Bottrell, S.H., Adams, D.G., Head, I.M., 2001. Microbial–silica interactions in Icelandic hot spring sinter: possible analogues for some Precambrian siliceous stromatolites: Sedimentology, v., 48, p. 415–433.

Konhauser, K. O., Jones, B., Reysenbach, A.-L., & Renaut, R. W., 2003. Hot spring sinters: Keys to understanding Earth's earliest life forms. Canadian Journal of Earth Sciences, 40(11), 1713–1724.

Landrum, J.T., Bennett, P.C., Engel, A.S., Alsina, M.A., Pasten, P.A., Milliken, K., 2009. Partitioning geochemistry of arsenic and antimony, El Tatio geyser field, Chile. Appl. Geochem. 24, 664-676.

Lowe, D.R., Braunstein, D., 2003. Microstructure of high-temperature (>73 °C) siliceous sinter deposited around hot springs and geysers, Yellowstone National Park: the role of biological and abiological processes in sedimentation. Canadian Journal of Earth Sciences 40, 1611–1642.

Lahsen, A., Trujillo, P., 1975. El Tatio geothermal field. Proc. of the Second United Nations Symposium on the Development and Use of Geothermal Resources, San Francisco, California, pp. 157–178.

Lahsen, A., 1988. Chilean Geothermal Resources and their possible utilization. Geothermics 17, 401-410.

Lynne B. Y. and Campbell K. A., 2003. Diagenetic transformations (opal-A to quartz) of low- and mid-temperature microbial textures in siliceous hot-spring deposits, Taupo Volcanic Zone, New Zealand. Can. J. Earth Sci. v. 40, p. 1679–1696.

Lynne, B.Y., Campbell, K.A., Moore, J.N., Browne, P.R.L., 2005. Diagenesis of 1900-year-old siliceous sinter (opal-A to quartz) at Opal Mound, Roosevelt Hot Springs, Utah, U.S.A.Sediment. Geol. v. 179, p. 249–278.

Lynne, B.Y., Campbell, K.A., James, B., Browne, P.R.L., Moore, J.N., 2007. Tracking Crystallinity in Siliceous Hot-Spring Deposits. Am. J. Sci. 307, 612–641.

Lynne, B.Y., Campbell, K.A., Moore, J.N., Browne, P.R.L., 2008. Origin and evolution of the Steamboat Springs siliceous sinter deposit, Nevada, U.S.A. Sediment. Geol. 210, 111–131.

Lynne, B. Y., 2012, Mapping vent to distal- apron hot spring paleo-flow pathways using siliceous sinter architecture: Geothermics, v. 43, p. 3-24.

Lynne, B.Y., 2015. Impact of three common post-depositional environmental settings on siliceous sinter diagenesis: an eight year experiment. J. Volcanol. Geotherm. Res. 292, 84–101.

McKenzie E. J., Brown K. L, Cady S. L., Campbell K. A., 2001. Trace metal chemistry and silicification of microorganisms in geothermal sinter, Taupo Volcanic Zone, New Zealand. Geothermics 30, 483-502.

Munoz-Saez, C., Manga, M., Hurwitz, S., 2018, Hydrothermal discharge from the El Tatio basin, Atacama, Chile: Journal of Volcanology and Geothermal Research, v. 325, p. 25-35.

Nicolau, C., Reich, M., Lynne, B., 2014, Physico-chemical and environmental controls on siliceous sinter formation at the high-altitude El Tatio geothermal field, Chile: Journal of Volcanology and Geothermal Resources, v. 282, p. 60–76.

Pope, J.G., McConchie, D.M., Clark, M.D., Brown, K.L., 2004. Diurnal variations in the chemistry of geothermal fluids after discharge, Champagne Pool, Waiotapu, New Zealand. Chem. Geol. 203, 253–272.

Rodgers, K.A.; Browne, P.R.L.; Buddle, T.F.; Cook, K.L.; Greatrex, R.A.; Hampton, W.A.; Herdianita, N.R.; Holland, G.R.; Lynne, B.Y.; Martin, R., 2004. Silica phases in sinters and residues from geothermal fields of New Zealand. Earth Sci. Rev. 66, 1–61.

Ruff, S.W., Farmer J. D., 2016. Silica deposits on Mars with features resembling hot spring biosignatures at El Tatio in Chile. Nature communications 7, 13554.

Sanchez-Yañez, C., Reich, M., Leisen, M., Morata, D., Barra, F., 2017, Geochemistry of metals and metalloids in siliceous sinter deposits: Implications for elemental partitioning into silica phases: Applied Geochemistry, v. 80, p. 112-123.

Smith, I. J., Lynne, B. Y., Jaworowski, C., Qasim, I., Heasler, H., Foley, D., 2018, The formation of geyser eggs at Old Faithful Geyser, Yellowstone National Park, U.S.A. Geothermics v., 75 p., 105-121.

Tassi F., Aguilera F., Darrah T., Vaselli O., Capaccioni B., Poreda R. J. and Huertas A. D., 2010. Fluid geochemistry of hydrothermal systems in the Arica-Parinacota, Tarapaca and Antofagasta regions (northern Chile). J. Volcanol. Geotherm. Res. 192, 1–15.

Trewin NH, Rice CM, 2004. The Rhynie Hot Springs System: geology, biota and mineralisation. Transactions of the Royal Society of Edinburgh, Earth Sciences 94:246.

Tobler D. J., Shaw S. and Benning L. G., 2009. Quantification of initial steps of nucleation and growth of silica nanoparticles: an in-situ SAXS and DLS study. Geochim. Cosmochim. Acta 73, 5377–5393.

Trujillo, P., 1969. Estudio para el desarollo geotermico en el norte de Chile. Manifestaciones termales de El Tatio, Provencia de Antofagasta: CORFO Project Report.

Walter, M.R., Des Marais, D., Farmer, J.D., and Hinman, N.W. 1996. Lithofacies and biofacies of mid-Paleozoic thermal spring deposits in the Drummond Basin, Queensland, Australia. Palaios, 11: 497–518.

Walter, M.R. 1976. Hot-spring sediments in Yellowstone National Park. In Stromatolites. Edited by M.R. Walter. Developments in Sedimentology, Vol. 20, Elsevier, Amsterdam, The Netherlands, pp.489–498.

Williams, L.A. and Crerar, D.A., 1985. Silica diagenesis, II. General mechanisms. Journal of Sedimentary Petrology v. 55, p. 312–321.

Zeil, W., 1959. Das Fumarolen– und Geysir–Feld westlich der Vulkangruppe des Tatio (Provinz Antofagasta, Chile). Bayerische Akademie der Wissenschaften, Abhandlung der Mathematisch-Naturwissenschaftliche Klasse, Muenchen, Deutschland, p. 22 (n. 96).

Zotov N., and Keppler H., 2002. Silica speciation in aqueous fluids at high pressures and high temperature. Chem. Geol. v.184, p. 71-82.

APPENDIX

Appendix A: Data Repository of chapter 2
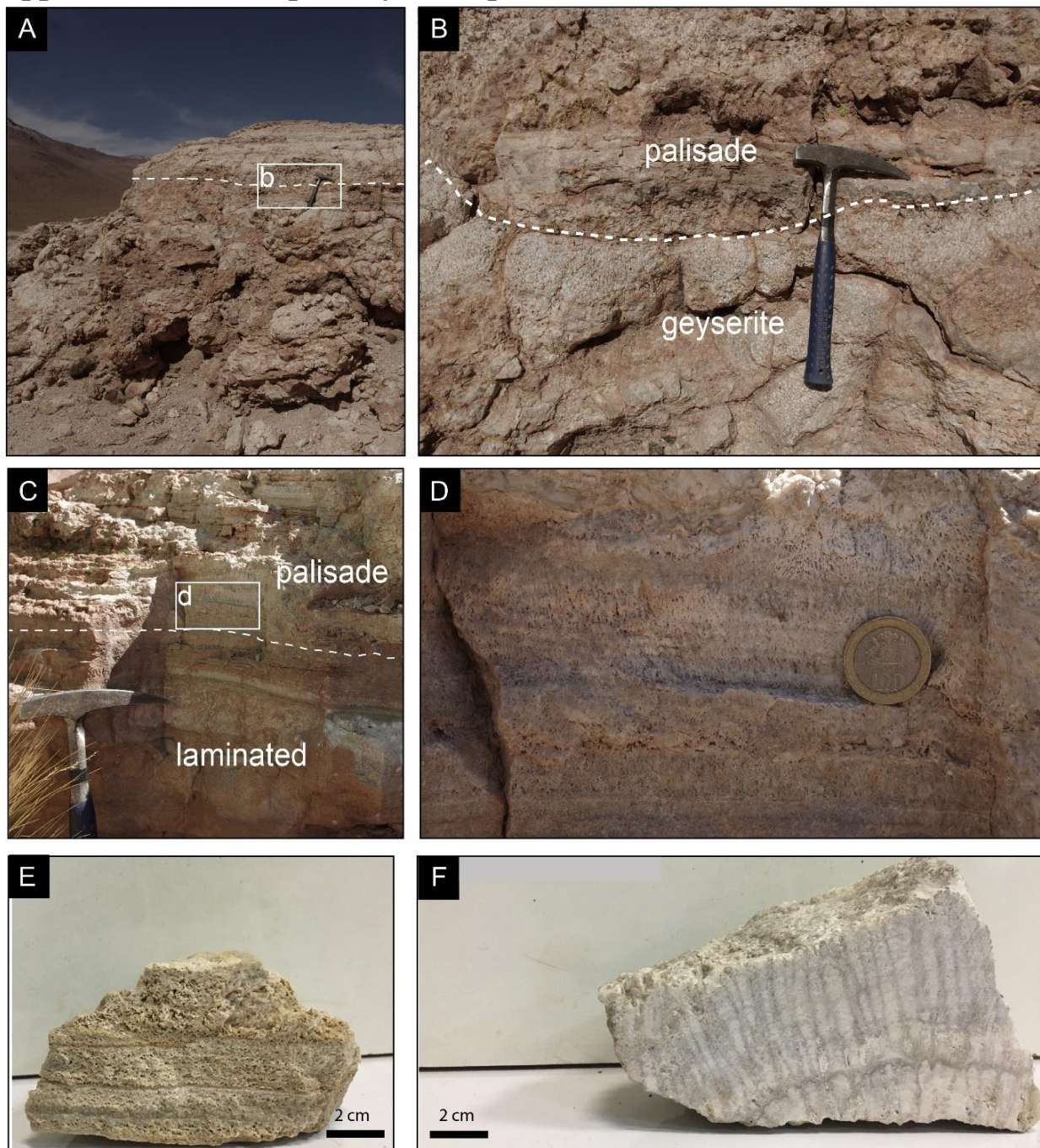
Figure 15. Paleosinter textures. A and B correspond to mound 502. A. Contact between geyserite in the lower part and palisade in the upper part. B. Zoom of the rectangle in A. See hammer for scale. C and D correspond to mound 404. C. Contact between laminated and palisade texture. D. Porous palisade texture. Magnification of the rectangle in C. See coin for scale. E. Palisade texture in sample 404f. F. Geyserite texture corresponding to sample 502m.
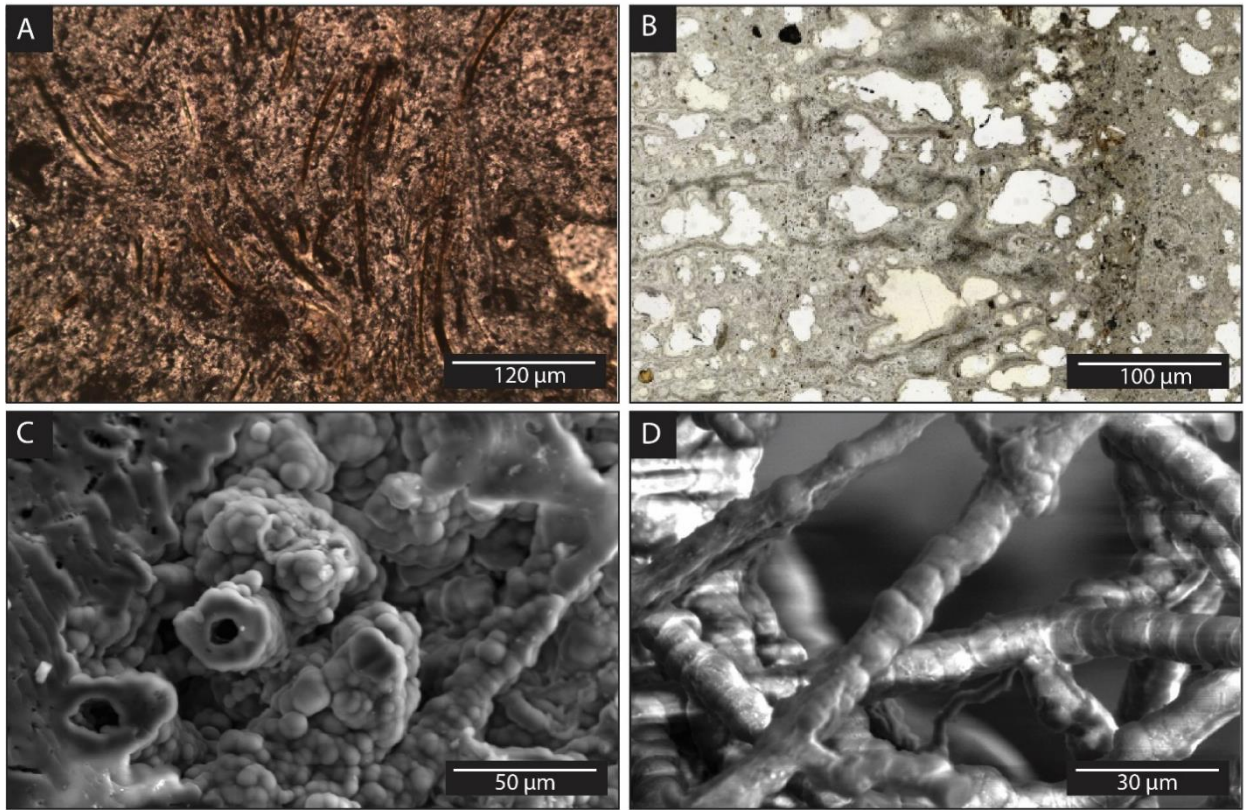
Figure 16. A and B. Photomicrograph of bacteria filaments present in sample 404d. B. Photomicrograph of bacteria filaments and elongated pores perpendicular to the layering present in sample 408t. C and D. Secondary electron SEM images of filament molds partially filled with porous silica (C: Sample 429t; D: Sample 408t).
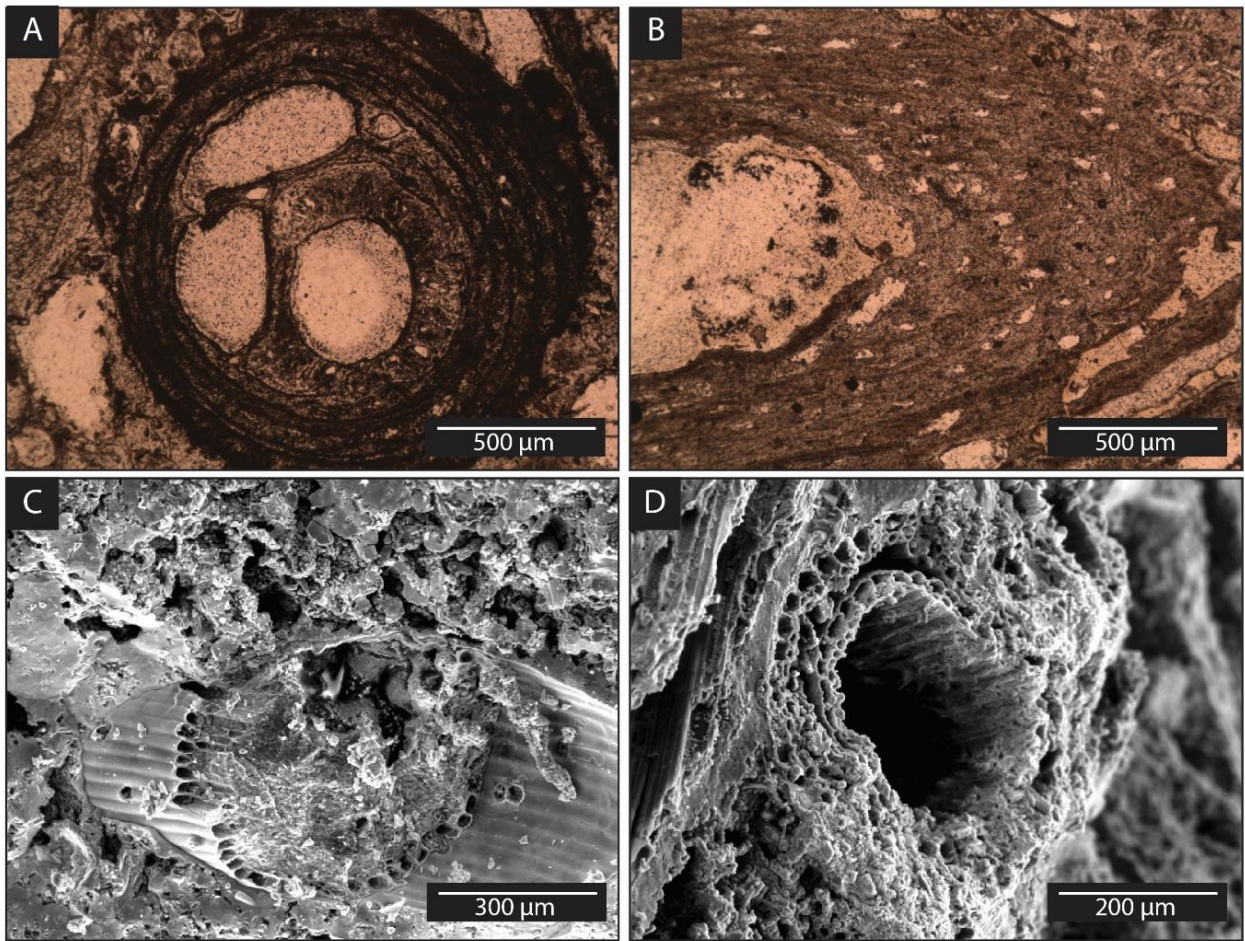
Figure 17. A and B. Photomicrograph of plant fragments present in sample 429b. C and D. Secondary electron SEM images of plant fragments in sample 404c.
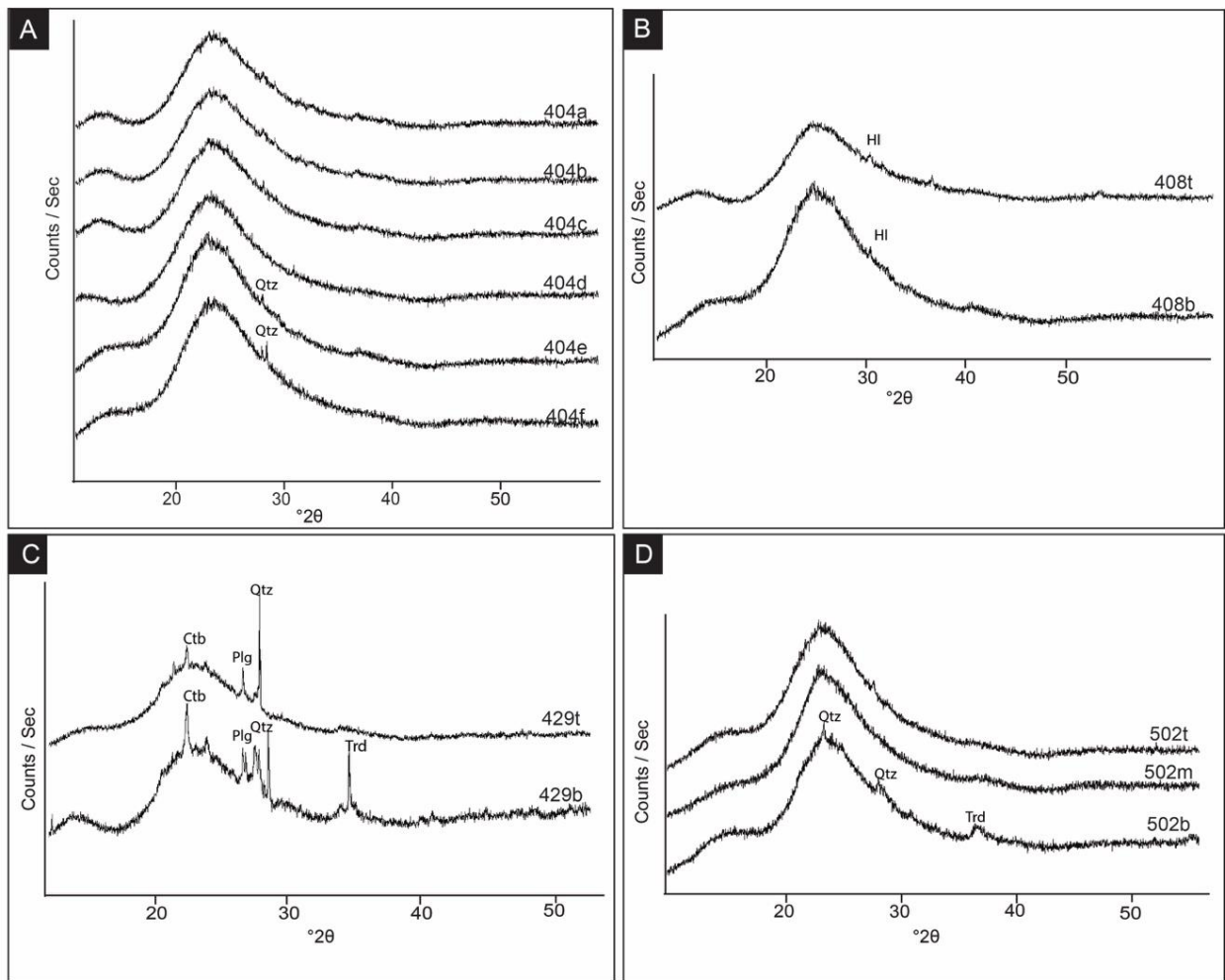
Figure 18. XRD spectra of selected sinter samples. A. 404 B. 408 C. 429 D. 502. Samples 404a,b,c,d 408b,t, 429b,t and 502b and m correspond to opal-A. The broadband is centered at 22.2°Θ, with FWHM values between 6.9°2Θ and 9.3°2Θ. Samples 404e,f, and 502b correspond to opal-A/-CT, and FWHM values vary between 5.7 and 6.1°2Θ. Main accessory minerals phases are labeled and correspond to plagioclase (Plg), halite (Hl), detrital quartz (Qz), tridymite (Trd) and cristobalite (Ctb).
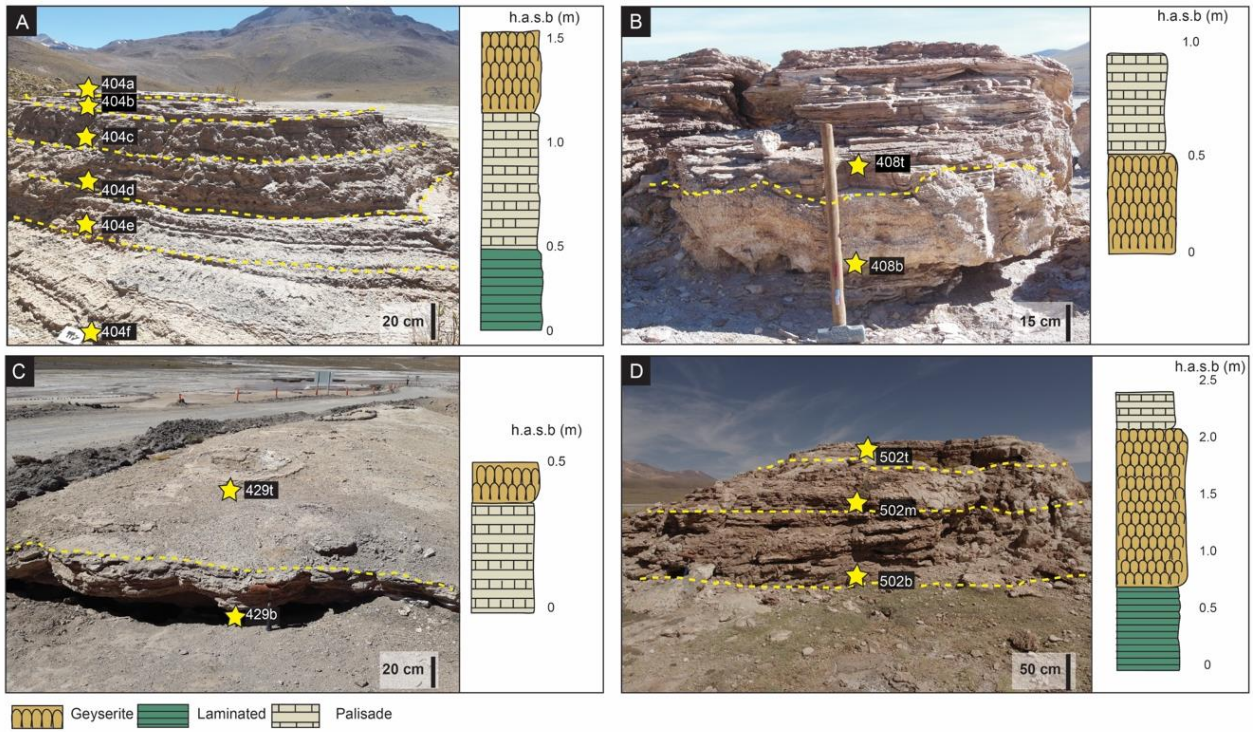
Figure 19. Paleosinter mounds sampled in this study. Stratigraphic profiles detail sample names and textures. h.a.s.b.: height above section base. A.404 B.408 (modified from Munoz-Saez et al., 2016) C.429 D.502. Stars represent sampling sites for dated sinter.
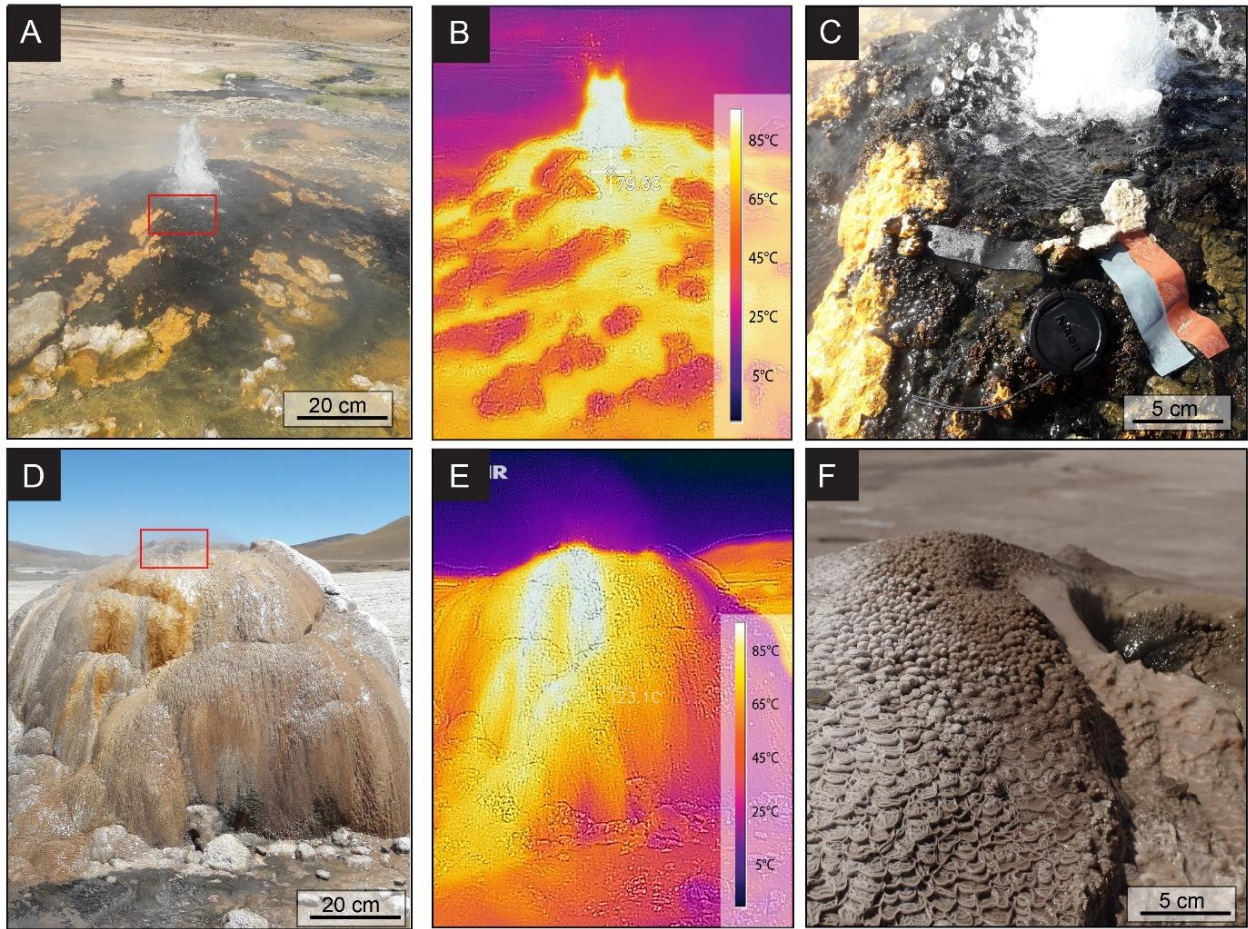
Figure 20. *In situ* silica precipitation experiments. A, B and C correspond to geyser 411. B is a thermal image of A, obtained with FLIR camera. C is a zoom of the red rectangle in A, showing the set-up of the experiment with sandpaper bands on November 2017. See lens cap for scale (55mm diameter). D, E, and F correspond to geyser 412. E is a thermal image of D, obtained with FLIR camera. F is a close up of the rectangle in D, showing the outflow zone where sandpapers were placed. See coin for scale.
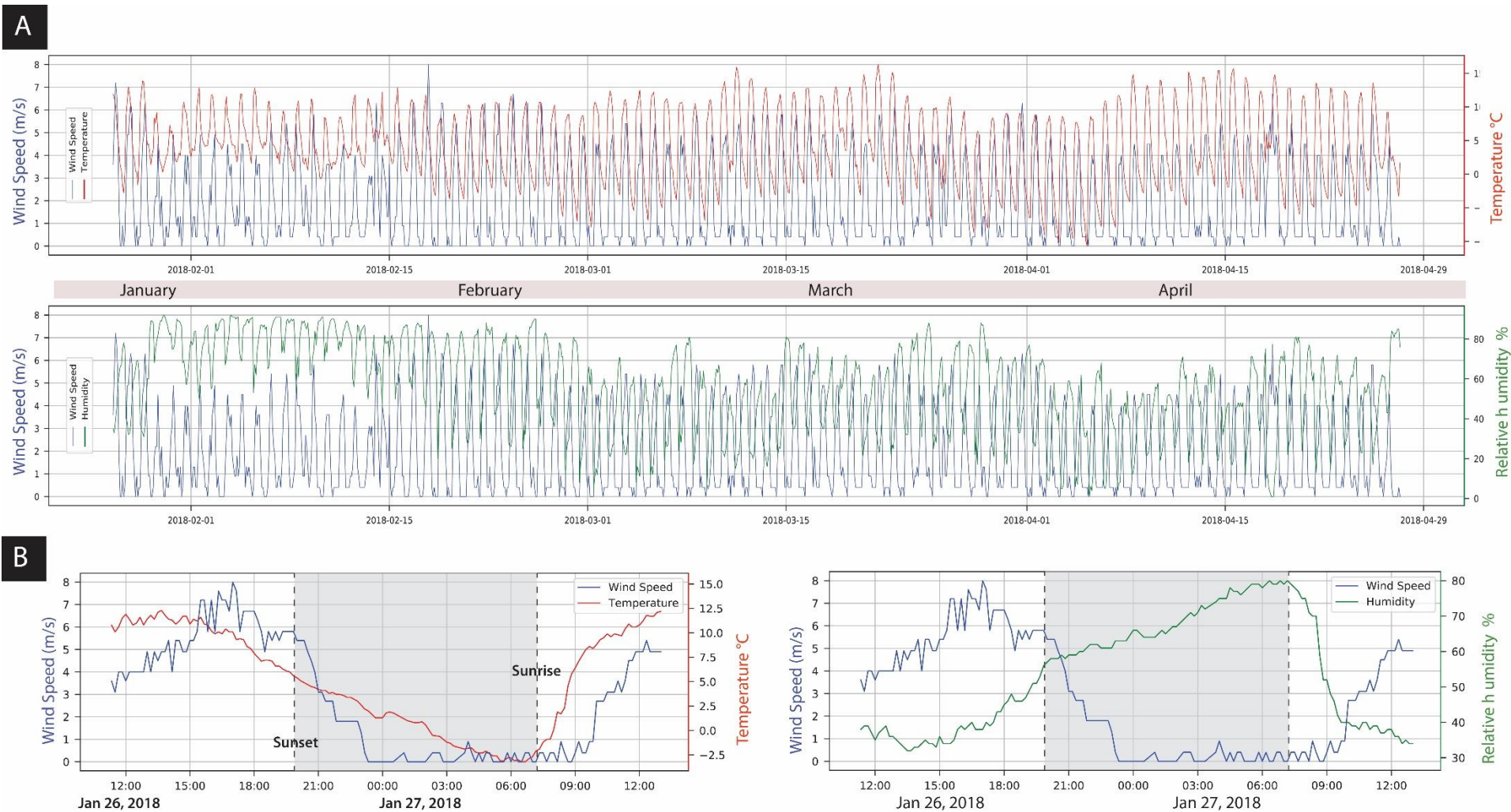
Figure 21. A. Local weather data of the El Tatio Hydrothermal Field from Jan 26 to April 27, 2018, collected at 2-hour intervals. Top: wind speed vs. air temperature. Bottom: the same wind speed vs. air relative humidity. B. Local weather data of the El Tatio Hydrothermal Field from Jan 26 to 27, 2018 at 10-minute intervals. Top: wind speed vs. air temperature. Bottom: the same wind speed vs. air relative humidity. Respective sunrise and sunset times were indicated by the dash lines and night times were shaded in gray.

Table 3. Radiocarbon ages

Sample code	Lab code	Fraction modern	±	$d^{13}C$ (‰)	±	^{14}C age years B.P.	±	cal age * cal years B.P.		Median proability
404a	198595	0.482	0.0012	-24.03	0.1	5860	25	6527	6696	6626
404b	198596	0.454	0.0040	N.D.[#]	N.D.[#]	6330	80	6999	7340	7207
404c	198594	0.358	0.0062	N.D.[#]	N.D.[#]	8230	140	8718	9480	9147
404d	198611	0.344	0.0020	N.D.[#]	N.D.[#]	8550	50	9437	9548	9506
404e	198613	0.312	0.0010	N.D.[#]	N.D.[#]	9340	30	10375	10588	10501
404e[†]	198593	0.304	0.0014	-25.12	0.1	9565	40	10666	10892	10856
404f	198612	0.259	0.0009	N.D.[#]	N.D.[#]	10840	30	12683	12744	12711
502t	198602	0.971	0.0037	N.D.[#]	N.D.[#]	230	35	139	230	197
502m	198601	0.806	0.0014	-20.42	0.1	1730	15	1540	1613	1585
502m[†]	198618	0.799	0.0014	N.D.[#]	N.D.[#]	1805	15	1611	1673	1648
502b	198600	0.758	0.0014	-20.51	0.1	2220	15	2221	2307	2241
408t	198614	0.933	0.0018	-25.02	0.1	555	20	511	548	531
408b	191794	0.407	0.0022	N.D.[#]	N.D.[#]	7220	45	7930	8065	7993
429t	198617	0.721	0.0014	-22.41	0.1	2625	20	2700	2764	2737
429b	191803	0.629	0.0052	-21.07	0.1	3720	70	3832	4236	4015

*Using the SHCal13 dataset (Hogg et al., 2013). Calibrated ages are presented as mean ages with 2 sigma (95%) confidence limits

[†]Duplicate

[#]N.D= not determined

Table 4. Precipitation rates based on radiocarbon data

Lab code	Sample	Texture	Bottom	Top	Thickness (m)	^{14}C age	±	ΔT (yearss)	Area (m²)	Volume (m³)	Density (kg/m³)§	Mass (kg)	kg/m²	Precipitation rate kg /yrs per m²	mm/yr
198600	502b (bottom)	laminated	0	0.7	0.7	2220	15	**490**	56	39.2	1800	70560	1260	**2.57**	**1.42**
198601	502m	geyserite	0.7	1.9	1.2	1730	15	**1500**	52	67.2	1800	120960	2160	**1.44**	**0.8**
198618	502m†					1805	15				1800				
198602	502t (top)	palisade	1.9	2.4	0.5	230	35		50	28	1800	50400	900		
				Height	2.4										
198612	404f (bottom)	laminated	0	0.7	0.7	10840	30	**1275**	46	32.2	1800	57960	1260	**0.988**	**0.549**
198613	404e	laminated	0.7	0.9	0.2	9340	30	**1015**	44	8.8	1800	15840	360	**0.355**	**0.197**
198593	404e†					9565	40				1800				
198611	404d	palisade	0.9	1	0.1	8550	50	**320**	43	4.4	1800	7920	180	**0.563**	**0.313**
198594	404c	palisade	1	1.2	0.2	8230	140	**1900**	42	8.8	1800	15840	360	**0.189**	**0.105**
198596	404b	palisade	1.2	1.3	0.1	6330	80	**470**	41	4.4	1800	7920	180	**0.383**	**0.213**
198595	404a(top)	geyserite	1.3	1.5	0.2	5860	25	**5860**		8.8	1800	15840	360		**0.034**
				Height	1.5										
191803	429b (bottom)	palisade	0	0.3	0.3	3720	70	**1095**	22	6.6	1800	11880	540	**0.49**	**0.274**
198617	429t (top)	geyserite	0.3	0.5	0.2	2625	20			4.4	1800	7920	360		
				Height	0.5										
191794	408b (bottom)	geyserite	0	0.5	0.5	7220	45	**6665**	51	25.5	1800	45900	900	**0.14**	**0.075**
198614	408t (top)	palisade	0.5	0.5	0.8	555	20			40.8	1800	73440	1440		
				Height	0.8										

† duplicate

§ (Herdianita et al., 2000)

Table 5. Precipitation rates based on in situ experiments

Sample	Longitude	Latitude	Original weight (g)	Total weight (g)	Area (m²)	Weight (g)/ 6 months	Weight (g)/ 1 year	Weight (kg)/ 1 year	kg/years per m²
412 a	68°0´32´´W	22°19´41´´ S	0,9381	2,5913	0,0025	1,6532	3,3064	0,0033064	1,32256
412 b	68°0´32´´W	22°19´41´´ S	1,2	4,3729	0,0025	3,1729	6,3458	0,0063458	2,53832
412 c	68°0´32´´W	22°19´41´´ S	1,37	2,4232	0,0025	1,0532	2,1064	0,0021064	0,84256
411 a	68°2´46´´W	22°20´30´´ S	0,9381	4,0892	0,0025	3,1511	6,3022	0,0063022	2,52088
411 b	68°2´46´´W	22°20´30´´ S	1,2	4,8501	0,0025	3,6501	7,3002	0,0073002	2,92008
411 c	68°2´46´´W	22°20´30´´ S	1,37	2,6972	0,0025	1,3272	2,6544	0,0026544	1,06176

Table 6. Silica saturation

Site	SiO₂ (ppm)	T (°C)	log k*	k	SiO₂ sat. ratio
411	283	78.8	-2.32	0.0047	0.99
412	113	75.3	-2.34	0.0045	0.42

*log(K)=-8.476 - 485.24 ·T-1 - 2.268·10-6 ·T2 +3.068 · log(T)

Radiocarbon ages

Thirteen sinter samples were cut, cleaned, and grinded. The fine-grained samples were later treated with 1 N HCl for 24 h and rinsed with ultrapure water. Then, all samples were digested in 48% HF. The remaining carbonaceous (non-soluble) material was rinsed with ultrapure water and centrifuged. The supernatant was discarded and the carbonaceous precipitate was rinsed with ultrapure water several times. The samples were analyzed for ^{14}C at the UC Irvine Keck-CCAMS facility. The age is reported as before present (B.P.), where present is AD 1950 (Stuiver and Polach, 1977). Calibrated ages obtained on CALIB (http://calib.qub.ac.uk) using the SHCal13 dataset (Hogg et al., 2013) are also reported. Calibrated ages are presented as mean ages with a 2σ confidence level. All results were corrected for isotopic fractionation using δ^{13}C values measured with the AMS spectrometer, but these may differ from the isotope ratios of the original material due to fractionation during AMS sample preparation and/or the measurement itself and are not reported. However, seven samples had a sufficient quantity of carbon collected from the combustion to prepare a separate aliquot of CO_2 for δ^{13}C analysis, by stable isotope ratio mass spectrometer (IRMS). δ^{13}C values for those samples were measured to a precision of <0.1‰ relative to PDB, using a Thermo Finnigan Delta Plus IRMS with Gas Bench input at UC Irvine (Table 3).

X-ray diffraction

Powder X-ray diffraction (XRD) was used to identify silica phases and accessory minerals according to established protocols (Herdianita et al., 2000; Lynne et al., 2007). The analyses were carried out using a Siemens Diffractometer model D-5000 at the Physics Department of the Universidad de Chile. The untreated powder samples (<200 mm) were scanned at a rate of 0.6°2/min, with a step size of 0.01°, from 0 to 40°2, and operating conditions of 40 kV and 30 mA. Accessory minerals were identified using the XPowder12 software. In all diffractograms, the value of the Full Width at Half Maximum (FWHM) was measured by fitting the curve and baseline

manually (Lynne et al., 2007). The FWHM is the main parameter used to determine the degree of structural disorder in different non- crystalline silica (Smith, 1998; Lynne et al., 2007).

Samples consist mainly of opal-A, in agreement with previous studies (Fernandez-Turiel et al., 2005; Garcia-Valles et al., 2008; Nicolau et al, 2014). Opal-A/-CT was recognized in samples 404 e and f, and 502b. FWHM values range from 6.9°2Θ to 9.3°2Θ (Fig. 18), in agreement with Garcia-Valles (2008) (5.7 and 10.6 Δ°2θ), independent of fabric type, being similar among all samples. Higher values have been reported by Nicolau et al. (2014), reaching 12°2Θ, placing El Tatio as the sinter with the highest structural disorder. This particular feature has been attributed to cation incorporation into the silica structure and/or the occurrence of micro- to nano-scale accessory minerals, related to high evaporation conditions (Nicolau et al., 2014; Sanchez-Yañez et al., 2017). In general, values of FWHM decrease with increasing sample age in geyser mounds reaching a difference of 2°2Θ between the bottom and the top, varying from opal-A to opal A-CT. However, these changes cannot be extrapolated to other mounds. For instance, the youngest sample does not present the wider FWHM (Fig. 18). Our results show that opal-A may persist over time, until 8 ka B.P. Certainly, the FWHM changes observed in mounds 404 and 502 in the present study are consistent with the pattern of behavior found by Herdianita et al. (2000), Smith et al., (2003) and Lynne et al., (2007), who reported an overall decrease in FWHM with time. However, its maturation varies from deposit to deposit, probably resulting from different discharge conditions, and therefore, variability in the dissolution-reprecipitation processes. Overall, these sinters are still mineralogically immature.

In situ experiment
The experiments consisted of placing three 25 cm^2 sandpaper sheets that represent a naturally rough surface near-vent areas of each site (Fig. 4C). The experiments were performed from November 2017 to April 2018. The mineralized sandpaper sheets were collected and placed into sterilized plastic tubes and then dried at room temperature. The sheet/silica samples were weighted, and the amount of precipitated silica was determined by subtracting the sandpaper sheet weight from the dried sheet/silica sample. The water temperature at site 411 and 412 were 78.8 °C and 75.3 °C, respectively (Fig. 4D; Fig. 20). At each site, the thermal water was filtered using a 0.45 μm millipore membrane and then collected in 125 ml bottles. Water samples were analyzed for dissolved silica, using inductively coupled plasma optical emission spectrometry (ICP-OES). The concentration of dissolved SiO_2 at sites 411 and 412 was 283 mg/L and 113 mg/L, respectively.

The significantly higher precipitation rates reported at Wairakei (maximum of 350 kg/years/m^2; Mountain et al., 2003) and Reykjanes (maximum of 304 kg/years/ m^2; Tobler et al., 2008) were obtained from wastewater drains at geothermal power plants and hence, do not represent natural discharges. Also, *in situ* studies undertaken at the Map of Australia Pool, at Orakei Korako, Taupo Volcanic Zone, display high precipitation rates (Lynne et al., 2019). In this study, samples were taken from discharge channels covered by a plastic pipe, aiming at comparing the precipitation rate on glass slides with mass flow of geothermal fluids. At Yellowstone National Park, USA some studies focussed on calcite precipitation and the formation of travertine (Blank et al., 2002; Spear et al., 2005; Kandianis et al., 2008 and references therein), and did not present sinter growth rates studies. At Dagunguo hot spring, in China, Peng and Jones (2012) documented opal-A accumulated at rates of 0.5 to 0.75 mm/month in an artificial hot pool and higher values in PVC pipes. We did not include this data in our study because they do not represent natural discharges. In addition, tephrochronological ages were obtained at Geysir, Iceland, intercalated

with silica, but no precise silica sinter precipitation rates could be obtained to compare with our data (Jones et al., 2007).

Scanning Electron Microscopy

In order to obtain morphological and textural data, sinter samples were examined using a FEI Quanta 250 Scanning Electron Microscope (SEM) at the Universidad de Chile. The SEM is equipped with a secondary electron (SE), energy-dispersive X-ray spectrometry (EDS), backscattered electron (BSE) and cathodoluminescence (CL) detectors. The analyses were performed using a spot size of 1 to 3 m, an accelerating voltage of 5 to 20 keV, a beam intensity of 80 mA, and a working distance of 10 mm.

Aerial Drone Imaging

The aerial images were acquired using DJI Mavic Pro drone with the on-board camera at 12MP resolution. Images were recorded from a height between 20 and 33 meters with sufficient overlaps (>85%). This ensures that every point on the surface was captured more than 5 times (downstream software image processing then chooses the sharpest pixels out of these overlapping images to generate a combined final 2D or 3D map). The images were stitched together using the commercially available Pix4D Mapping Software to combine all images into a map with a resolution better than 1.0 cm/pixel.

Meteorological Data

Meteorological data including temperature, wind speed and relative humidity were collected with a weather station (Vantage Vue, Davis Instruments Co., Hayward, California, USA) that was installed on site near the entrance (22°21'3.38"S, 68° 0'54.21"W), which is about 1 km away from the main hydrothermal field. Short-term meteorological data were collected for one full day from Jan 26 to 27, 2018 at 10-minute intervals and long-term data were collected continuously from Jan 27, 2018, until April 27, 2018, at 2-hour intervals. Local sunrise and sunset times were retrieved from < https://www.timeanddate.com/sun/> on Jan 21, 2019.

The 10-minute interval meteorological data from Jan 26 to 27, 2018 (Fig. 21A) revealed that local air temperature rises immediately following sunrise to between 10 to 13 °C at noon. This maximum day temperature is near-constant all year round (Fernandez-Turiel et al., 2005). Wind speed shows a consistent ~2 hours lag after the air temperature increase, indicating that wind generation is likely linked to solar heating which warmed the air in the first place. Relative humidity of the air decreased rapidly following sunrise, coinciding in time with the local wind generation, indicating that the local humid air (which accumulated over the night while wind speed is low) is quickly displaced by dry, regional air through wind action. Wind speed reaches to a maximum between 2-6 pm, while the air temperature is high and humidity is low, suggesting that all three factors combine to produce the maximum effect of the evaporation of the hydrothermal fluid as well as the depositing solid sinter material. Long-term meteorological data (Fig. 21B) further confirms this daily trend, showing that sinter deposition across the El Tatio region likely experiences the same fashion of evaporative drying on a daily basis driven by regional atmospheric processes.

References

Blank, C.E., Cady, S.L., Pace, N.R., 2002, Microbial composition of near-boiling silica- depositing thermal springs throughout Yellowstone National Park: Appl. Environ. Microbiol. 68, 5123–5135

Fernandez-Turiel, J.L., Garcia-Valles, M., Gimeno-Torrente, D., Saavedra-Alonso, J., Martinez-Manent, S., 2005, The hot spring and geyser sinters of el Tatio, northern Chile: Sediment. Geol., v. 180, p. 125–147.

Garcia-Valles, M., Fernandez-Turiel, J.L., Gimeno-Torrente, D., Saavedra-Alonso, J., Martinez-Manet, S., 2008, Mineralogical characterization of silica sinters from the el Tatio geothermal field, Chile: Am. Mineralogist, v. 93, p. 1373–1383.

Herdianita, N.R., Browne, P.R.L., Rodgers, K.A., and Campbell, K.A., 2000, Mineralogical and textural changes accompanying ageing of silica sinter: Mineralium Deposita, v. 35, p. 48–62.

Hogg, A., Hua, Q., Blackwell, P.G., Niu, M., Buck, C.E., Guilderson, T.P., Heaton, T.J., Palmer, J.G., Reimer, P.J., Reimer, R.W., Turney, C.S.M., Zimmerman, S.R.H., 2013, SHCal13 Southern Hemisphere calibration, 0–50,000 years cal B.P.: Radiocarbon, v. 55, p. 1889–1903.

Jones, B., Renaut, R.W., Torfason, H., Bernhart Owen, R., 2007, The geological history of Geysir, Iceland: a tephrochronological approach to the dating of sinter: Journal of the Geological Society, London, v. 164, p. 1241–1252.

Kandianis, M.T., Fouke, B.W., Johnson, W., Veysey II, J., Inskeep, W.P., 2008, Microbial biomass: a catalyst for CaCO3 precipitation in advection-dominated transport regimes: GSA Bull., v. 120, p. 442–450.

Lynne, B.Y., Campbell, K.A., James, B., Browne, P.R.L., Moore, J.N., 2007, Tracking crystallinity in siliceous hot-spring deposits: American Journal of Science, v. 307, p. 612–641.

Lynne, B. Y., Boudreau, A., Smith, I. J., Smith G. J., 2019, Silica accumulation rates for siliceous sinter at Orakei Korako geothermal field, Taupo Volcanic Zone, New Zealand: Geothermics, v. 78, p. 50-61.

Mountain, B.W., Benning, L.G., Boerema, J.A., 2003, Experimental studies on New Zealand hot spring sinters: rates of growth and textural development: Can. J. Earth Sci. v. 40, p. 1643–1699.

Munoz-Saez, C., Saltiel, S., Manga, M., Nguyen, C., Gonnermann, H., 2016, Physical and hydraulic properties of modern sinter deposits: El Tatio, Atacama: Journal of Volcanology and Geothermal Research, v. 325, p. 156-168.

Nicolau, C., Reich, M., Lynne, B., 2014, Physico-chemical and environmental controls on siliceous sinter formation at the high-altitude El Tatio geothermal field, Chile: Journal of Volcanology and Geothermal Resources, v. 282, p. 60–76.

Peng, X., Jones, B., 2012, Rapid precipitation of silica (opal-A) disguises evidence of biogenicity in high-temperature geothermal deposits: case study from Dagunguo hot spring. China: Sedimentary Geology, v. 257, p. 45–62.

Sanchez-Yanez, C., Reich, M., Leisen, M., Morata, D., Barra, F., 2017, Geochemistry of metals and metalloids in siliceous sinter deposits: Implications for elemental partitioning into silica phases: Applied Geochemistry, v. 80, p. 112-123.

Smith, D.K., 1998, Opal, cristobalite, and tridymite: noncrystallinity versus crystallinity, nomenclature of the silica minerals and bibliography: Powder Diffraction, v. 13, p. 2–19.

Smith, B.Y., Turner, S.J., Rodgers, K.A., 2003, Opal-A and associated microbes from Wairakei, New Zealand: the first 300 days: Mineral. Mag. v. 67, p. 563–579.

Spear, J.W., Walker, J.J., McCollom, T.M., Pace, N.R., 2005. Hydrogen and bioenergetics in the Yellowstone geothermal ecosystem: Proc. Natl. Acad. Sci. U. S. A. v. 102, p. 2555–2560.

Stuiver, M., Polach, H.A., 1977, Discussion: reporting of 14C data: Radiocarbon, v. 19, p. 355–363.

Tobler, D.J., Stefansson, A., Benning, L.G., 2008, In situ grown silica sinters in Icelandic geothermal areas: Geobiology, v. 6, p. 481–502.

Appendix B: X-Ray Diffraction and Petrography

The following figures include photographs of all samples studied. In the left panel, there is a scanned thin section of the selected samples and in the right panel a representative photograph of the sample under polarized light. Then, the XRD traces of all the samples not presented previously are included in figure 43.
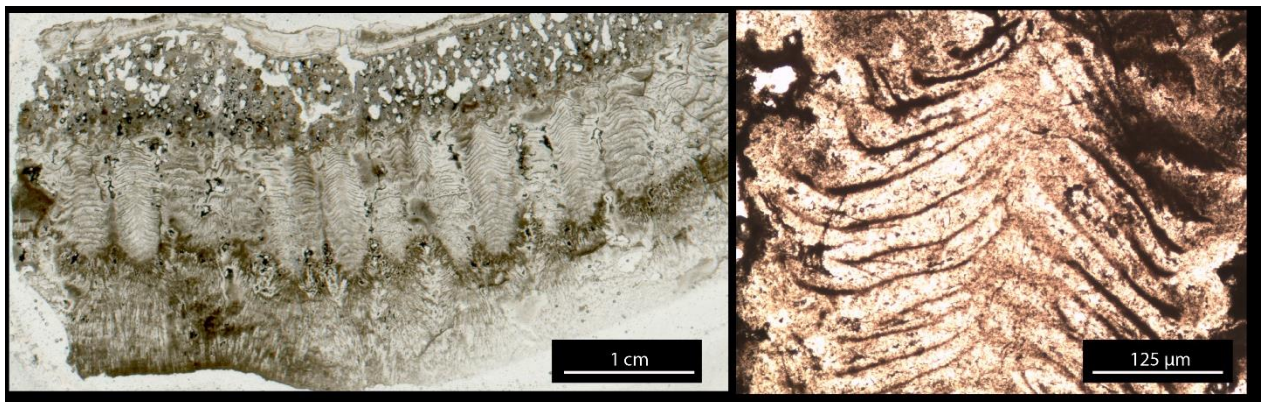
Figure 22. Sample 404a. Cross view of columnar geyserite texture with tubular microfossils.
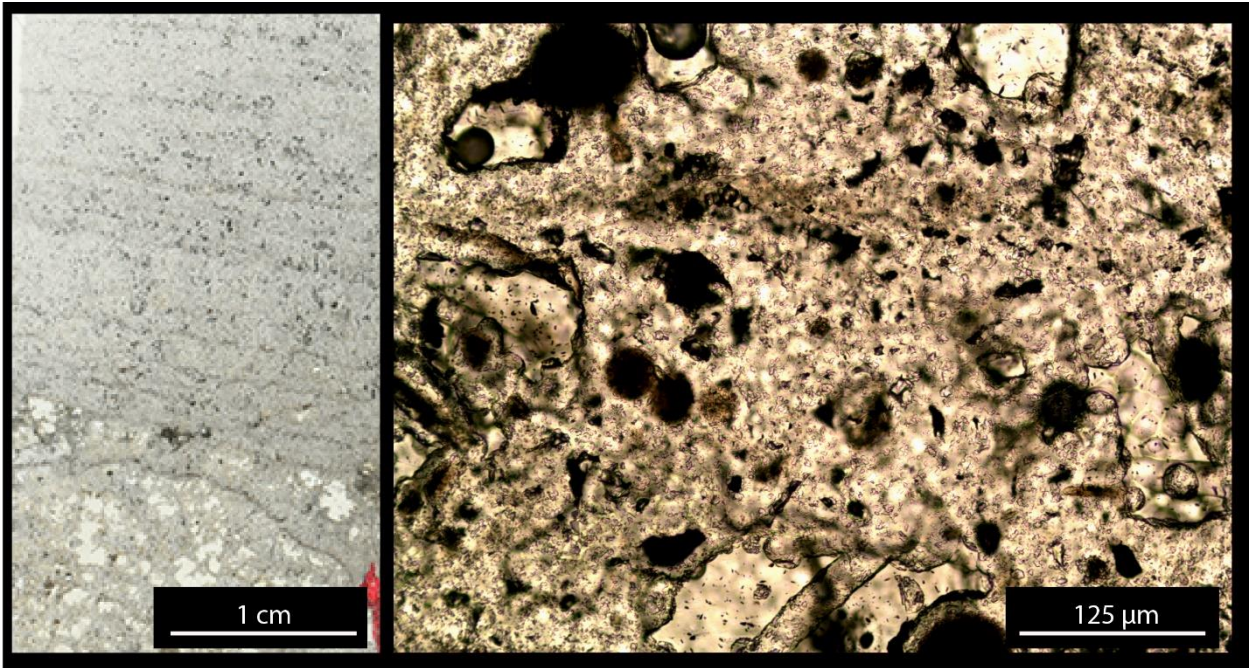
Figure 23. Sample 404b. Peloidal fabrics in silica matrix of laminated texture.
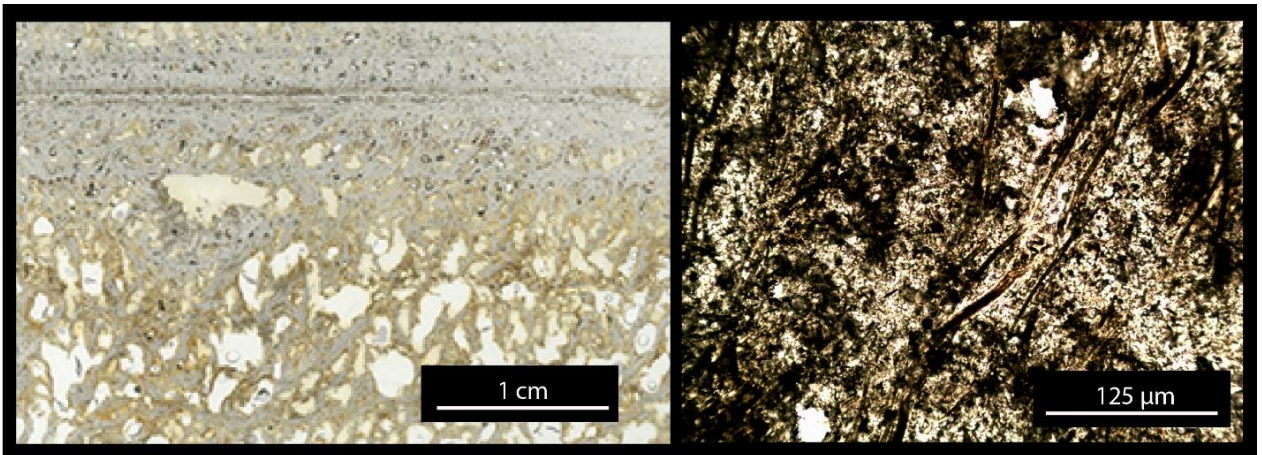
Figure 24. Sample 404c. Sharp contact between weakly laminated layer and the porous layer. In the right panel, vertically oriented microbes dominated by cyanobacteria, corresponding to the laminated layer.
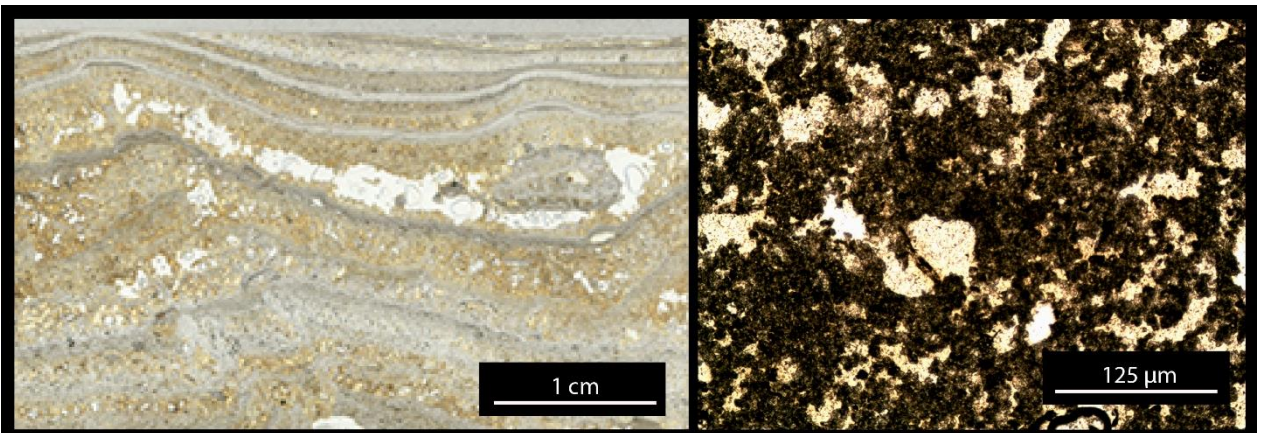
Figure 25. Sample 404d. Laminated layer with porous features.

67
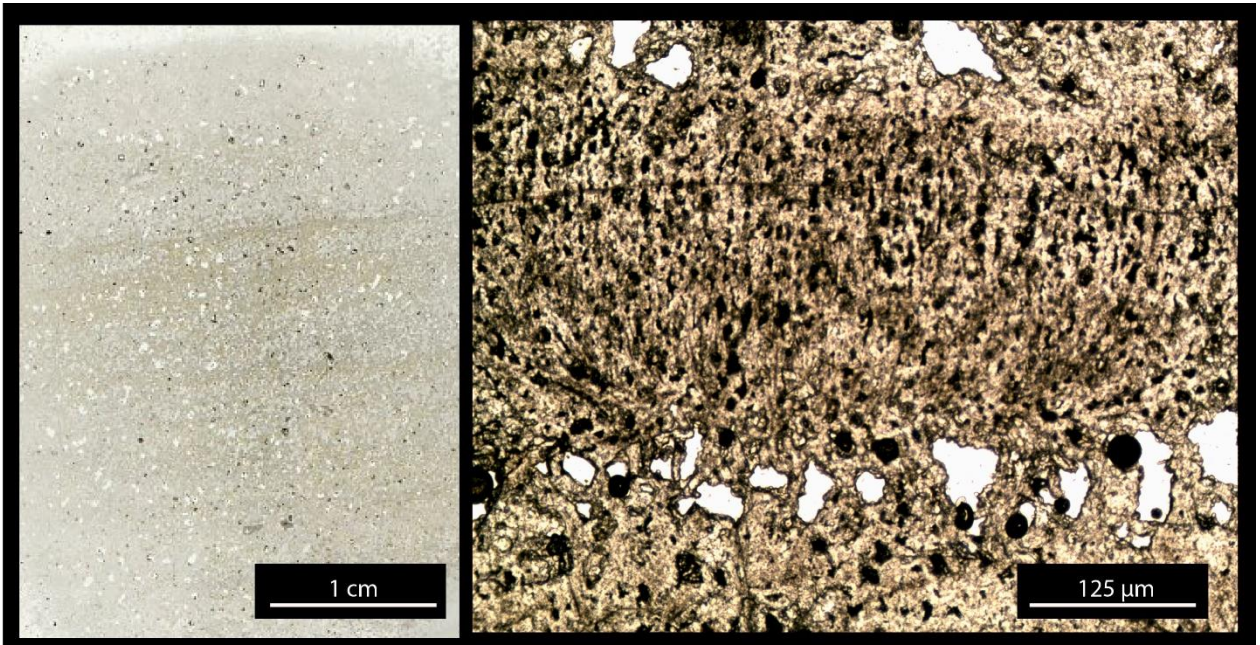
Figure 26. Sample 404e. Weak lamination with thin 'bushy' dendritic stromatolites.
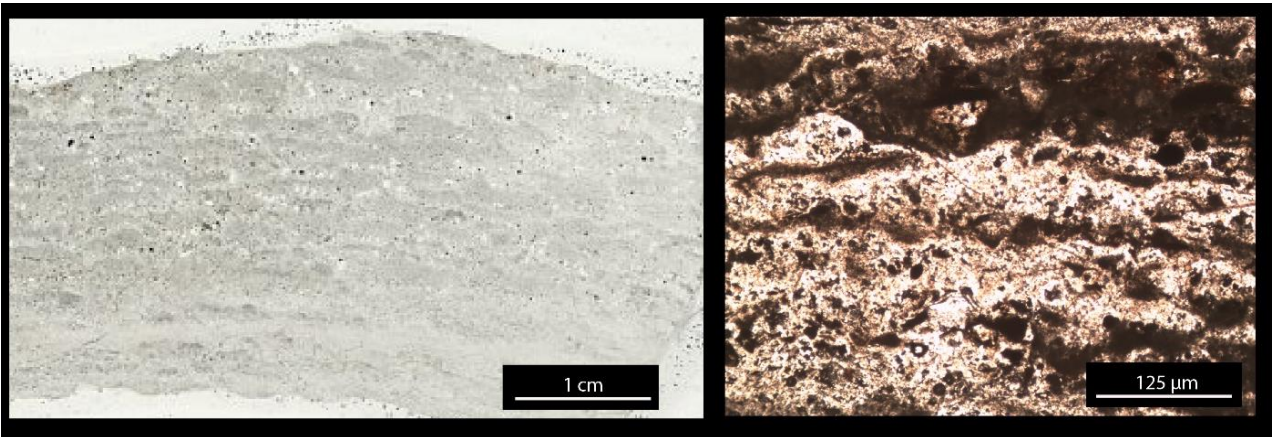
Figure 27. Sample 404f. Laminated texture.
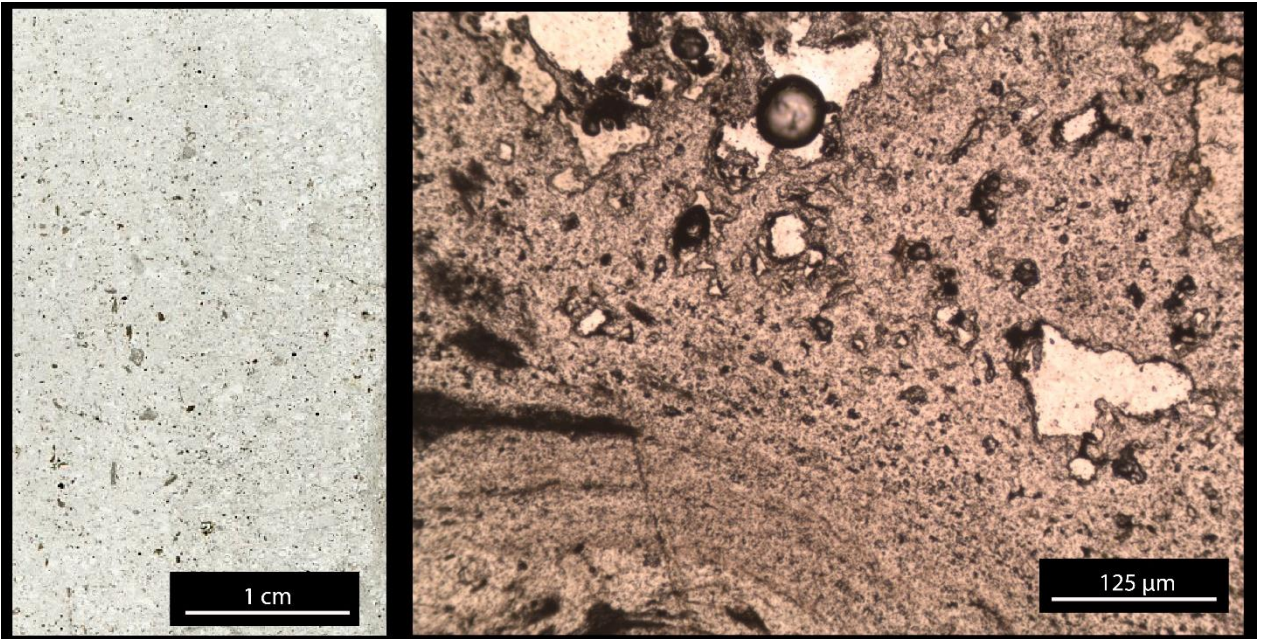
Figure 28. Sample 408t. Porous silica texture with laminated silica at the bottom
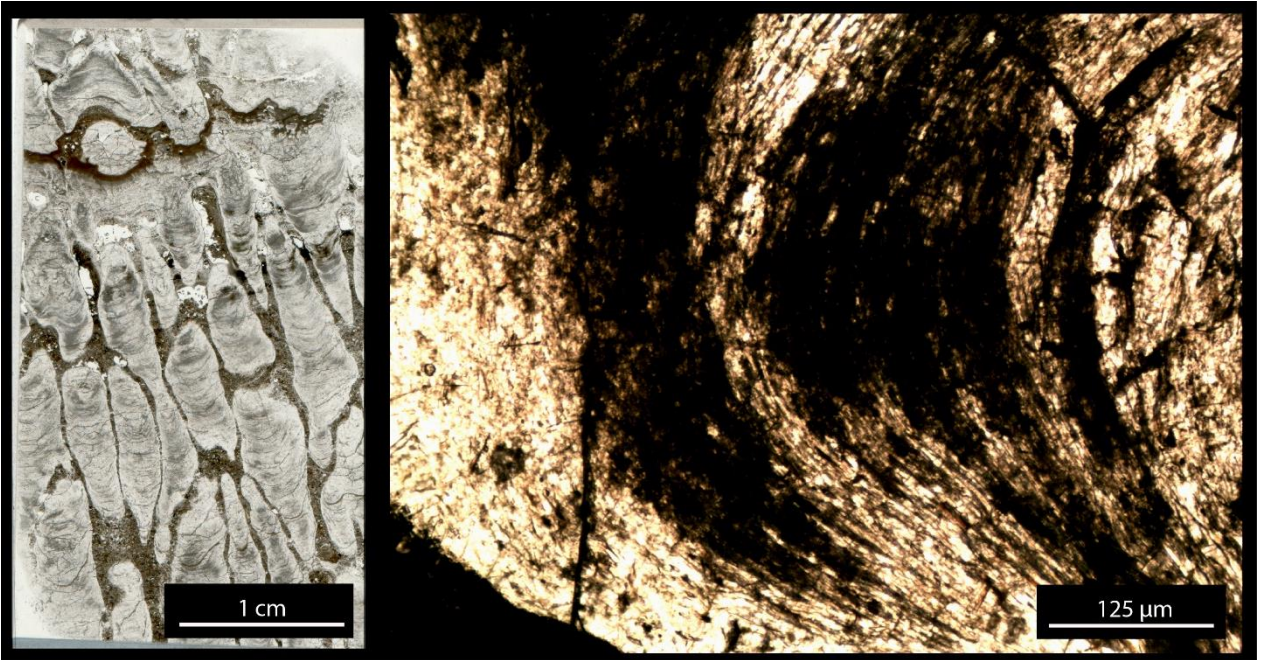
Figure 29. Sample 408b. Columnar geyserite con upward convex lamination.
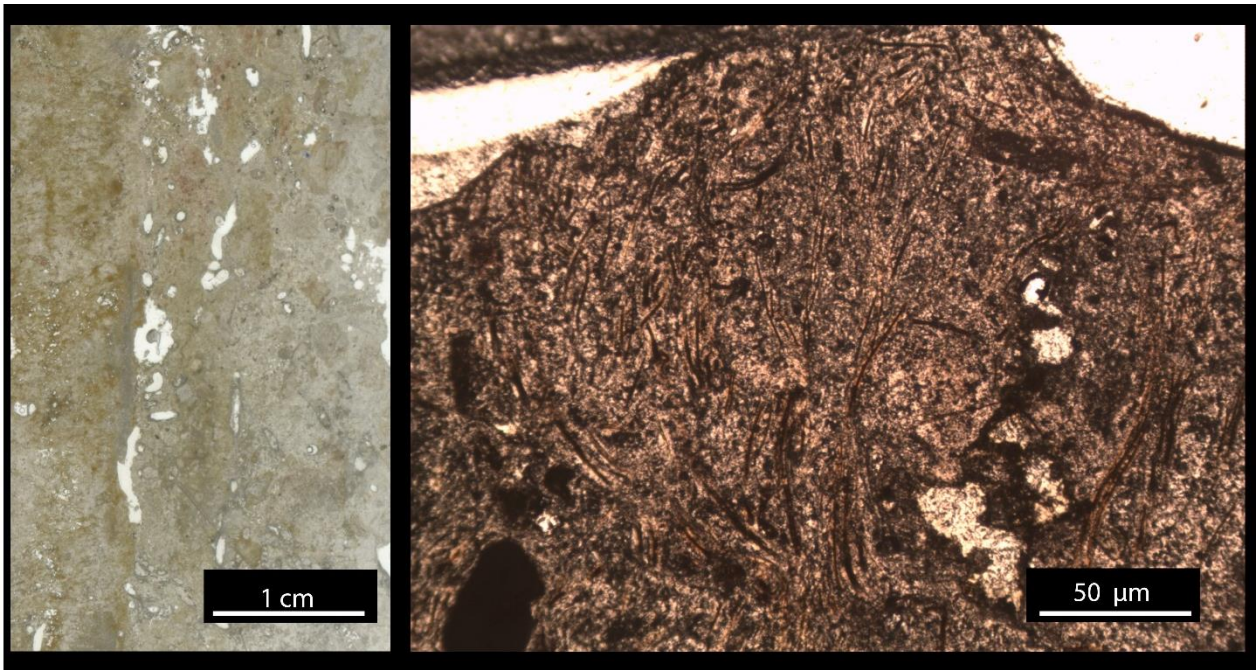
Figure 30. Sample 412. Longitudinal section of vertically oriented, tubular microfossils, encased in a silica matrix.
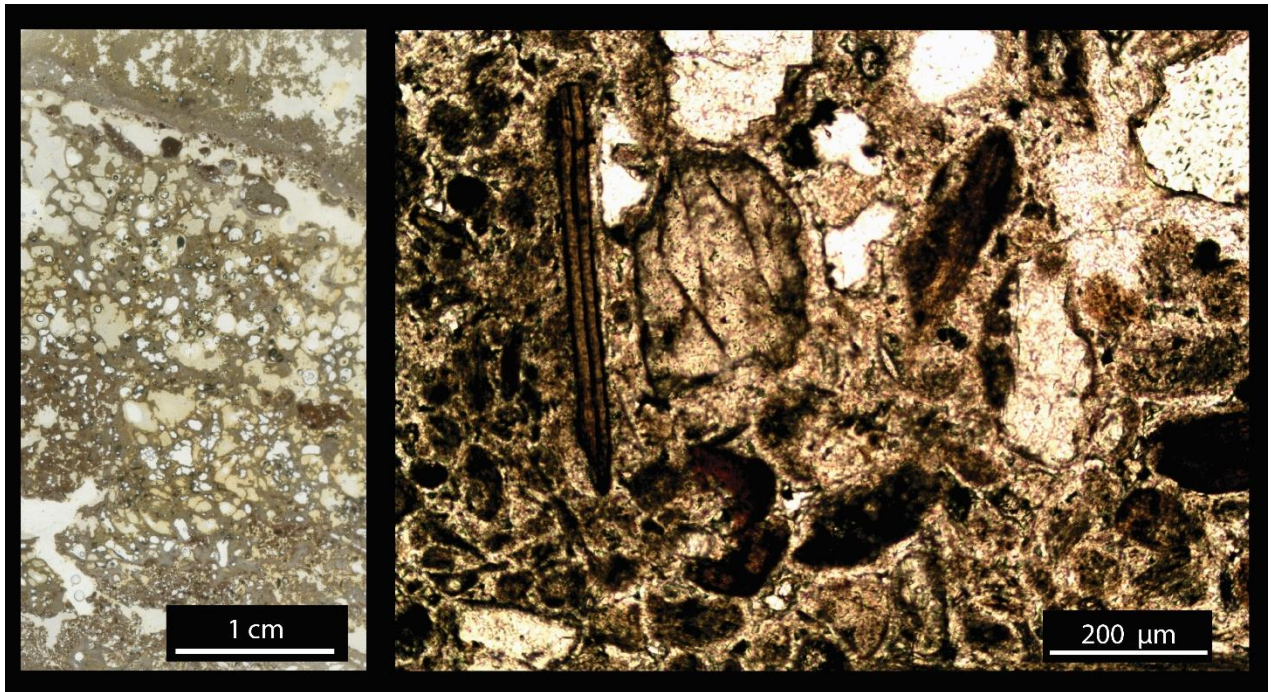
Figure 31. Sample 414. Porous lamination with fragments of biotite and peloidal fabric.
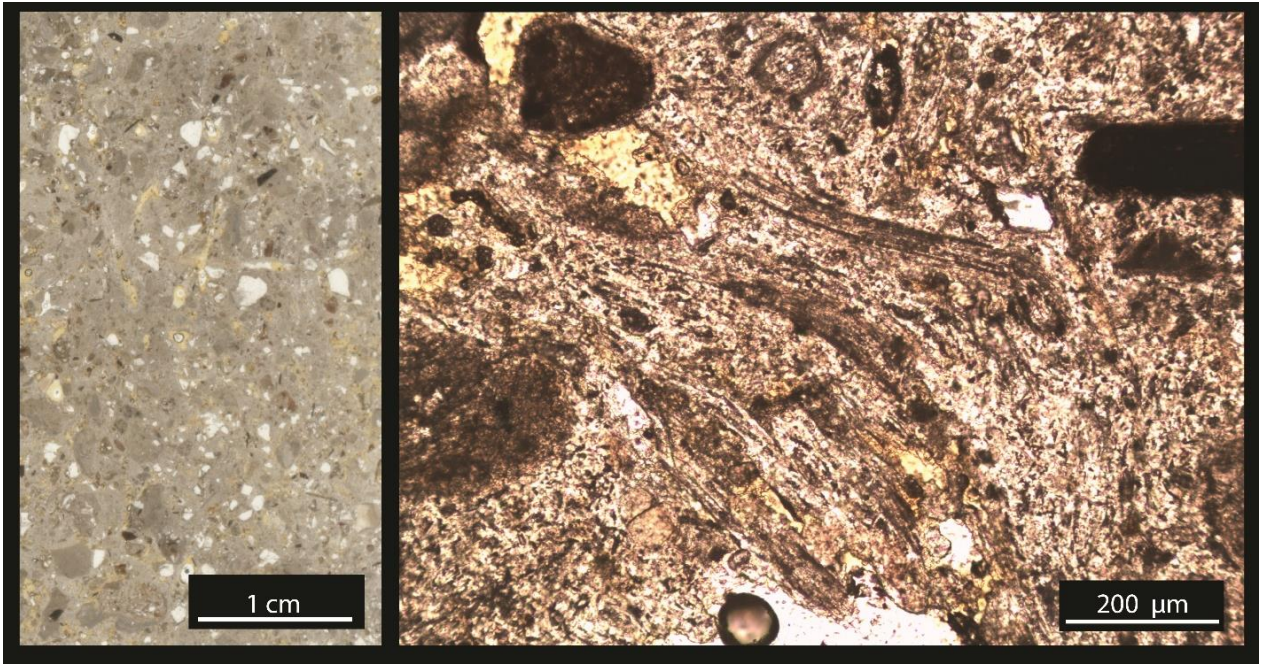
Figure 32. Sample 416. Silicified reeds.
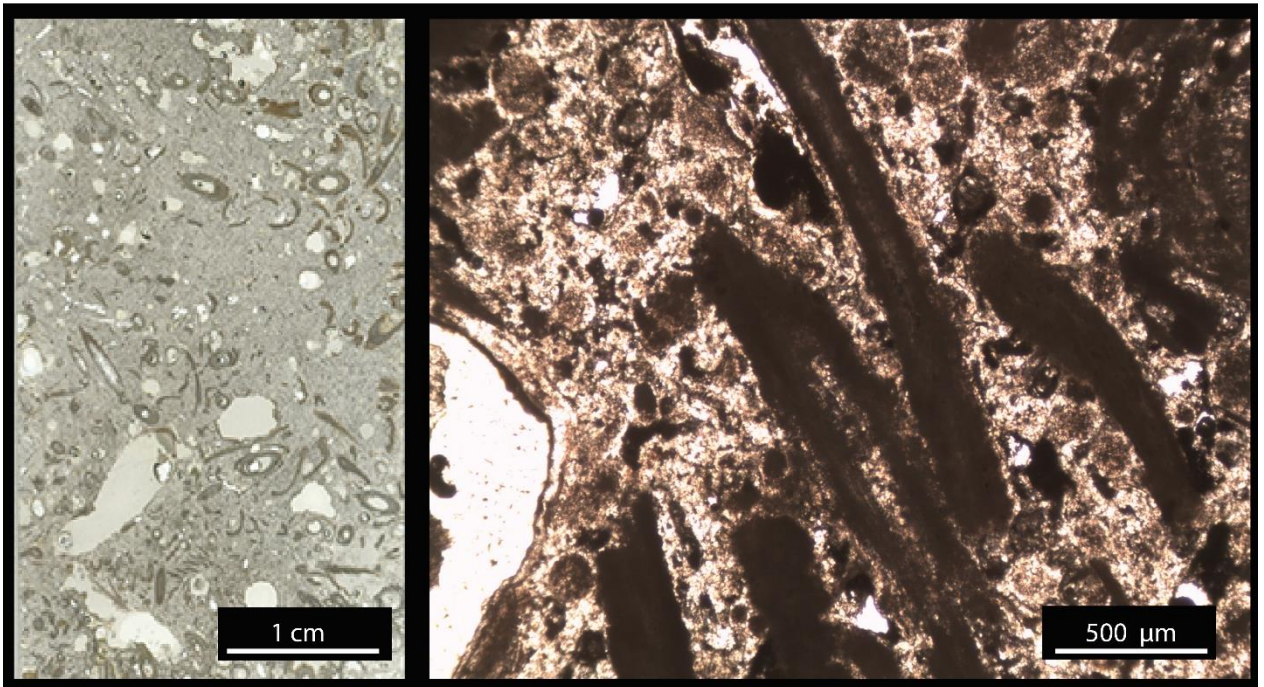
Figure 33. Sample 420. Plant fragments encased in the silica matrix.
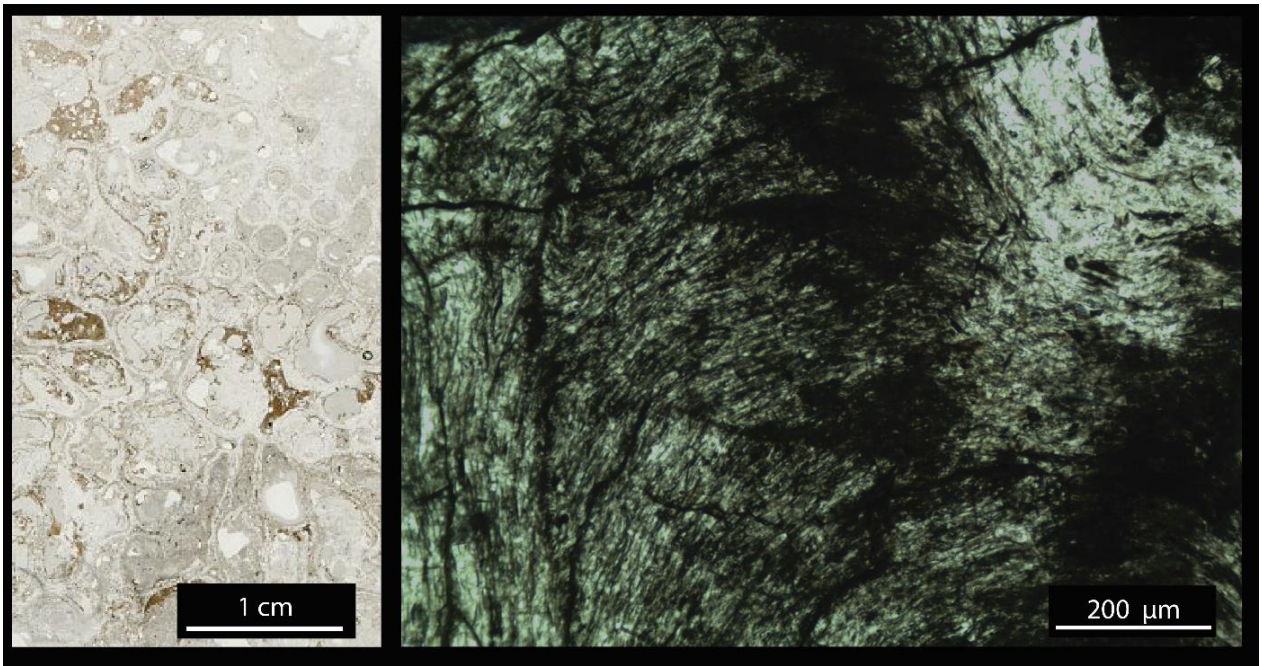
Figure 34. Sample 429t. Stromatolite-like lamination with moderately to steeply convex, relatively uniform laminae.
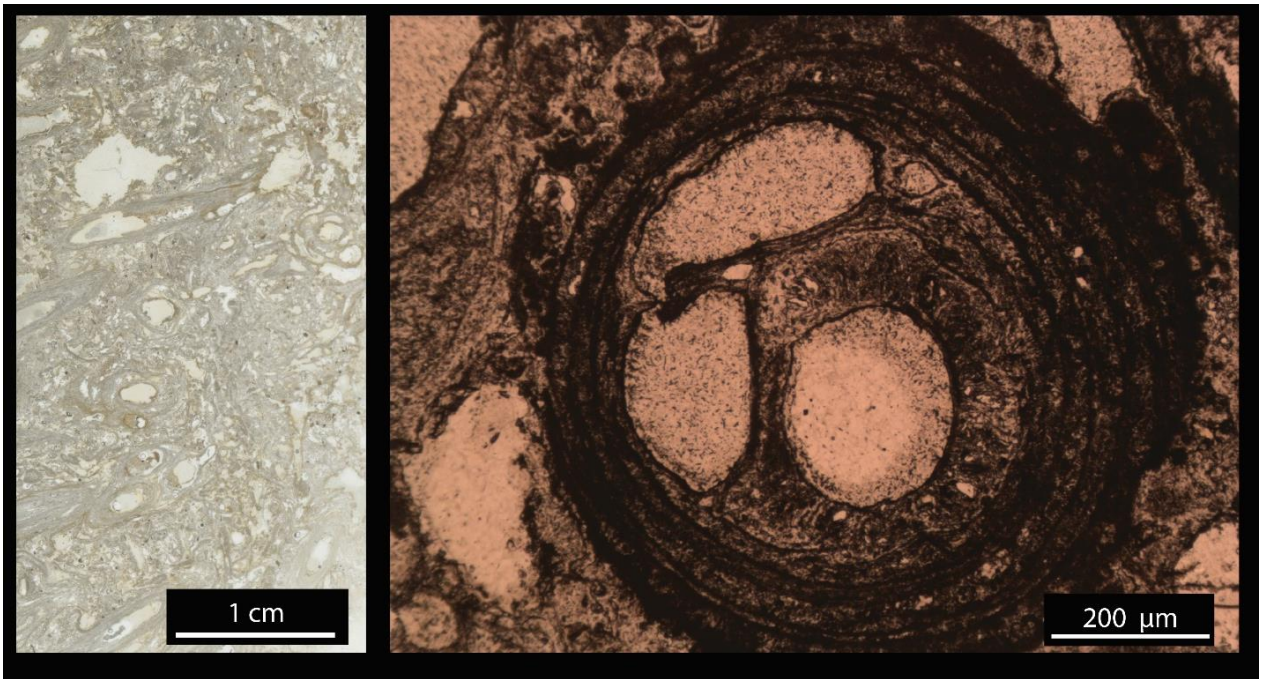
Figure 35. Sample 429b. Plant stems in cross-section with a concentric lamina of silica.
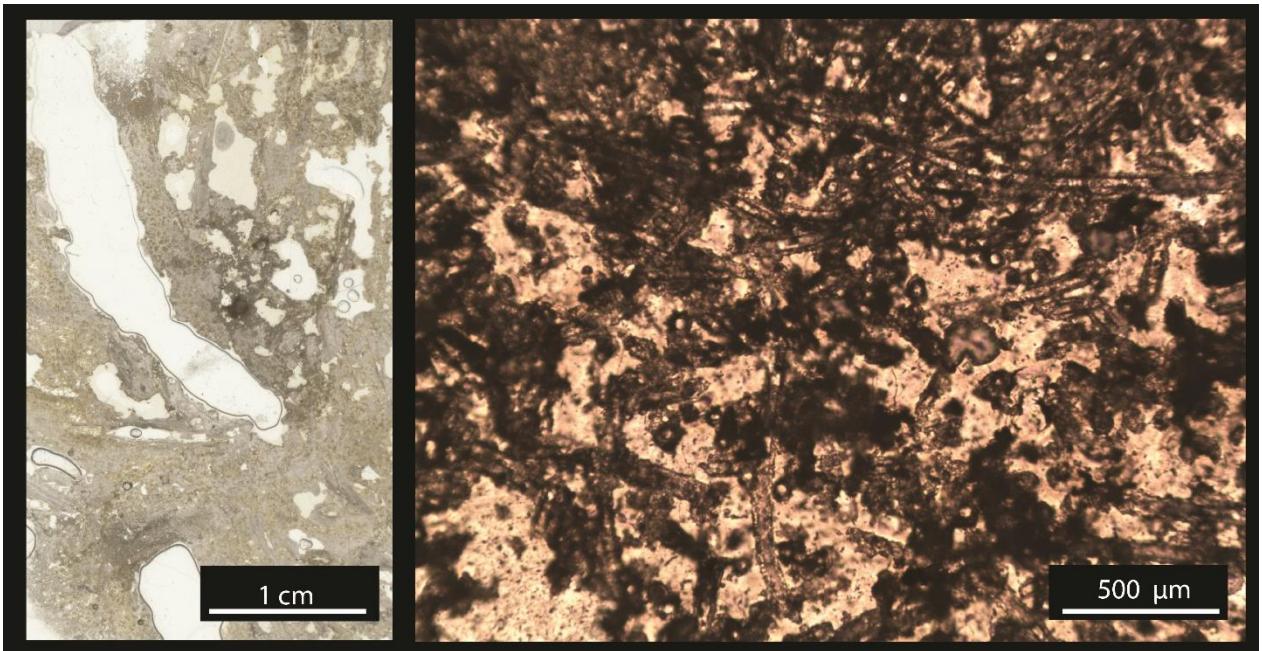
Figure 36. Sample 432. Empty tubular microfossils sheaths (sharp outline) with patchy recrystallization of the granular infill of individual filaments.
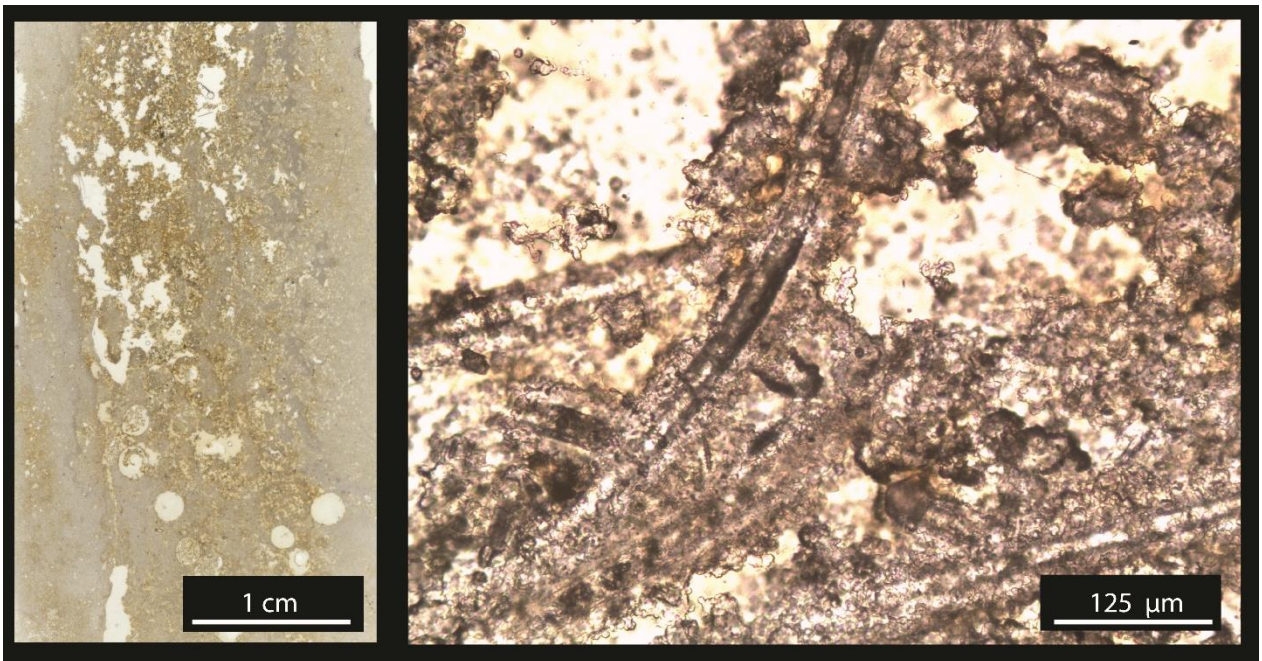
Figure 37. Sample 435. Microfossil sheath coated with silica spheroids.
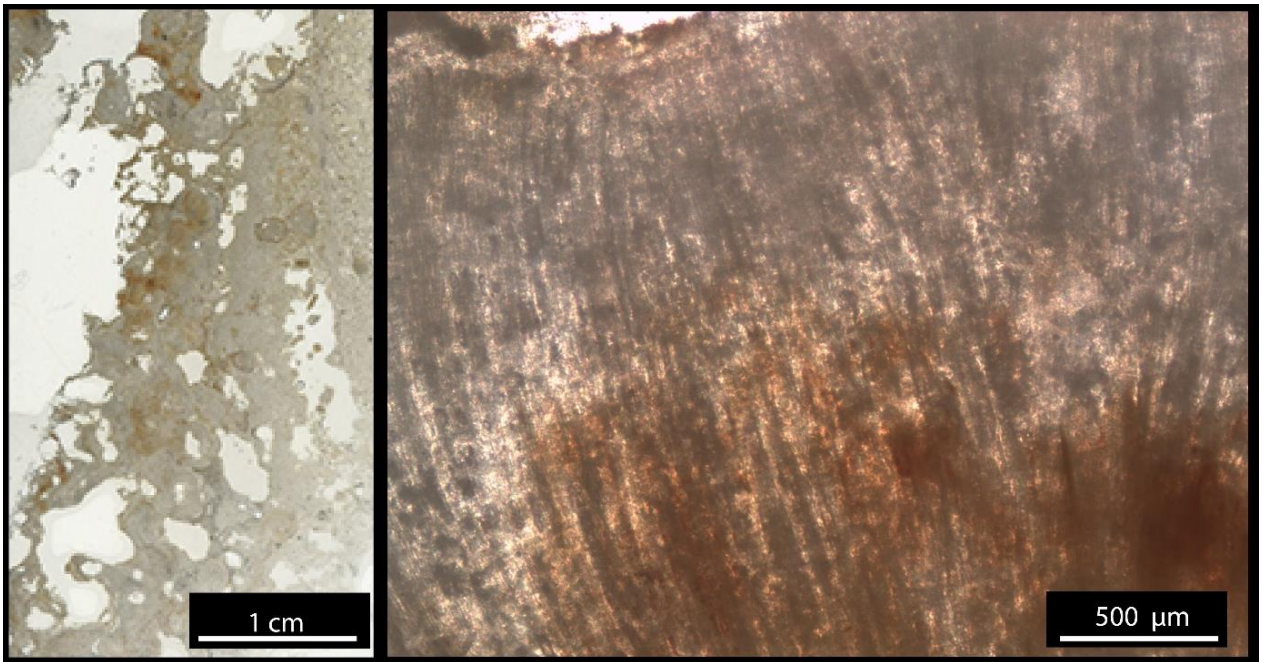
Figure 38. Sample 441. Longitudinal section of vertically oriented tubular microfossils, encased in a matrix of silica**.**
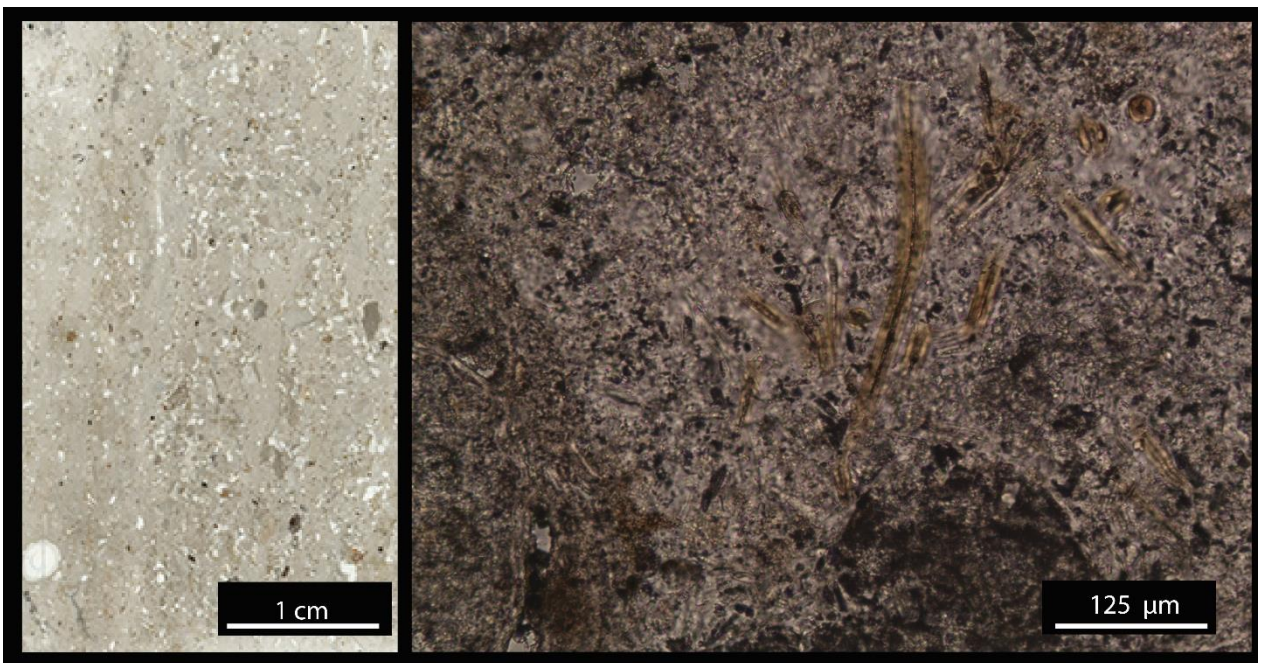
Figure 39. Sample 453. Detail of filaments in longitudinal section characterized by an outer sheath, dark granular interior fill, and translucent grainy interspace.
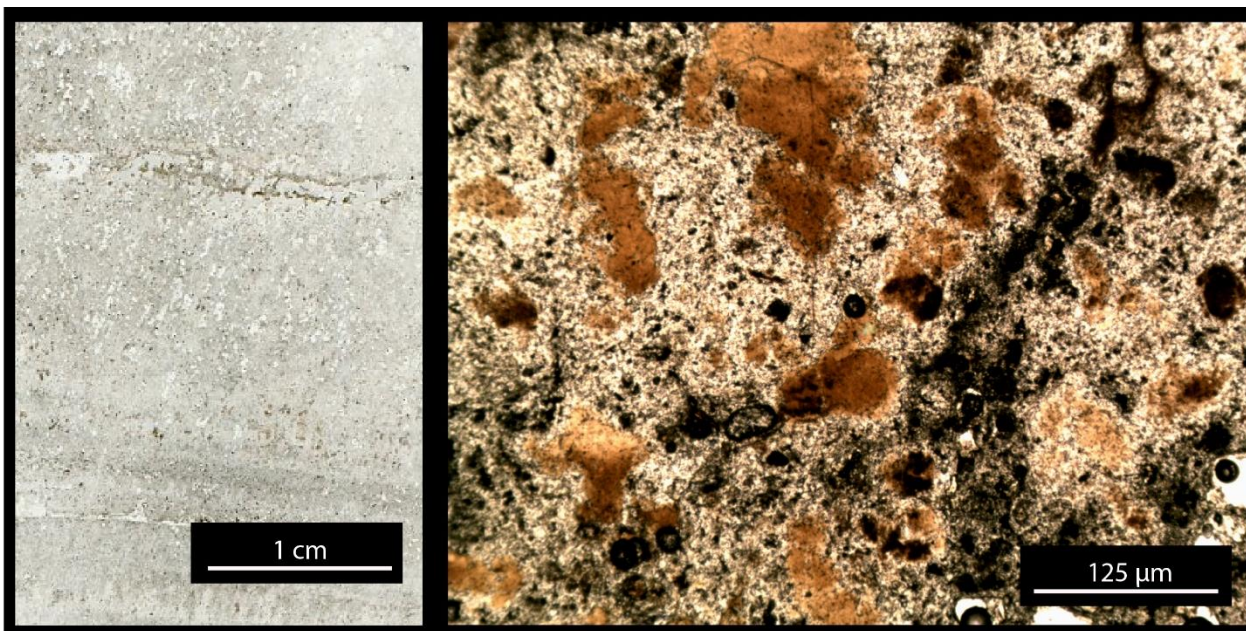
Figure 40. Sample 502b. Palisade texture. Clotted textures encrusting silica sinter fragments.
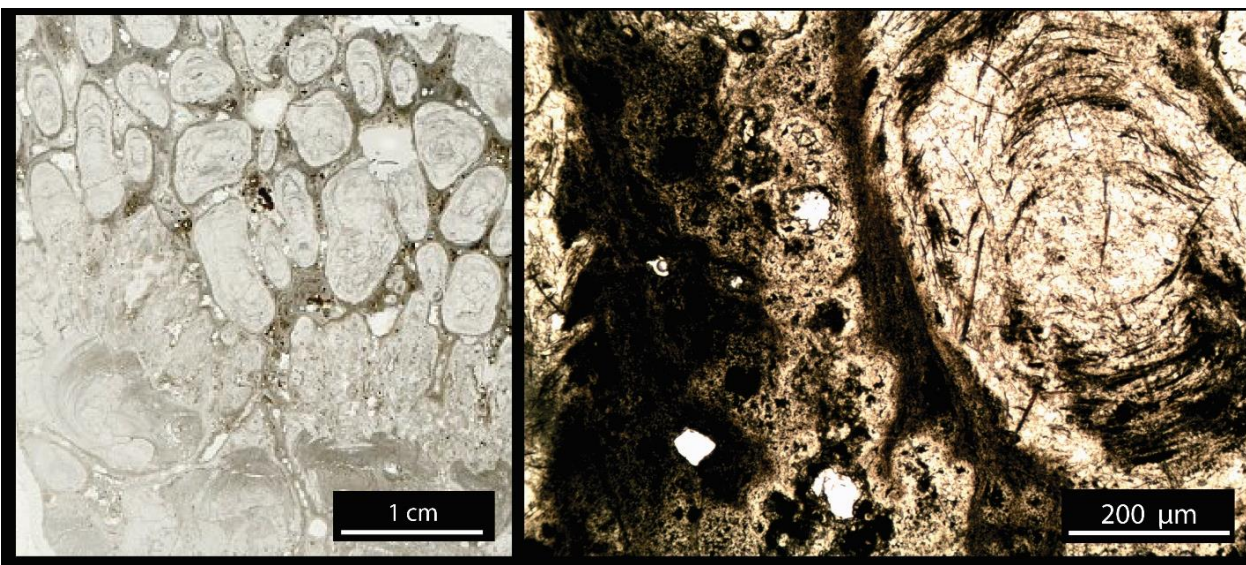
Figure 41. Sample 502m. Detail of the silicified columns of geyserite and their preserved internal texture.
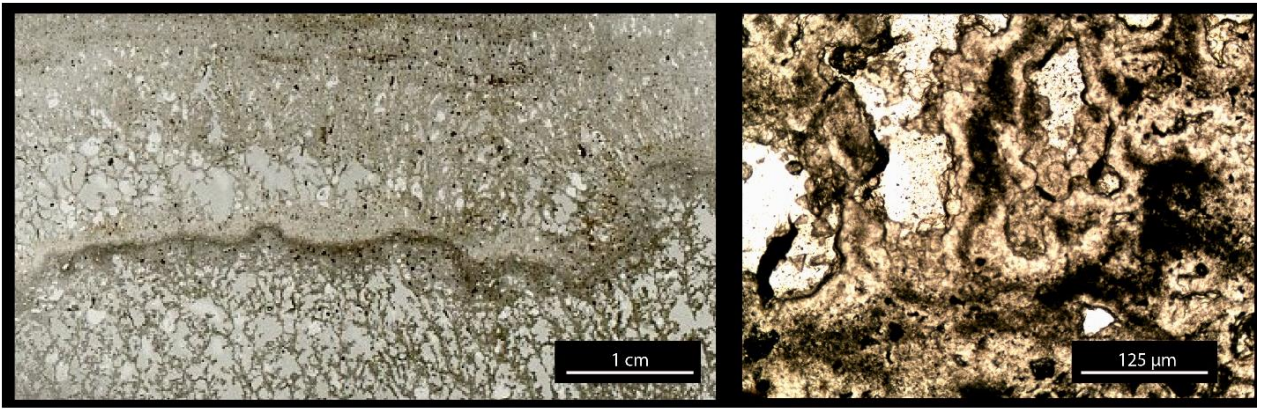
Figure 42. Sample 502t.Palisade texture**.** Two layers with of vertically oriented, tubular microfossils, encased in a matrix of transparent and clotted silica, with fenestrae of 100µm.
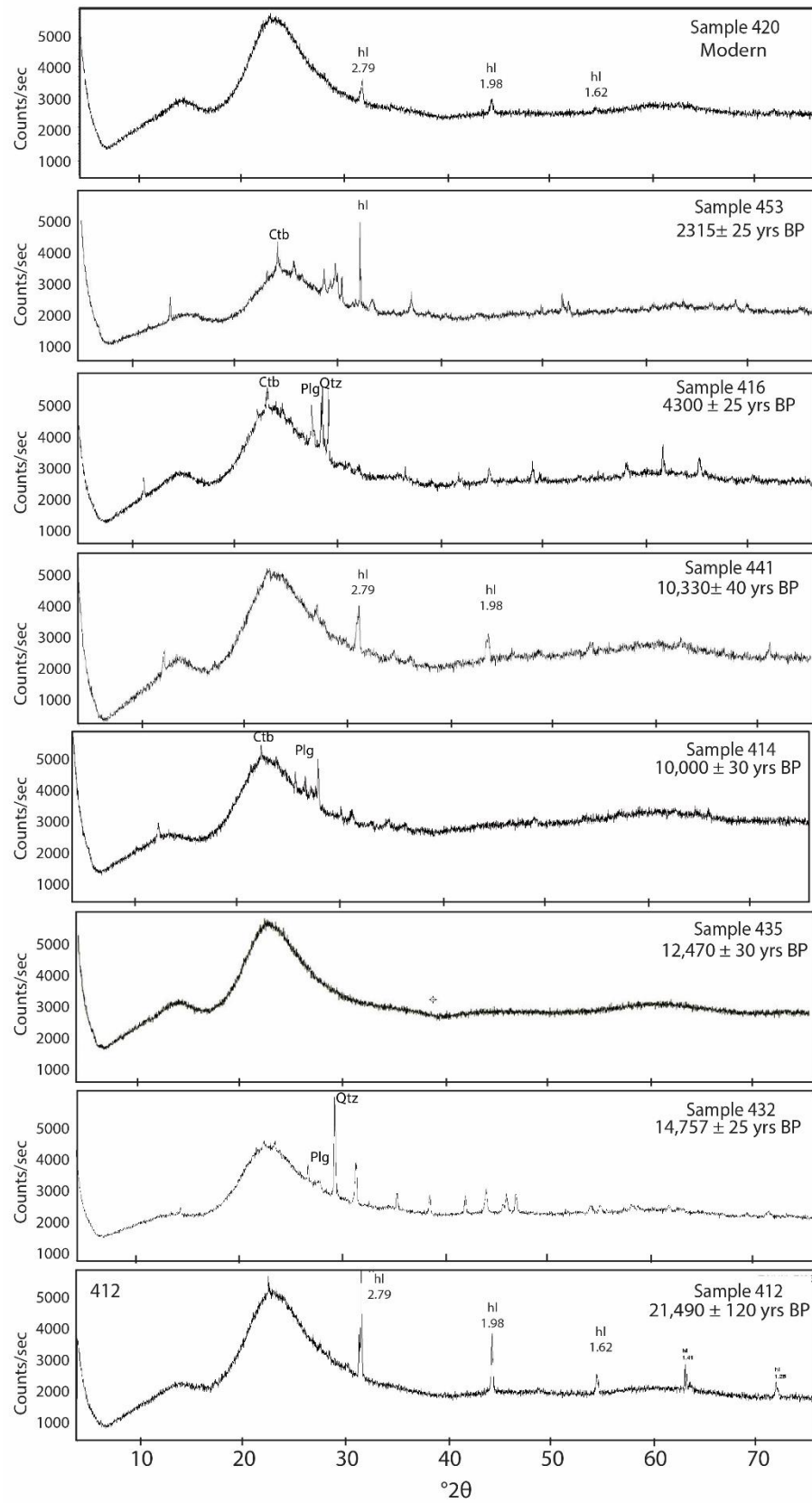
Figure 43. XRD spectra of selected samples, ordered by age.

Appendix C: Water geochemistry

Seventeen water samples were taken from eruptive and quiescent pools, as near as possible to the vent or seep, in April 2017. At each site, the thermal water was filtered using a 0.45 µm Millipore membrane and then collected in 125 ml bottles. Samples for cation analysis were acidified with 2 ml of HNO_3 after filtration. Sampling procedures used in this study were done following that of previous studies (e.g. Giggenbach and Gouguel, 1989). The temperature and pH of each site were measured in the field.

The major, minor and trace element composition of thermal water samples were determined at the Geology Department, Universidad de Chile. Anion concentrations were determined using a Metrohm 861 Advanced Compact Ion Chromatographer (IC), while cation concentrations, trace elements, and dissolved silica were analyzed using inductively coupled plasma optical emission spectrometry (ICP-OES).
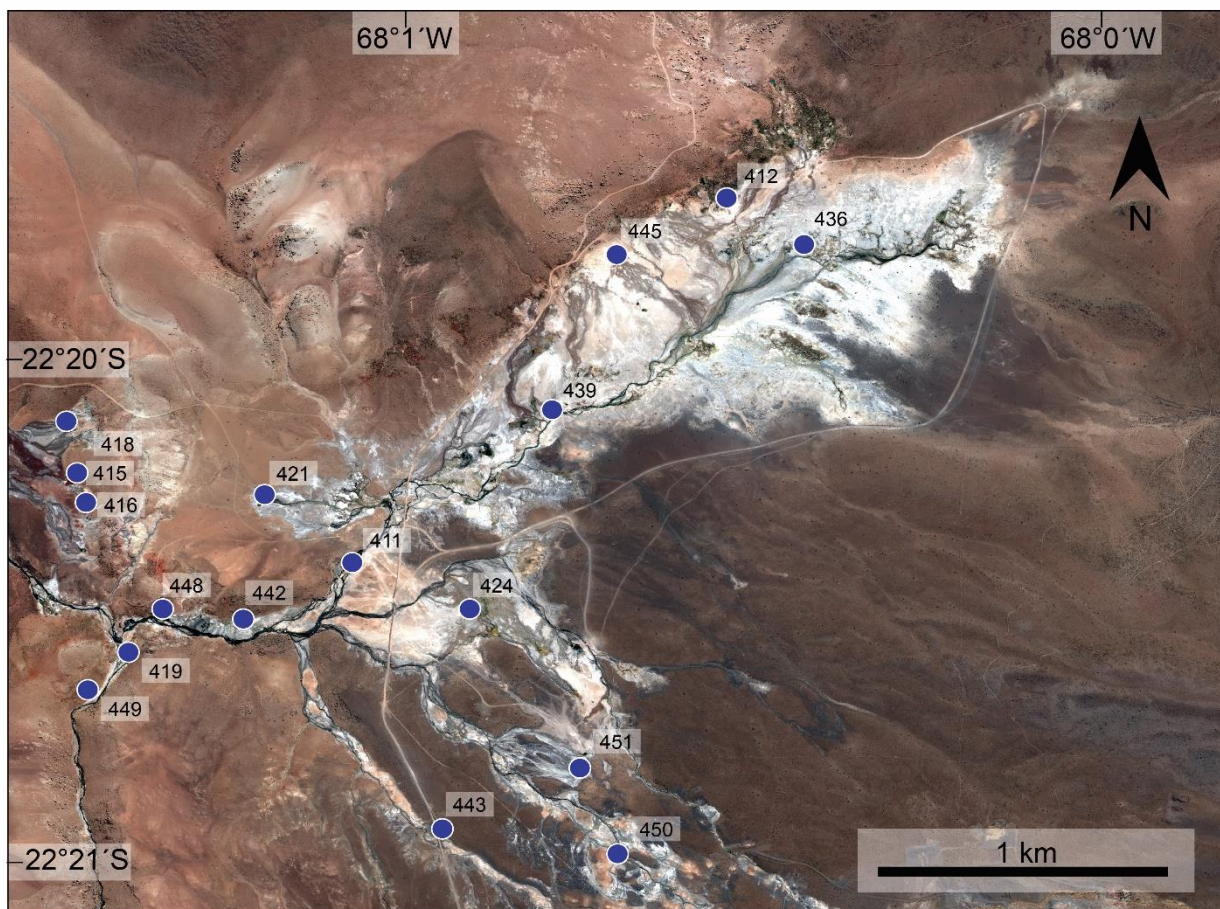
Figure 44. Water samples location at the El Tatio geyser field.

Table 7. Water geochemistry of major elements and physicochemical properties of thermal waters

Sample	Coord N	Coord E	Conductivity mS/cm	pH	Na (mg/L)	K (mg/L)	Ca (mg/L)	Mg (mg/L)	SiO_2 (mg/L)	Si (mg/L)	F (mg/L)	Cl (mg/L)	SO_4 (mg/L)	Br (mg/L)	No_3 (mg/L)	PO_4 (mg/L)
411	601063	7529259	14.71	7.49	3392	229	213	5.17	283	132	1.65	4695	43.8	4.66	< 0,10	< 0,10
412	602151	7530427	10.68	7.5	3188	438	110	3.41	113	96	0.27	280	227	0.31	0.27	< 0,10
416	600281	7529501	16.62	7.7	3313	372	232	1.95	505	236	2.4	5476	39	5.47	< 0,10	< 0,10
418	600237	7529732	18.57	7.5	3653	448	230	0.35	303	142	2.32	5806	40.7	5.93	< 0,10	< 0,10
419	600384	7528991	16.32	7.8	3431	235	222	2.95	283	132	1.88	5420	42.6	5.56	< 0,10	< 0,10
421	600794	7529458	12.2	7.69	2431	217	141	4.37	354	165	1.6	3685	38.6	3.67	< 0,10	< 0,10
424	601377	7529103	10.14	6.3	2030	117	141	0.77	375	456	0.66	3219	40.5	3.02	1,77	< 0,10
426	602156	7530255	12.27	6.58	2980	248	149	4.97	1050	491	1.66	4091	48.3	3.9	0,36	< 0,10
439	601667	7529739	6.1	6.85	1330	126	82.4	8.03	424	198	0.69	1964	46.3	1.95	< 0,10	< 0,10
443	601306	7528427	15.83	7.28	3473	147	232	15.8	444	208	2.04	5181	51.5	5.08	< 0,10	< 0,10
445	601818	7530248	23.01	7.05	5149	756	264	0.17	838	392	3.11	7865	41	7.92	< 0,10	< 0,10
447	600765	7529049	14.48	6.45	3448	172	213	4.58	606	283	1.5	5066	48.8	4.84	1,02	< 0,10
448	600506	7529097	16.5	7.65	3162	225	230	1.34	576	269	1.84	5292	44.5	5.44	< 0,10	< 0,10
449	600251	7528832	10.96	7.13	2533	162	149	6.15	475	222	0.72	3348	36.6	3.61	1,36	< 0,10
450	601812	7528341	16.2	6.07	3533	139	232	9.15	525	246	2.68	4717	53.2	4.96	< 0,10	< 0,10
451	601709	7528595	14.59	6.48	3979	150	253	7.02	364	170	2.94	5040	52.4	5.32	< 0,10	< 0,10

Table 8. Water geochemistry of minor and trace elements

Sample	Li (μg/L)	Be (μg/L)	B (μg/L)	Al (μg/L)	V (μg/L)	Cr (μg/L)	Fe (μg/L)	Mn (μg/L)	Co (μg/L)	Ni (μg/L)	Cu (μg/L)	Zn (μg/L)	As (μg/L)	Se (μg/L)	Rb (μg/L)
411	26372	< 1	114051	< 20	<60	7 13	1317	346	< 2	< 10	35.1	< 70	26674	< 30	2301
412	1841	< 1	112211	< 20	<60	<0.7	165	362	< 2	< 2	7.16	98	32284	<03	1694
415	7655	< 0,2	32486	< 4	9.3	<1.4	47	331	< 0,4	< 2	8.35	49.1	9069	<6	1046
416	30831	< 2	127049	< 40	< 120	< 14	< 200	479	< 4	< 20	< 40	< 140	34108	< 60	3598
418	32372	< 2	133035	< 40	< 120	< 14	< 200	197	< 4	< 20	< 40	< 140	35168	< 60	4178
419	29473	< 2	128955	< 40	< 120	< 14	< 200	324	< 4	< 20	< 40	< 140	29682	< 60	2980
421	21481	0.84	89802	< 10	34.4	<3,5	330	337	< 1	< 5	23.2	< 35	22710	< 15	2547
424	17012	< 0,5	78237	< 1	< 30	< 3,5	161	74.1	< 1	< 5	19.5	< 35	19498	< 15	1375
426	23386	< 0,5	96755	< 1	0 38,4	< 3,5	216	218	< 1	< 5	26.7	< 35	22634	< 15	2875
439	10433	< 0,2	43829	< 4	15,3	<1.4	75	76.0	< 0,4	5.226	11.10	49.6	10604	< 6	1321
443	26283	< 2	119500	< 40	< 120	< 14	684	653	< 4	< 20	< 40	< 140	29590	< 60	2065
445	41668	<2	172718	< 40	<120	14	< 200	253	<4	< 20	< 40	< 140	42952	< 60	6350
447	28305	<1	122632	20	60	7	1925	376	< 2	< 10	36.8	< 70	28182	< 30	2290
448	28349	<2	122794	< 40	120	14	< 200	136	< 4	< 20	< 40	< 140	29066	< 60	2811
449	18193	<0,5	86328	10	43.8	192	192	494	< 1	< 5	22.1	< 35	17940	< 15	1677
450	25992	<2	118962	< 40	120	14	1264	462	< 4	< 20	< 40	< 140	29321	< 60	1994
451	28817	<1	131477	20	60	7	1911	399	< 2	< 10	39.4	< 70	29429	< 30	2155

Table 9. Trace elements in El Tatio thermal waters

Sample	Sr (µg/L)	Zr (µg/L)	Mo (µg/L)	Ag (µg/L)	Cd (µg/L)	Sn (µg/L)	Sb (µg/L)	Cs (µg/L)	Ba (µg/L)	W (µg/L)	Hg (µg/L)	Pb (µg/L)	U (µg/L)
411	3101	54.5	35.8	< 0,3	< 0,4	< 1	1554	10526	230	15.9	< 0,4	< 0,8	< 0,1
412	3138	18.7	0.82	<0,03	<0,04	<0,1	61 1	10493	84.1	< 2	< 0,4	< 0,08	< 0,1
415	928	17.1	11.9	<0,06	<0,08	<0,2	1047	4006	60.3	22.1	0.96	< 0,16	0.069
416	3893	61.4	34.4	< 0,6	< 0,8	< 2	1902	11596	87.7	26.2	< 0,8	< 1,6	< 0,20
418	3903	62.6	31.6	< 0,6	< 0,8	< 2	2057	12520	65.0	27.2	< 0,8	< 1,6	< 0,20
419	3538	54	47.9	< 0,6	< 0,8	< 2	1529	12052	119	16.8	< 0,8	< 1,6	< 0,20
421	2285	45.7	29.1	< 0,15	< 0,2	< 0,5	1630	8989	210	14.9	0.65	< 0,4	< 0,05
424	1720	38	24.2	< 0,15	< 0,2	< 0,5	1430	7075	309	11.0	< 0,2	< 0,4	< 0,05
426	2216	45.5	30.4	< 0,15	< 0,2	< 0,5	1548	8867	232	20.4	0.83	< 0,4	0.41
439	1100	20.7	18.8	<0,06	< 0,08	< 0,2	598	3856	152	10.4	0.45	< 0,16	0.73
443	3495	53.2	31.5	< 0,6	< 0,8	< 2	1783	10382	193	14.9	< 0,8	< 1,6	< 0,20
445	4119	75	38.4	< 0,6	< 0,8	< 2	2710	15881	183	37.9	< 0,8	< 1,6	< 0,20
447	2921	56.5	38	< 0,3	< 0,4	< 1	1605	10768	350	21.7	< 0,4	< 0,8	< 0,1
448	3299	52.2	36.6	< 0,6	< 0,8	< 2	1809	11490	192	24.2	< 0,8	< 1,6	< 0,20
449	1869	35.8	58.2	< 0,15	< 0,2	< 0,5	594	6977	439	14.0	0.56	< 0,4	0.16
450	3573	53	30.9	< 0,6	< 0,8	< 2	1755	10449	65.6	11.9	< 0,8	< 1,6	< 0,20
451	3678	59.4	35.1	< 0,3	< 0,4	< 1	1984	11530	118	19.7	< 0,4	< 0,8	< 0,1